

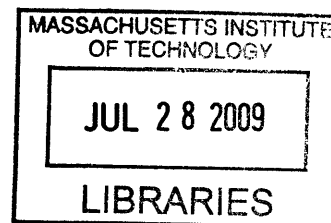
**Phase Behavior and Phase Transformation Kinetics during Electrochemical  
Cycling of Lithium Transition Metal Olivine Compounds**

By

**NONGLAK MEETHONG**

B.S. Ceramic Engineering

Alfred University, 2004



Submitted to the **Department of Materials Science and Engineering** in partial fulfillment of the requirements for the degree of

**DOCTOR OF PHILOSOPHY**

**ARCHIVES**

**IN MATERIALS SCIENCE AND ENGINEERING**

At the

**MASSACHUSETTS INSTITUTE OF TECHNOLOGY**


**JUNE 2009**

© 2009 Massachusetts Institute of Technology. All rights reserved.

Signature of Author:

Department of <sup>EM</sup>Materials Science and Engineering  
May 20, 2009

Certified by: \_\_\_\_\_

 Yet-Ming Chiang  
Kyocera Professor of Ceramics  
Thesis Supervisor

Accepted by: \_\_\_\_\_

 Christine Ortiz  
Associate Professor of Materials Science and Engineering  
Chair, Departmental Committee on Graduate Students

# Phase Behavior and Phase Transformation Kinetics during Electrochemical Cycling of Lithium Transition Metal Olivine Compounds

By  
Nonglak Meethong

Submitted to the Department of Materials Science and Engineering  
On May 20, 2009 in Partial Fulfillment of the Requirements for the Degree of  
Doctor of Philosophy in Structural and Environmental Materials

## Abstract

Olivine  $\text{LiMPO}_4$  ( $M = \text{Fe, Mn, Co, Ni}$ ) compounds have received most attention from the battery research community as the cathodes for Li-ion batteries because of several advantages, including a high theoretical capacity, 170 mAh/g, and flat discharge potential (with respect to  $\text{Li/Li}^+$ ) of 3.45 V, 4.1V, 4.8V, and 5.1V, respectively, for Fe, Mn, Co, and Ni. Among these,  $\text{LiFePO}_4$  has received the most attention for its likelihood to provide low price, good cycling stability, thermal stability, and low-toxicity. It is being utilized in a new generation of Li-ion batteries for high power applications such as power tools and electric vehicles. However,  $\text{LiFePO}_4$  cathodes also have several drawbacks, such as low electronic conductivity, and slow Li-ion transport during the  $\text{LiFePO}_4/\text{FePO}_4$  two-phase transformation during the charge-discharge process. This results initially in poor rate capability and making the practical utility of these compounds unclear. Numerous studies have attributed the rate capability of olivines purely to chemical diffusion limitations. Many efforts have been devoted to improving the conductivity and the rate performance of  $\text{LiFePO}_4$  cathodes. Since this class of olivines undergoes a first-order phase transition upon electrochemical cycling, in order to improve rate capability, an equally important goal is to maximize the rate of phase transformation. In this work, the impact of phase behavior and phase transformation on electrochemical properties such as voltage profile, cycle life, and rate capability of olivine compounds was studied in several aspects. We found that: (1) the phase diagram of  $\text{Li}_{1-x}\text{FePO}_4$  is size and composition-dependent; (2) elastic misfit between the triphylite and heterosite phases during electrochemical cycling plays a significant and previously unrecognized role in determining the rate capability and cycle life of olivine compounds; (3) the phase transformation path of nanoscale olivines  $\text{Li}_{1-x}\text{MPO}_4$  ( $M = \text{Mn, Fe}$ ) is much more complex than their conventional coarse grained counterparts. Upon electrochemical cycling, a fraction (increasing with increasing size) of the delithiated  $\text{Li}_y\text{MPO}_4$  that is formed is partially amorphous or metastable. Finally, (4) aliovalent cation substitution is an effective and controllable way to improve electrochemical properties, especially rate capability, of the  $\text{Li}_{1-x}\text{FePO}_4$  olivine compounds.

Thesis Supervisor: Yet-Ming Chiang

Title: Kyocera Professor of Ceramics, Department of Materials science and Engineering

## **Acknowledgement**

Throughout the course of my studies at MIT, I received a great deal of love, help, support, guidance, and encouragement from many people around me. I would like to take this opportunity to express my sincere appreciation to everyone.

First and foremost, I would like to acknowledge the Royal Thai Government Scholarship Program for their financial support which allowed me to come to the United States and have a chance to fulfill my dream.

Prof. Yet-Ming Chiang, my advisor, has been supportive throughout these past five years at MIT. His guidance, inspiration, and consolation are beyond my words. I am so thankful and grateful for the opportunities he has given me. Under his supervision, I had many great opportunities to present my research work to the battery research community in many conferences organized in various parts of the world. I would like to thank him for encouraging me to be confident and to think of myself as being a researcher rather than just a graduate student.

I am thankful to Prof. Craig Carter and Prof. Bernhardt Wuensch, my thesis committee, for their valuable suggestions and for making this thesis a readable one. Prof. Carter's good sense of humor has brightened up my life at MIT. Prof. Wuensch's generosity and passion to teach have also inspired me.

My gratitude also goes to my co-authors. I am thankful to Dr. Hsiao-Ying Huang, Dr. Ming Tang, Dr. Scott Speakman (Center of Materials Science and Engineering at MIT), Dr. Celine Han, and Yu-Hua Kao for co-authoring several publications; some of which are presented in this thesis. I would like to thank and share this accomplishment with them all.

I would like to thank people in Chiang and Carter groups and former colleagues - Dr. Dong-wan Kim, Miso Kim, Tim Chin, Vyom Sharma, Bryan Ho, Dr. Young-kyo Cho, Dr. Ryan Wartena, Dr. Can Erdonmez, Dr. Wei Lai, Dr. Chang-jun Bae, Dr. Yan Wang, and

Dr. Shen Dillon for sharing with me their experience, knowledge, and of course, their lab supplies and equipment. They all have made my life in the lab a pleasant one.

I would like to thank Toni Centorino, Kathy Farrell, Angelita Mireles, and Rachel Kemper for their administrative assistance and hard work to make sure that I would not miss any important deadlines. Toni has also made all of the conference trips during these past five years a lot less hectic for me.

I wish to express my sincere appreciation to all of my TSMIT (Thai Students at MIT) friends whose names cannot be all listed here, but will always be kept in my memory. They have always been my wonderful cheerleaders. They have made MIT a home away from home for me. Special thanks go to P'Naan Panitarn, P'Nok Samerkhae, P'Lek Wanida, P'Ae Ratchatee, and P'Vee Yuttanant, for helping me from the very first day during the DMSE visiting weekend to the very fun and supportive years in the department. Best wishes go to N' Kob Tongjai, N' Jin (both are 3<sup>rd</sup> year DMSE graduate students), and N'Boat Siamrut (incoming 1<sup>st</sup> year DMSE graduate student). I am thankful to P' Gift Piyatida for helping me with various things from grocery shopping to writing MATLAB codes. Thank to Yeaw Numpon, P'Peng Warit, N'Kai Chollakarn, Mint Chanikarn, and Oh Surapap for being such good supporters and Zipcar drivers for me. Many thanks go to P'Puk Nisanart for everything, especially, updating me with all the shoe sale ads and feeding me with her yummy Thai food, various kinds of no berries snacks, and sweet Thai drinks.

Many thanks to Thai Scholar' 43 friends for the fun and youthful moments we had together since our first day of the journey (July 7, 2000) to the United States. Special thanks to Omom Pimporn, Mint Chanikarn, Fai Vorrapan, Nammon Mananya, Ple Pornkamol, Jeab Naraphorn for moral support they have provided for the past 9 years. Best wishes to everyone and good luck with their research work. I wish to thank Chris Brown and Poo Rorke for organizing the summer program at Brewster Academy about 9 years ago and continuing to provide encouragement and support for us until these days. I will always remember Poo Rorke's quote, "There is nothing Thai Scholars cannot do, if

we do it together.” I will be waiting for my TS’43 friends in Thailand, and we will one day reunite and make positive changes to our beloved country together.

I would like to thank my Satri Nakhonsawan friends for keeping me in the loop. I enjoyed reading their posts on my Hi5 and late night chats with many of them, especially Onsiri, Amp, Tan, Toey, First, Pai, Ji-beau, Safe, and Naam. Although our lives have gone in different paths, I am so glad we have managed to keep in touch and been there for each other once in a while.

My deepest gratitude goes to my family for their endless love and support that help me survive the tough, and at many times lonely, years in the United States. Mom and dad are “super parents”. They have shown me how persistent and hard working one can be. They always make sure that their children get the best of what they can possibly provide, although, in many times, that would mean sacrificing their own needs. They are the best parents I imagine I could ever have. My eldest sister, P’Waw Naowarat, has always been a good role model, a listener, and a great cheerleader. My younger sister, Net Kanchana, has proven to be my best personal negotiator and my spoke-person. N’Pang Nichayada, my youngest little sister has always been the center of love and provided a huge source of encouragement for me. Many times simple words from her can truly lift up my spirit. Whenever I felt like giving up, a yearning to be a good role model for her kept me going. Sutham has been providing me with tremendous amount of love and support throughout these years. He has been taking good care of not only me, but also my family. He has showed me what it is like to care and to be cared about. This thesis would have not been completed without him.

Last but not least, I would like to thank all of my beloved teachers, whom I dedicate this thesis to, for their guidance, support, inspiration, encouragement, and belief in me. Even though this thesis came too late for some of them, I would like them to know that without all of them there those days; there would have not been Dr. Nonglak Meethong here today. Wherever they are or might be; I would like to say, “Thank you!”

# **Dedication**

To All of My Beloved Teachers

Thank You!

# Contents

<b>ABSTRACT</b> .....	<b>2 -</b>
<b>ACKNOWLEDGEMENT</b> .....	<b>3 -</b>
<b>DEDICATION</b> .....	<b>6 -</b>
<b>LIST OF FIGURES AND TABLES</b> .....	<b>10 -</b>
<b>CHAPTER 1</b> .....	<b>16 -</b>
MOTIVATION.....	16 -
THESIS OUTLINE .....	20 -
<i>Chapter 1 Figures and Tables</i> .....	23 -
<b>CHAPTER 2</b> .....	<b>25 -</b>
BACKGROUND ON OLIVINE COMPOUNDS .....	25 -
BACKGROUND ON EXPERIMENTAL TECHNIQUES.....	28 -
<i>Electrochemical Measurement: Galvanostatic Cycling</i> .....	28 -
<i>Electrochemical Measurement: Intermittent Titration Techniques</i> .....	28 -
<i>Electrochemical Measurement: Cyclic Voltammetry</i> .....	29 -
<i>Diffraction and Rietveld Refinement</i> .....	29 -
<i>Electron Microscopy</i> .....	30 -
<i>References</i> .....	30 -
<i>Chapter 2 Figures and Tables</i> .....	32 -
<b>CHAPTER 3</b> .....	<b>35 -</b>
SIZE-DEPENDENT PHASE DIAGRAM OF $\text{Li}_{1-x}\text{FePO}_4$ .....	35 -
<i>Introduction</i> .....	36 -
<i>Experimental Section</i> .....	36 -
Test Materials.....	36 -
Electrochemical Tests .....	37 -
Structural Analysis.....	38 -
<i>Results and Discussion</i> .....	38 -
Low-Rate Galvanostatic Tests .....	38 -
Potentiostatic Intermittent Titration Tests (PITT) .....	39 -
Diffraction Studies of Size-Dependent Miscibility at Room Temperature .....	41 -
Origin of Size-Dependent Nonstoichiometry .....	43 -
<i>Summary and Conclusions</i> .....	45 -
<i>References</i> .....	45 -
<i>Chapter 3 Figures and Tables</i> .....	47 -

<b>CHAPTER 4 .....</b>	<b>- 54 -</b>
PHASE BEHAVIOR OF NANOSCALE $\text{Li}_{1-x}\text{FePO}_4$ AND CRITERION FOR SELECTING MATERIALS FOR HIGH-POWER RECHARGEABLE BATTERIES .....	- 54 -
<i>Introduction</i> .....	- 55 -
<i>Experimental Section</i> .....	- 55 -
Test Materials.....	- 55 -
Electrochemical Tests .....	- 57 -
Structural Analysis.....	- 57 -
Thermodynamic Model.....	- 58 -
<i>Results and Discussion</i> .....	- 58 -
Electrochemical Measurements .....	- 58 -
Diffraction Studies .....	- 60 -
Coupling between Elastic Misfit, Lithium Nonstoichiometry, and Rate Capability- 62 -	
Thermodynamic Model.....	- 64 -
Kinetic Limitations in the Presence of Incoherent Interfaces.....	- 67 -
<i>Summary and Conclusions</i> .....	- 68 -
<i>References</i> .....	- 69 -
<i>Chapter 4 Figures and Tables</i> .....	- 72 -
<b>CHAPTER 5 .....</b>	<b>- 79 -</b>
ELECTROCHEMICALLY INDUCED PHASE TRANSFORMATION IN NANOSCALE OLIVINES $\text{Li}_{1-x}\text{MPO}_4$ (M = Fe, Mn) .....	- 79 -
<i>Introduction</i> .....	- 80 -
<i>Experimental Section</i> .....	- 82 -
Test Materials.....	- 82 -
Electrochemical Tests .....	- 83 -
Structural Analysis.....	- 84 -
<i>Results and Discussion</i> .....	- 85 -
Time- and State-of-Charge Dependence of OCV .....	- 85 -
State-of-Charge Dependence of “Triphylite” and “Heterosite” Phase Fractions- 87 -	
- .....	
Additional Amorphous or Disordered Phases.....	- 90 -
Phase Transformation upon Cycling of Nano- $\text{Li}_{1-x}\text{MnPO}_4$ .....	- 92 -
General Discussion .....	- 92 -
<i>Summary and Conclusions</i> .....	- 97 -
<i>References</i> .....	- 97 -
<i>Chapter 5 Figures and Tables</i> .....	- 101 -
<b>CHAPTER 6 .....</b>	<b>- 108 -</b>
ALIOVALENT SUBSTITUTIONS IN OLIVINE LITHIUM IRON PHOSPHATE AND IMPACT ON STRUCTURE AND PROPERTIES .....	- 108 -
<i>Introduction</i> .....	- 109 -
<i>Experimental Section</i> .....	- 110 -
Experimental Strategy.....	- 110 -
Test Materials.....	- 111 -



Structure Analysis .....	- 111 -
Electron Microscopy .....	- 112 -
Electrochemical Tests .....	- 112 -
<i>Results and Discussion</i> .....	- 113 -
Bulk Solid Solution of 2+ through 5+ Aliovalent Dopants .....	- 113 -
Effect of Particle Size on Dopant Solubility .....	- 115 -
Potentiostatic Titration Measurements of Lithium Immiscibility and Phase Transformation Kinetics .....	- 119 -
<i>Summary and Conclusions</i> .....	- 122 -
<i>References</i> .....	- 125 -
<i>Chapter 6 Figures and Tables</i> .....	- 128 -
<b>CHAPTER 7</b> .....	<b>- 141 -</b>
CONCLUSIONS.....	- 141 -
<i>Summary</i> .....	- 141 -
<i>Future Work</i> .....	- 144 -
Lithium Transport Kinetics in Olivine Cathodes.....	- 144 -
Electrochemically Driven Phase Transformations Studies using In-situ X-ray Diffraction.....	- 145 -
Mixed Transition Metal Olivines Cathodes for Li-ion Batteries .....	- 146 -
<i>References</i> .....	- 146 -

## List of Figures and Tables

Figure 1-1: Lithium-ion batteries for various applications including portable electronics, power tools, and electric vehicles.....	23 -
Figure 1-2: Example of battery packs for electric vehicle applications.....	23 -
Figure 1-3: Electrochemical processes in Li-ion batteries during charging and discharging. During discharge, an electrical circuit is formed, the anode material (in this case lithiated carbon) oxidizes, or gives up electrons, while the cathode material (in this case lithium cobalt oxide) immersed in an electrolyte becomes reduced, or gains electrons. Lithium ions move from the anode to the cathode to provide charge neutrality so that the reactions can continue and the electrons can keep flowing providing electrical energy to the connected device. During charge, the process is reversed: the cathode and the anode are oxidized and reduced, respectively. The electrical energy is restored to the battery.....	24 -
Figure 2-1: Polyhedral representation of olivine $\text{LiFePO}_4$ structure projecting along the [001] direction.....	32 -
Figure 2-2: Schematic representation of the system during cycling showing the two phase end-members; triphylite and heterosite. ....	32 -
Figure 2-3: Schematic illustration of the “core-shell” model explaining the discharge process of $\text{Li}_x\text{FePO}_4$ proposed by Srinivasan and Newman. ....	33 -
Figure 2-4: Phase diagram comparison of conventional coarse-grained $\text{LiFePO}_4$ studied by a) Dodd et al., <sup>23</sup> b) Delacourt et al., <sup>22</sup> and c) Zhou et al., <sup>24</sup> showing existence of miscibility gap in this system. At low temperature, two-phase coexistence of the Li-rich (triphylite or T) and Li-poor (heterosite or H) end-members is observed. At intermediate temperatures, the proposed phase diagram resembles a eutectoid system, with eutectoid point at around $x = 0.45-0.65$ and 150 - 200 °C. The disordered (D) or solid solution phase (SS) is proposed at high temperatures. ....	34 -
Table 2-I: Lattice parameters and unit cell volume for triphylite and heterosite phases as determined by Rietveld refinement, by Andersson et al. <sup>16</sup> .....	34 -
Figure 3-1: Sample preparation and firing schedule for the studied powders. ....	47 -
Figure 3-2: Transmission electron microscopy (TEM) images of three powder samples tested, having the following BET specific surface areas and equivalent spherical particle diameters. (A) 48.8 $\text{m}^2/\text{g}$ , 34 nm; (B) 39.8 $\text{m}^2/\text{g}$ , 42 nm; (C) 14.8 $\text{m}^2/\text{g}$ , 113 nm. Sample C is a “carbon added” commercial sample in which fibrillar carbon can be seen, in contrast to samples A and B which have no detectable carbon phase.....	47 -
Figure 3-3: Galvanostatic charging (top) and discharging (bottom) at C/50 rate shows the narrower composition range over which smaller size particles exhibit a constant cell voltage corresponding to two-phase coexistence. Note also the overpotential measured on charge for the coarsest sample C as the two-phase plateau voltage is approached, absent for finer particle size samples A and B (inset). The two-phase plateau voltage also differs measurably for the three samples.....	48 -

Figure 3-4: Lithium solubility in the triphylite and heterosite phases is determined from the capacity vs. voltage measured potentiostatically upon charge and discharge in 5 mV steps. The OCV measured by taking each cell to 50% SOC and allowing voltage relaxation is indicated for each sample. Sample A has average particle diameter of 34 nm while sample C average particle diameter of 113 nm. .... - 49 -

Figure 3-5: Phase diagram for nanoscale lithium iron phosphate showing that the miscibility gap contracts systematically (increased solid solution limits) with decreasing particle size and increasing temperature. Numbers in parenthesis indicate the number of data points taken at that temperature to ensure consistency of the results. .... - 50 -

Figure 3-6: Phase diagram for nanoscale lithium iron phosphate plotted against the equilibrium phase diagram of Dodd et al.<sup>10</sup> ..... - 50 -

Figure 3-7: Lithium nonstoichiometry as a function of equivalent spherical diameter plot shows that below ~15 nm particle diameter, the miscibility gap may disappear completely at room temperature. .... - 51 -

Figure 3-8: Rietveld refined X-ray patterns for samples A, B, and C respectively, taken on samples at ~ 50% state of charge, including the fit to Si powder added as an internal standard. The observed intensity data are shown by the solid red line, and the dashed blue, aqua, and green lines overlying them are the calculated intensity of LiFePO<sub>4</sub>, FePO<sub>4</sub>, and Si respectively. The difference between the observed and calculated intensities is shown for each of the patterns. .... - 52 -

Table 3-I: The corresponding structural parameters obtained from the refinements of X-ray diffraction spectra (Figure 3-8). .... - 53 -

Table 3-II: Comparison of lithium solid-solution limits obtained from Rietveld refinement of X-ray diffraction spectra (Figure 3-8), assuming Vegard's law, with those obtained by PITT. .... - 53 -

Figure 4-1: Comparison of specific discharge capacity versus galvanostatic C rate for samples NC (top) and AC (bottom), representing high-rate doped nanoscale and "carbon-added" lithium iron phosphates respectively, measured in lithium half-cells of Swagelok™ type. Before each discharge, cells were charged at C/2 rate and held at 3.80 V until the current decays to C/25 rate. .... - 72 -

Figure 4-2: Galvanostatic charging (left) and discharge (right) at C/50 and C/100 rates shows the narrower composition range over which high rate doped nanoscale powders (sample NC) exhibit a constant cell voltage indicating two-phase coexistence, compared to the lower rate carbon-added sample AC. Note also the overpotential measured on charge for sample AC as the two-phase plateau voltage is approached, absent for sample NC (inset). OCV differs slightly for the two samples as discussed in text, indicated in inset. .... - 72 -

Figure 4-3: Capacity versus voltage measured potentiostatically upon charge and discharge in 10 mV steps. The OCV is indicated for each cell. a) Nb-doped nanoscale sample NC; b) carbon-added undoped LiFePO<sub>4</sub> sample AC. c) Full-scale representation of the data. .... - 73 -

Figure 4-4: Rietveld refined X-ray patterns for samples NC and AC respectively at ca. 50% state of charge, including the fit to Si powder added as an internal standard. The observed intensity data are shown by the solid red line, and the dashed blue, aqua, and green lines overlying them are the calculated intensity of  $\text{LiFePO}_4$ ,  $\text{FePO}_4$ , and Si respectively. The dashed lines are the calculated intensity of the aluminum peaks from the current collector. The difference between the observed and calculated intensities is shown for each of the pattern. The structural results are shown in Table 4-I..... - 74 -

Figure 4-5: Voltage steps (black) and corresponding current relaxation (red) during PITT measurements (10 mV steps, C/50 current cutoff) in the second charge cycle, indicating rate of phase transformation as a function of the applied potential. a) Doped nanoscale sample NC exhibits peak current at the start of each voltage step, followed by monotonically decaying current, at all overpotentials. b) Comparison sample AC exhibits a slow increase in the current at constant voltage, peaking nearly 4 h after the application of overpotential, indicating a time-varying barrier to phase transformation. Higher overpotentials are also required for phase transformation..... - 75 -

Figure 4-6: a) Molar free energy of two positive electrode phases illustrating tangent construction relating chemical potential differences and electromotive force in the absence of stored elastic energy. The reference energies are scaled so that the common tangent has zero slope. b) Within the two-phase region, a coherent interface between phases differing in molar volume produces an additional contribution to the molar free energy and is illustrated for the case of a spherical shell and spherical cap. .... - 76 -

Figure 4-7: Elastic energy normalized to volume and Young's modulus E, vs. volume fraction transformed phase, for the case of a spherical shell and a spherical cap. Poisson's ratio  $\nu$  is assumed to be 1/3. .... - 77 -

Figure 4-8: Transmission electron micrographs of starting powders of Sample AC (left) and after high rate cycled showing a high density of dislocations (right). .... - 77 -

Table 4-I: Physical and structural characteristics of a high rate doped nanoscale (Sample NC) and lower-rate "carbon-added" lithium iron phosphate (Sample AC), compared with literature data for  $\text{LiFePO}_4$  and  $\text{LiMnPO}_4$ . - 78 -

Figure 5-1: Three powders used in this study: (a) sample A,  $\text{Li}_{1-x}\text{FePO}_4$  having 34nm average particle size as determined from the BET specific surface area, (b) sample C,  $\text{LiFePO}_4$  having 113 nm average size, and (c) sample M,  $\text{Li}_{1-x}\text{MnPO}_4$  having 78 nm average particle size. The specific capacity vs. C-rate is shown for samples A and C. .... - 101 -

Figure 5-2: Time dependence of OCV of (A) sample A after charging to various states of charge, SOC; (B) sample A after discharging to various states of discharge, SOD; and (C) sample C after charging to various SOC. A relaxation of the OCV that takes place over as long as 100 h is seen in sample A, and over 20-40 h for sample C. The relaxed value of OCV is seen to be a function of SOC and SOD. .... - 102 -

- Figure 5-3: (A) Temperature dependent miscibility data for samples A and C from ref 7 plotted against the equilibrium phase diagram of Dodd et al..<sup>6</sup> (B) Room temperature terminal OCV and galvanostatic voltage curve at C/50 rate measured on both charging and discharging of sample A. (C) Terminal OCV and C/50 galvanostatic charge curves measured at room temperature as a function of state-of-charge for samples A and C..... - 103 -
- Figure 5-4: Results for sample C showing nearly ideal two-phase reaction. (A) XRD spectra taken as a function of state-of-charge from starting material to 95% SOC with “H” representing heterosite, “T” representing triphylite, and C denoting the graphite (002) reflection from carbon additive in the electrode formulation. Only a portion of the full spectra obtained from 15° to 135° 2-theta are shown. (B) Unit cell volumes and the normalized crystalline phase fraction of triphylite (unfilled symbols) and heterosite (filled symbols). (C) Galvanostatic voltage curve at C/50 measured at room temperature..... - 104 -
- Figure 5-5: Results showing phase evolution in nanocrystalline sample A. (A) XRD spectra taken as a function of state-of-charge, from starting material to 100% SOC. Only a portion of the full spectra obtained from 15° to 135° 2-theta are shown. (B) Unit cell volumes and the crystalline phase fraction of  $\text{Li}_y\text{FePO}_4$  (filled symbols) and  $\text{Li}_{1-x}\text{FePO}_4$  (unfilled symbols). The nonstoichiometry parameters x and y calculated from Vegard’s law are given next to each unit cell volume datum. (C) Galvanostatic voltage curve measured at C/50 rate at room temperature. The phase boundaries measured in ref 7 by electrochemical (PITT) and x-ray diffraction (Vegard’s law) techniques are shown as shaded vertical lines.- 105 -
- Figure 5-6: XRD spectra of sample M in its starting state and after charging to composition  $\text{Li}_{0.60}\text{MnPO}_4$ . The sample exhibits broadened peaks for the delithiated  $\text{Li}_y\text{MnPO}_4$  (labeled “P”) phase indicating that the newly formed phase is highly disordered. .... - 106 -
- Figure 5-7: Phase transformation pathways between lithiated and delithiated phases in  $\text{LiMPO}_4$  olivines. .... - 107 -
- Figure 6-1: Sample preparation and firing schedule of the studied materials. .... - 128 -
- Figure 6-2: Lattice parameters and unit cell volumes for four dopants each at 5 at% overall doping level, formulated according to Mechanisms 1-5, compared to the undoped control sample (dashed horizontal line). Values are from Rietveld refinements of X-ray diffraction spectra. The unit cell parameters increase as the valence of the dopant increases; Mechanism 1 in which the solute substitutes onto the M1 site with charge compensation by Li vacancies gives the largest unit cell expansion ..... - 128 -
- Figure 6-3: a) X-ray diffraction spectra for samples with varying Zr doping level showing olivine (O), NASICON (N), and trace  $\text{Fe}_2\text{P}_2\text{O}_7$ (F). High-quality spectra ( $R_{\text{exp}} \sim 1.5\%$ ) were collected using a Rigaku RTP500RC instrument at scan rates of  $0.18^\circ \text{ min}^{-1}$  over the  $2\theta$  range from 15° to 135°. Limited  $2\theta$  ranges are shown on an expanded scale for clarity. Lines for NASICON phases of several compositions are shown for

comparison. With increasing Zr content, the single NASICON phase in the sample increases in amount and exhibits a peak shift to lower angles indicating increasing Zr content in this phase. b) Unit cell volume expansion for Zr-doped samples shows nearly linear increase with increasing Zr doping level up to 10% without saturation. ....- 129 -

Figure 6-4: STEM composition maps of the 5 mol % Zr sample, doping according to mechanism 1, showing that Zr is uniformly detected in the crystallites.- 130 -

Figure 6-5: Rietveld-refined phase fractions ( : Olivine, : NASICON) and unit cell volumes ( : Olivine, : NASICON) for olivine and NASICON in Zr-doped compositions prepared according to defect mechanism 1. As is permitted by the Gibbs phase rule, the relative amounts and unit cell volumes (reflecting Zr concentration) vary continuously as the overall Zr doping level is increased. Thus the solubility of Zr in both phases increases with Zr content. ....- 131 -

Figure 6-6: Olivine unit cell volume vs. firing temperature for a 7.5% Zr-doped composition, compared to results for undoped LiFePO<sub>4</sub>. The unit cell volume decreases slightly upon coarsening of the particle size to >1 μm from an initial average particle size of 45 nm (determined from BET measurement), but remains significantly greater than that for the undoped sample, showing that the solid solubility of Zr is slightly size-dependent. ....- 132 -

Figure 6-7: An example of neutron diffraction spectrum from a 5 mol% Zr sample doped according to Mechanism 1. Two additional neutron and one XRD spectra were simultaneously refined according to the following models: a) (Li<sub>0.845</sub>Zr<sub>0.043</sub>Δ<sub>0.112</sub>)(Fe<sub>0.979</sub>Δ<sub>0.021</sub>)PO<sub>4</sub>; b) stoichiometric LiFePO<sub>4</sub>; c) Li(Fe<sub>0.90</sub>Zr<sub>0.05</sub>Δ<sub>0.05</sub>)PO<sub>4</sub>; and d) (Li<sub>0.8</sub>Zr<sub>0.05</sub>Δ<sub>0.15</sub>)FePO<sub>4</sub>. Δ represents vacant lattice sites. The observed intensity data are shown by the solid line, and the overlying dotted line is the calculated intensity. Vertical markers below the diffraction patterns indicate positions of possible Bragg reflections. Differences between the observed and calculated intensities are plotted in the same scale. The best goodness-of-fit (smallest R<sub>wp</sub>, R<sub>p</sub>, and χ<sup>2</sup> parameters) is obtained for models a) and d) in which the Zr is assumed to occupy the M1 sites, and especially for model a) in which the Zr site concentration is allowed to vary. ....- 133 -

Figure 6-8: Curved Li migration path in the olivine [010] direction <sup>3, 21, 22</sup>, for comparison with the Li-O and O-O bond length changes in Table 6-II. Note that the diffusion path lies out of the x-y plane and passes through O1-O2-O3 triangle. ....- 134 -

Figure 6-9: Capacity versus voltage measured potentiostatically upon charge and discharge in 5 mV steps for the 5 mol% Mg doped nanoscale sample (bottom). Solid solubility regions x,y can be measured and calculated from the accumulated capacities below and above the OCV for x in the Li-rich Li<sub>1-x</sub>FePO<sub>4</sub> phase and y in the Li-poor Li<sub>y</sub>FePO<sub>4</sub> phase, respectively. The solid solubility x and y are calculated to be 10.6% and 13.3%, respectively. PITT responses of the undoped control sample, the

conventional coarse-grained sample, and 1% Nb doped nanoscale sample were plotted for comparison (top). .....- 135 -

Figure 6-10: Comparative phase diagram shows the miscibility gap contraction of nanoscale Mg and Nb doped samples as compared to the undoped control of similar particle size (42 nm) and a coarser conventional powder (113nm), each measured using the same PITT protocol. The equilibrium phase diagram for bulk  $\text{Li}_{1-x}\text{FePO}_4$  (micron size) published by Dodd et al. <sup>16</sup> is also shown for comparison. ....- 136 -

Figure 6-11: Potentiostatic intermittent titration tests (PITT), showing 5 mV voltage steps (blue) and corresponding current relaxation (red). a) 5% Mg doped sample during charge; b) 5% Mg doped sample during discharge; c) Undoped sample during charge; d) Undoped sample during discharge. The 5% Mg-doped nanoscale sample exhibits a characteristic of fast phase transformation with a peak current at the start of each voltage step followed by monotonically decay, at all overpotentials. The undoped sample exhibits slower rate of current decay and, at some potentials, rise in current as a phase transformation barrier is overcome. The cut-off currents were C/100 for the 5% Mg doped sample and C/200 for the undoped sample, respectively. ....- 137 -

Table 6-I. Ideal crystal compositions and defect compensations mechanisms tested, with  $\text{M}^{n+}$  substituting on M1 and/or M2 sites.  $\text{M}^{n+}$  represents  $\text{Mg}^{2+}$ ,  $\text{Al}^{3+}$ ,  $\text{Zr}^{4+}$  or  $\text{Nb}^{5+}$  ions. ....- 138 -

Table 6-II: Rietveld refined site occupancies (g), atomic coordinates (x, y, z) and thermal parameters for a 5% Zr doped sample doped according to defect mechanism 1. The site occupancies correspond to an approximately charge-neutral composition of  $(\text{Li}_{0.845}\text{Zr}_{0.043}\Delta_{0.112})(\text{Fe}_{0.979}\Delta_{0.021})\text{PO}_4$ . Lattice parameters also shown. ....- 139 -

Table 6-III: Goodness-of-fit parameters and bond lengths of doped compositions based on defect Mechanism 1, M1 site doping with M1-site vacancy compensation mechanism, compared to undoped control sample. The  $\text{Mg}^{2+}$  results are for a 10% doping level while the  $\text{Al}^{3+}$ ,  $\text{Zr}^{4+}$  and  $\text{Nb}^{5+}$  results are for 5% doping level. Systematic expansion of the oxygen-oxygen and lithium-oxygen bond lengths is observed upon doping at these levels. ....- 140 -

# Chapter 1

## Motivation

Lithium-ion batteries have improved performance in a wide variety of mobile electronic devices such as communication devices, multimedia players, and laptop computers (Figure 1-1). They have higher volumetric and gravimetric energy densities than other competing battery technologies, such as lead-acid, nickel cadmium (NiCd), or nickel-metal hydride (NiMH). This enables lighter and smaller battery packs. New fields of applications, such as power tools, plug-in hybrid electric vehicles (PHEVs), hybrid electric vehicles (HEVs), all-electric vehicles (EVs), renewable electrical energy storage, and electric grid stabilization, require that Li-ion batteries have high safety, durable high power, long life and low cost. For hybrid vehicles, the materials in the rechargeable battery must have durable high power being able to discharge fast so that the vehicles can accelerate quickly or to charge sufficiently fast to take advantage of regenerative braking, otherwise much of the fuel savings are lost. Li-ion batteries are viewed today as the most viable electric-vehicle battery chemistry due to their superior performance over other battery technologies. Some examples of battery packs currently available for electric vehicles applications are given in Figure 1-2. In such high-power applications, the phase behavior and phase transformation kinetics of the materials used in the batteries are critical to the electrochemical performance.

Lithium-ion batteries operate by an electrochemical process in which lithium ions are shuttled between two host electrodes (cathode and anode) during charge and discharge. A typical Li-ion battery contains a cathode, anode, electrolyte, and separator (Figure 1.3). The separator is a polymeric film used to prevent short circuits between the cathode and the anode. The electrolyte is an electronic insulator but an ionic conductor (i.e. it only allows ions to pass, but electrons normally are blocked). During discharge, an electrical circuit is formed, the anode material oxidizes, or gives up electrons, while the cathode material (in this case lithium cobalt oxide), immersed in an electrolyte, becomes reduced,



or gains electrons. Lithium ions move from the anode to the cathode to neutralize these charges. The reactions can thus continue and the electrons continue to flow, providing electrical energy to the connected device. During charging, the process is reversed: the cathode and the anode are oxidized and reduced, respectively. The electrical energy is restored to the battery. Ideally, intercalation or de-intercalation during cycling of lithium ions should leave the host structure intact. In practice, however, variation in lithium concentrations can lead to structural changes involving several phase transformations and/or volume changes. Examples of intercalation compounds that undergo a volume change with composition (because the ions occupy interstitial sites), include materials cycled predominantly within a solid solution field such as  $\text{LiCoO}_2$  and  $\text{LiMn}_2\text{O}_4$ . The compounds that undergo a first-order phase transformation include the olivines  $\text{LiMPO}_4$  ( $M = \text{Mn, Fe, Co, Ni}$ ),  $\text{Li}_4\text{Ti}_5\text{O}_{12}$ , and the “lithiated spinel”  $\text{Li}_2\text{Mn}_2\text{O}_4$ . Extensive research efforts have focused on understanding these structural changes in the lithium transition metal compounds and their effects on electrochemical properties. Understanding this relationship is critical for developing new materials as well as optimizing electrochemical performance of existing materials.

The main objectives of this research are to study the impact of phase behavior and phase transformation kinetics during electrochemical cycling on electrochemical properties such as voltage profile, cycle life, and rate capability, and how these are affected by particle size and compositions. We choose to use lithium transition metal olivine compounds  $\text{LiMPO}_4$  ( $M = \text{Fe, Mn}$ ) as our model materials, because they represent a class of cathode materials of great interest to the battery community due to their high potential uses in EV, HEV, and PHEV applications.

The energy output of lithium rechargeable batteries is dependent on the voltage upon which lithium ions are inserted and the number of sites that can accommodate the ions in the host structure. The theoretical voltage of a battery is determined by the type of active materials it contains. The value can be calculated from free energy data or obtained experimentally. The voltage is dependent on many factors, including concentration and temperature, as described by the Nernst equation:

$$E = E^0 - \frac{RT}{nF} \ln \frac{[\text{reduction}]}{[\text{oxidation}]} \quad \text{Equation 1}$$

Where R = gas constant

T = absolute temperature

F = Faraday's constant (96,485 C.mol<sup>-1</sup> = 26.8 Ah.mol<sup>-1</sup>)

E<sup>0</sup> = standard potential at 25°C

n = number of moles of electrons in the reaction (for lithium cells, n = 1)

[Reduction] and [oxidation] = molar concentrations of the ions of the substance being reduced and oxidized.

The cell potential ( $\Delta E^0$ ) is determined by the thermodynamics of the system, and it is related to the Gibbs free energy of the system by the expression:

$$E - E^0 = \Delta E^0 = \frac{-\Delta G}{nF} \quad \text{Equation 2}$$

The free energy is related to the chemical potentials  $\mu$  of the reactants i, as

$$\Delta G = \sum_i v_i \mu_i \quad \text{Equation 3}$$

where  $v_i$  are coefficients of the i<sup>th</sup> reactants in the electrochemical reaction. For substances formed, v is positive, and for substances consumed v is negative. Since

$$\Delta E^0 = -\frac{1}{nF} \sum_i v_i \mu_i \quad \text{Equation 4}$$

the cell voltage is thus obtained from the chemical potentials of the reactants in the cell.

When a steady current is applied to the electrode upon charging, the voltage or potential of the cathode moves to a value characteristic of the reactive couple and varies with time as the ratio of concentration changes at the electrode interface. For the olivine compounds (LiMPO<sub>4</sub>, M = Fe, Ni, Mn, Co), the model of two-phase coexistence between lithiated and delithiated phases during charge and discharge, according to which a constant

potential or open-circuit-voltage (OCV) vs.  $\text{Li}/\text{Li}^+$  is thermodynamically required, has been widely accepted in the battery community. However, any additional contributions to free energy can have an effect on the absolute value of OCV. Therefore, a study of equilibrium voltage could provide some useful thermodynamic information about this system. Moreover, metastable behavior may exist during lithium insertion and de-insertion of these compounds; therefore, a more complex model is required in order to be able to fully explain the phase behavior of the compounds under different cell environments and electrochemical use conditions.

The impact of phase behavior and phase transformation kinetics on cycle life is unclear. Lithium insertion/ extraction in intercalation compounds should leave the structures unchanged regardless of its type. However, it has been observed that variation in lithium content during repetitive cycling can lead to lattice expansion and contraction of the host structures. This intercalation process has thus been expected to induce structural damage or irreversible phase changes that could lead to poor cycle life or decrease the energy output of lithium rechargeable batteries.

Olivine compounds have the advantages of low cost, high thermal stability, non-toxicity, reasonably high energy density, and high energy capacity. However, the practical use of these compounds as cathode materials for lithium rechargeable batteries was initially limited due to its poor rate capability. Recently, significant efforts have been made to compensate for these shortcomings. Examples are coating with an electron-conducting phase (mostly carbon), particle size minimization, and/or aliovalent doping. This has permitted commercialization of  $\text{LiFePO}_4$  as a cathode material in batteries. Despite its commercialization, the mechanisms allowing high power in these compounds are still extensively debated. It is one of the objectives of this study to understand these mechanisms.

# Thesis Outline

The main objective of this thesis is to understand the correlation between particle size, composition (doping), phase behavior and phase transformation kinetics, and their relation to practical properties for the  $\text{LiMPO}_4$  cathode compounds. This study has been carried out in several stages as will be reported in the following chapters. Chapter 2 will present an overview of olivine compounds as cathode materials, which includes overall characteristics, crystal structure, and electrochemical storage mechanism of these compounds. We expect that there may be fundamental differences such as phase stability, phase transformations, and lithium transport kinetics between nanoscale particles and their bulk counterparts; we therefore propose to study the effect of particle size on phase diagram of this system. The results are shown in Chapter 3. We discovered that when  $\text{LiFePO}_4$  is fabricated in nanoscale form, the phase diagram is changed dramatically. There is much greater extent of solid solution in both the Li-poor and Li-rich coexisting phases. In other words, the miscibility gap is contracted. We found that the miscibility gap shrinks dramatically with decreasing particle size and increasing temperature. And for the doped nanoscale powder, the lithium nonstoichiometry parameters are 2 times larger than for the undoped powder of equivalent size (Chapter 4). There is much less lattice mismatch between the two co-existing phases observed as well. We believed that these changes in phase stability of the materials would have the following effect on properties:

- Co-existence of  $\text{Fe}^{2+}/\text{Fe}^{3+}$  in both phases improves electronic conductivity and rate capability
- Lower transformation strain when cycling, since there is much less lattice mismatch between the two co-existing phases. This would allow more facile phase transformation, and provide for higher rate capability and longer cycle life.

In fact, the mechanisms allowing high power in these compounds have been extensively debated. Numerous studies have attributed the rate capability of olivines purely to chemical diffusion limitations. However, as mentioned previously, and to be explained

further in the later chapters, this class of olivines undergoes a first-order phase transition upon electrochemical cycling. We thus reasoned that an equally important goal should be to maximize the rate of phase transformation, regardless of the rate-limiting step. We propose a model, suggesting by correlations between lattice misfit and rate capability, that in order to provide high power and long life characteristics for lithium rechargeable batteries, the electrode materials must exhibit small elastic misfits between the parent and daughter phases to allow facile phase transformation during electrochemical cycling. Up to now, we know of no counterexamples in which high rate capability is obtained for a phase transformation of large misfit. The model (in collaboration with Prof. Carter's group) demonstrating the role of this "nanomechanics" on battery performance is treated in detail, and the supporting experimental results are given in Chapter 4.

The topic of phase behavior and transport properties of the olivine compounds is very interesting. Many of these unconventional phenomena have yet to be fully understood and will remain to be one of the fruitful topics for battery researchers to explore and discuss. Chapter 5 shows further interesting behavior that arises from downsizing the particles- the phase-transformation pathway of nanoscale materials becomes much more complex and involves transformation to amorphous and/or metastable phase(s). It is well known that a key feature of the  $\text{Li}_x\text{FePO}_4$  cathode is its extremely flat charge/discharge profile. This is categorized as typical of two-phase reaction systems, even though the composition and amounts of the two phases can be varied. Finely-resolved equilibrium voltage measurements can provide insights on how thermodynamics of the phase co-existence changes with particle size. In fact, we found that phase transformation path differs significantly between the nanosized ( $< 40$  nm) and "conventional" coarse-grained ( $> 100$  nm) materials. Whereas coarse-grained  $\text{LiFePO}_4$  undergoes a conventional two-phase reaction in which crystalline  $\text{LiFePO}_4$  and  $\text{FePO}_4$  co-exist, in nanoscale samples the following are observed: (1) there is a reduced miscibility gap between co-existing crystalline phases as shown previously; and (2) upon charge, a fraction (increasing with increasing particle size) of the crystalline delithiated  $\text{Li}_y\text{FePO}_4$  that is formed is partially amorphous and metastable.

Isovalent substitutions have been a highly successful route to structure and property optimization in intercalation compounds used as lithium storage electrodes for rechargeable lithium batteries. For example in the ordered rock salts  $LiMO_2$  compounds,  $Ni^{2+}$  and/or  $Mn^{2+}$  (i.e.  $LiCo_xNi_{1-x}O_2$ ,  $LiCo_{1/3}Ni_{1/3}Mn_{1/3}O_2$ ) have been used to replace expensive  $Co^{2+}$  or for spinels  $LiM_2O_4$ ,  $LiNi_xMn_{2-x}O_4$  has been produced to provide better structural stability. However, the possibility for, and role of, aliovalent doping with appropriate charge-compensating point defects of the olivines, which may have as great or greater impact on structure and transport properties as isovalent substitutions, has been widely debated. In Chapter 6, we carry out critical tests of the plausible defect compensation mechanisms using compositions designed to accommodate  $Mg^{2+}$ ,  $Al^{3+}$ ,  $Zr^{4+}$ ,  $Nb^{5+}$  ions on the M1 and/or M2 sites of  $LiFePO_4$  with appropriate charge-compensating defects, and obtain conclusive crystallographic evidence for lattice doping. Structural and electrochemical analyses show that doping can induce a reduced lithium miscibility gap, increased phase transformation kinetics during cycling, and expanded Li diffusion channels in the structure. These have also been discussed throughout this thesis. We showed in Chapters 3, 4, and 6 that phase transformation kinetics as determined from time resolved electrochemical and structural measurements were different among nanoscale, conventional, and doped nanoscale samples.

## Chapter 1 Figures and Tables



**Figure 1-1: Lithium-ion batteries for various applications including portable electronics, power tools, and electric vehicles.**



**Figure 1-2: Example of battery packs for electric vehicle applications**

Source: National Renewable Energy Laboratory

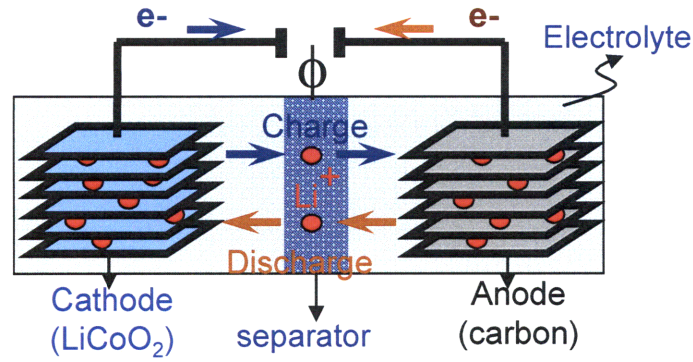


**Figure 1-3: Electrochemical processes in Li-ion batteries during charging and discharging. During discharge, an electrical circuit is formed, the anode material (in this case lithiated carbon) oxidizes, or gives up electrons, while the cathode material (in this case lithium cobalt oxide) immersed in an electrolyte becomes reduced, or gains electrons. Lithium ions move from the anode to the cathode to provide charge neutrality so that the reactions can continue and the electrons can keep flowing providing electrical energy to the connected device. During charge, the process is reversed: the cathode and the anode are oxidized and reduced, respectively. The electrical energy is restored to the battery.**



# Chapter 2

## Background on Olivine Compounds

Many families of compounds have been developed for use as cathode materials in Li-ion batteries, such as layered oxides  $\text{LiMO}_2$  ( $M = \text{Co, Ni, Mn, or V}$ ), manganese spinel ( $\text{LiMn}_2\text{O}_4$ ), and phospho-olivines  $\text{LiMPO}_4$  ( $M = \text{Fe, Mn, Co, or Ni}$ ). Lithium cobalt oxide is the most common cathode used in Li-ion batteries today; however, the high cost of cobalt and safety concerns make it impractical for some applications such as electric vehicle applications. Olivine-type cathodes have become of particular interest for transportation and energy applications ranging in size scale from hybrid and plug-in hybrid electric vehicles to utilities-scale power regulation due to its low cost (substituting of expensive cobalt with cheaper and more abundant iron or manganese), high safety, high thermal stability, and environmentally friendly characteristics. This family of compounds is the focus of this thesis.

The crystal structure of  $\text{LiMPO}_4$  is well-known and described by the space group  $P nma$ . Figure 2-1 shows the crystal structure of  $\text{LiFePO}_4$ . The structure is based on a nearly close-packed (hcp) arrangement of oxygen. Iron (Mn, Co, and Ni in the case of other olivines) is located in a slightly distorted  $\text{FeO}_6$  octahedron. Lithium is located in a second set of octahedral sites ( $\text{LiO}_6$ ) which are distributed differently. Phosphorous is located inside the tetrahedral sites. The  $\text{LiO}_6$  octahedron shares edges with four other octahedra, and  $\text{FeO}_6$  shares edges with two octahedra and corners with three  $\text{PO}_4$  tetrahedra.

The first published work describing the use of a lithium metal phospho-olivine as the positive electrode in a lithium rechargeable battery appears to be by Kamauchi et al.,<sup>1</sup> who specified the compound  $\text{LiCoPO}_4$  as well as other transition metal substitutions. Most researchers have first become aware of this family of compounds through the work of Padhi et al.<sup>2</sup> Olivine  $\text{LiMPO}_4$  ( $M = \text{Fe, Mn, Co, Ni}$ ) compounds have gained attention from battery research community because of their several advantages, such as high theoretical capacity, 170 mAh/g, and flat discharge plateaus at 3.45 V, 4.10 V, 4.80 V,

and 5.10 V (vs. Li/Li<sup>+</sup>), respectively for Fe, Mn, Co, and Ni. Among these, LiFePO<sub>4</sub> has received the most attention to date as it has the highest potential to provide reasonably high energy density, low price, good cycling stability, good thermal stability, and low toxicity.<sup>2</sup> However, pure LiFePO<sub>4</sub> also has several drawbacks, such as low electronic conductivity on the order of 10<sup>-9</sup> S cm<sup>-1</sup>, and slow Li-ion transport during the LiFePO<sub>4</sub>/FePO<sub>4</sub> phase transformation during the charge-discharge process<sup>2-4</sup> resulting in poor rate capability and making the practical utility of these compounds initially unclear. Many efforts have been devoted to improving the conductivity of LiFePO<sub>4</sub>, as well as the rate performance of LiFePO<sub>4</sub> cathodes, such as adding-coating conductive media in the LiFePO<sub>4</sub> cathodes to increase the conductivity,<sup>6-9</sup> synthesizing nanoscale particles to shorten the Li transport length,<sup>10,11</sup> forming a percolating nano-network of metal-rich phosphides<sup>12</sup> to improve electronic conductivity or doping the LiFePO<sub>4</sub> with other transition metals.<sup>13,14</sup> After Chung et al.<sup>5</sup> demonstrated high charge capacity at charge/discharge rates well above 5C in doped nanoscale LiFePO<sub>4</sub> (e.g., 115 mAh/g for 6 min continuous discharge (20C rate)) at room temperature, interest in this material grew rapidly as reflected by a large increase in the number of publications from about 30 publications published between 1997-2001 to about 150 publications published between 2002-03 and more than 1800 publications published between 2002- 2008.

One of the key features of the LiFePO<sub>4</sub> cathode is its extremely flat charge/discharge voltage vs. capacity curve categorized as typical of two-phase reaction systems. When cycling at room temperature, the two phases are a lithiated triphylite phase, LiFePO<sub>4</sub>, and a delithiated heterosite phase, FePO<sub>4</sub>. Both phases are olivine-type orthorhombic structures, with the differences being the presence of lithium chains in the triphylite structure as shown in Figure 2-2. The lattice parameters for each phase are given in Table 2-I.<sup>15</sup> In the literature, a core-shell reaction whereby the newly formed phase uniformly coats the preexisting phase during lithium intercalation/de-intercalation has been widely applied. Srinivasan and Newman<sup>15</sup> have found a continuous deviation of the OCV from the plateau value of 3.45 V at both the beginning (0 < x <ca. 0.03) and end (ca. 0.96 < x < 1) of the charge/ discharge reaction. Combined with their mathematical expression, it was suggested that there would be a corresponding monophasic region, where the overall

reaction scheme can be represented as Figure 2-3 with the previously published charge-discharge curves measured at C/20 rate.<sup>16, 18</sup> (Note that charge/discharge rates are usually reported in C-rate convention, or C/n, where n is the time in hours for complete charge or discharge of the nominal capacity measured. In this case, C/20 rate means that it takes 20 hours to completely charge the cell to the cut-off voltage). Most of the electrode reaction is dominated by the two-phase coexistence of  $\text{Li}_\alpha\text{FePO}_4$  and  $\text{Li}_{1-\beta}\text{FePO}_4$  but with very narrow monophasic regions ( $0 < x < \alpha$  and  $1-\beta < x < 1$ ) close to the stoichiometric end members of  $\text{LiFePO}_4$  and  $\text{FePO}_4$  at room temperature. These nonstoichiometric parameters  $\alpha$  and  $\beta$  in the two phase region are convenient diagnostics for the electrode activity because they are directly linked with the density of lithium defect and  $\text{Fe}^{3+}/\text{Fe}^{2+}$  mixed valence state and hence the hopping probability of both of lithium ions and polarons. The straightforward estimation of the nonstoichiometric parameters  $\alpha$  and  $\beta$  of  $\text{Li}_x\text{FePO}_4$  ( $0 < x < 1$ ) phases at room temperature has been demonstrated using Rietveld refinement of X-ray diffraction profiles and found to be  $\alpha \sim 0.03$  and  $\beta \sim 0.04$ . In follow-up experiments<sup>20</sup>, neutron diffraction measurements indicated site occupancies of lithium to be  $\alpha = 0.05$  and  $1-\beta = 0.89$ . Higher temperature investigations of the  $\text{Li}_x\text{FePO}_4$  phase diagram by Delacourt et al.<sup>21</sup> and by Dodd et al.<sup>22</sup> confirm the low temperature immiscibility, but also find an unusual eutectoid point at 150 °C<sup>20</sup> or 200 °C<sup>21</sup> where the solid solution phase emerges around  $x \sim 0.45 - 0.65$ . Above 300 – 400 °C, a solid solution occurs for all compositions. This phenomenon was explained by Zhou et al.<sup>23</sup> They used first-principles LDA+U calculations and Monte Carlo simulations to determine the phase diagram based on a coupled cluster-expansion model, and found that while transformations from low-T ordered or immiscible states are almost always driven by configurational disorder (i.e. random occupation of lattice sites by multiple species), in  $\text{FePO}_4$ - $\text{LiFePO}_4$  the formation of a solid solution is almost entirely driven by electronic configurational entropy. Panels a and b of Figure 2-4 show the phase diagram of conventional coarse grained-powder studies by Dodd et al.<sup>22</sup> and by Delacourt et al.,<sup>21</sup> respectively. Figure 2-4c shows the calculated phase diagram by Zhou et al.<sup>23</sup> taking into account the effect of electronic configurational entropy.

## **Background on Experimental Techniques**

In order to understand the results presented later, a description of the experimental techniques including electrochemical measurements, structural analysis based on X-ray and neutron diffraction, and electron microscopy are presented here.

### Electrochemical Measurement: Galvanostatic Cycling

Galvanostatic charging and discharging requires the application of a constant current over a range of voltage. Voltage is allowed to change freely depending on chemical reactions that occurred within that voltage range; therefore, this technique can provide information on the kinetics and mechanisms of electrode reactions. Unless noted otherwise throughout this thesis, the voltage limits were 2.0 – 4.2 V for the lithium iron phosphate samples, and 2.0 - 4.5 V for the lithium manganese phosphate. For a system that shows two co-existing phases during electrochemical cycling such as the olivines, slow galvanostatic cycling can be used to determine the solid solution limits from the deviation in voltage with state-of-charge, even though with this technique some polarization always present, introducing inaccuracy in measuring the solid solution limit.

### Electrochemical Measurement: Intermittent Titration Techniques

The Galvanostatic Intermittent Titration Technique (GITT) is a common technique used to establish the thermodynamic voltage as a function of composition. It is considered to be a more accurate method for determining the solid solution limit than galvanostatic cycling. In this technique, the voltage relaxation after the application of constant current pulses is measured. However, in systems having a first-order phase transition, such as in olivine compounds, the current pulsing needed in GITT inherently leads to an increase in overpotential during the pulse, which could introduce hysteresis effects due to the nucleation or growth of a new phase.

The Potentiostatic Intermittent Titration Technique (PITT) is a technique in which current relaxation after the application of voltage steps is measured. For determining

solid solution limits, the capacities above and below the open-circuit voltage corresponding to two-phase co-existence is measured. We consider the PITT measurements to be more exacting when there is true two-phase co-existence since they measure the extent of nonstoichiometry without any overpotential. Also, during two-phase co-existence, the current measured in PITT is exactly linear to the phase transformation rate, assuming that there is no capacitive current, or short circuit, or other regions of lithium accumulation in the sample. Therefore, PITT can provide a direct measure of each sample's transformation rate as a function of the applied potential as well.

#### Electrochemical Measurement: Cyclic Voltammetry

Cyclic Voltammetry or CV is a potentiodynamic electrochemical measurement in which the potential is ramped linearly versus time; this ramping is known as the experiment's scan rate (V/s). From the current measured vs. potential, information about the redox potential and electrochemical reaction rates of the compounds can be obtained. For example, a sharp increase in current typically indicates a redox process is occurring. As another example, if the electronic transfer at the surface is fast and the current is limited by the diffusion of species to the electrode surface, then the current peak will be proportional to the square root of the scan rate.

#### Diffraction and Rietveld Refinement

X-ray diffraction is one of the most common techniques applied to battery materials to obtain information on how structures change under particular circumstances. In addition to lattice constants, we can obtain the relative strain and crystallite size of each phase, and in ex-situ or in-situ experiments, can do this as a function of composition. Neutron diffraction is a method for determining atomic structure with greater precision than is possible in X-ray diffraction. Complementary to X-ray radiation neutron radiation is most sensitive to detect "light" elements. However, in general, it is very difficult to calibrate a neutron diffractometer well enough to trust the absolute lattice parameters (the relative ones are usually excellent). This is especially true for TOF (Time-of-Flight)

diffractometers. There are many reasons for this, including sample position and transparency effects. Thus, x-ray diffraction is a more accurate method to measure lattice constants. Rietveld refinement is a standard method for obtaining structural parameters of materials by fitting experimental spectra to theoretical profiles calculated for numerous materials and instrumental variables. Both diffraction techniques and their Rietveld refinements are used in this thesis to study the structural changes during electrochemical tests, as well as the effects of aliovalent substitutions on the structure of the olivine materials.

### Electron Microscopy

Transmission Electron Microscope (TEM) can be used to obtain morphology, composition, and crystallographic information on materials. Transmission Electron Microscopy is used to study how the olivine materials change under specific electrochemical circumstances. Information on defects in these materials before and after cycling is necessary to fully explain the phase transformation mechanism, the transformation rate, and fatigue and fracture. Unless noted otherwise TEM work in this research was done with help from Y.H. Kao in Prof. Chiang's group.

### **References**

1. Kamauchi et. al. US Patent US005538814, July 23, 1996.
2. A. K. Padhi, K. S. Nanjundaswamy, and J. B. Goodenough, *J. Electrochem. Soc.*, **144**, 1188 (1997).
3. A. Yamada, S.C. Chung, *J. Electrochem. Soc.*, **151**, A1352 (2004).
4. C. Delacourt, L. Laffont, R. Bouchet, C. Wurm, J.-B. Leriche, M. Morcrette, J.-M. Tarascon, C. Masquelier, *J. Electrochem. Soc.*, **152**, A913 (2005).
5. S.Y. Chung, J.T. Bloking, Y.M. Chiang, *Nat. Mater.* **1**, 123 (2002).
6. N. H. Kwon, T. Drezen, I. Exnar, I. Teerlinck, M. Isono, M. Graetzel, *Electrochem. Solid State Lett.* **9**, A277 (2006).
7. K. Streibel, J. Shim, V. Srinivasan, J. Newman, *J. Electrochem. Soc.* **52**, A664 (2005).

8. C. Delacourt, C. Wurm, L. Laffont, F. Sauvage, J.-B. Leriche, R. Bouchet, M. Morcrette, J.-M. Tarascon, C. Masquelier, **2004**, *Proc. MRS Fall Meeting 2004* 321.
9. H. Huang, S.C. Yin, L.F. Nazar, *Electrochem. Solid-State Lett.*, **4**, 170 (2001).
10. J. Barker, M.Y. Saidi, J.L. Swoyer, *Electrochem. Solid-State Lett.*, **6**, 53 (2003).
11. N. Ravet, A. Abouimrane, M. Armand, *Nature Mater.* **2**, 702 (2003).
12. P. Subramanya Herle, B. Ellis, N. Coombs, L. Nazar, *Nature Mater.*, **3**, 147 (2004).
13. J. F. Ni, H. H. Zhou, J. T. Chen, and X. X. Zhang, *Mater. Lett.*, **59**, 2361 (2005).
14. G.-H. Li, H. Azuma, and M. Tohda, *J. Electrochem. Soc.*, **149**, A743 (2002).
15. S. Andersson, B. Kalska, L. Haggstrom, J.O. Thomas, *Solid State Ionics*, **130**, 41 (2000).
16. C. Delacourt, P. Poizot, J.-M. Tarascon, C. Masquelier, *Nature Mater.* **4**, 254 (2005).
17. V. Srinivasan, J. Newman, *J. Electrochem. Soc.*, **151**, A1517 (2004).
18. M. Yonemura, A. Yamada, Y. Takei, N. Sonoyama, and R. Kanno, *J. Electrochem. Soc.*, **151**, A1352 (2004).
19. A. Yamada, H. Koizumi, N. Sonoyama, and R. Kanno, *Electrochem. Solid-State Lett.*, **8**, A409 (2005).
20. A. Yamada, H. Koizumi, S. I. Nishimura, N. Sonoyama, R. Kanno, M. Yonemura, T. Nakamura, and Y. Kobayashi, *Nat. Mater.*, **5**, 357 (2006).
21. C. Delacourt, P. Poizot, J. M. Tarascon, and C. Masquelier, *Nat. Mater.* **4**, 254 (2005).
22. J. L. Dodd, R. Yazami, and B. Fultz., *Electrochem. Solid-State Lett.*, **9**, 3, A151 (2006).
23. F. Zhou, T. Maxisch, and G. Ceder., *Phys. Rev. Lett.*, **97**, 155704 (2006).

## Chapter 2 Figures and Tables

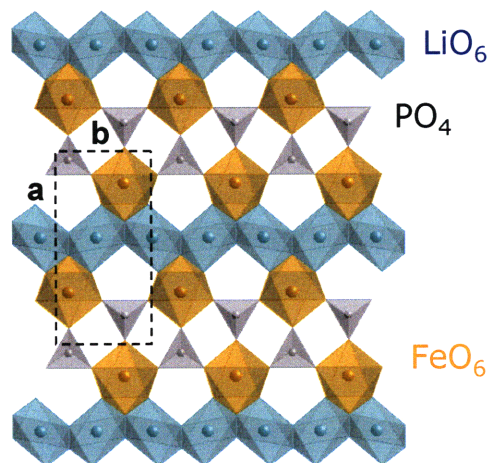


Figure 2-1: Polyhedral representation of olivine  $\text{LiFePO}_4$  structure projecting along the  $[001]$  direction.

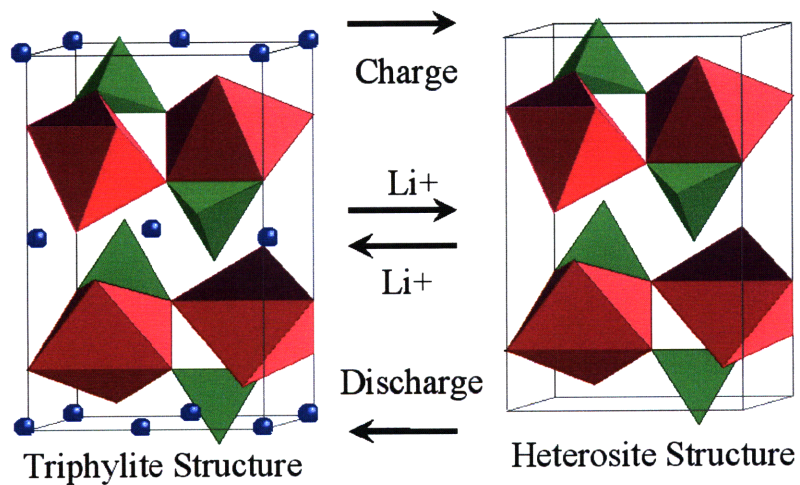


Figure 2-2: Schematic representation of the system during cycling showing the two phase end-members; triphylite and heterosite.



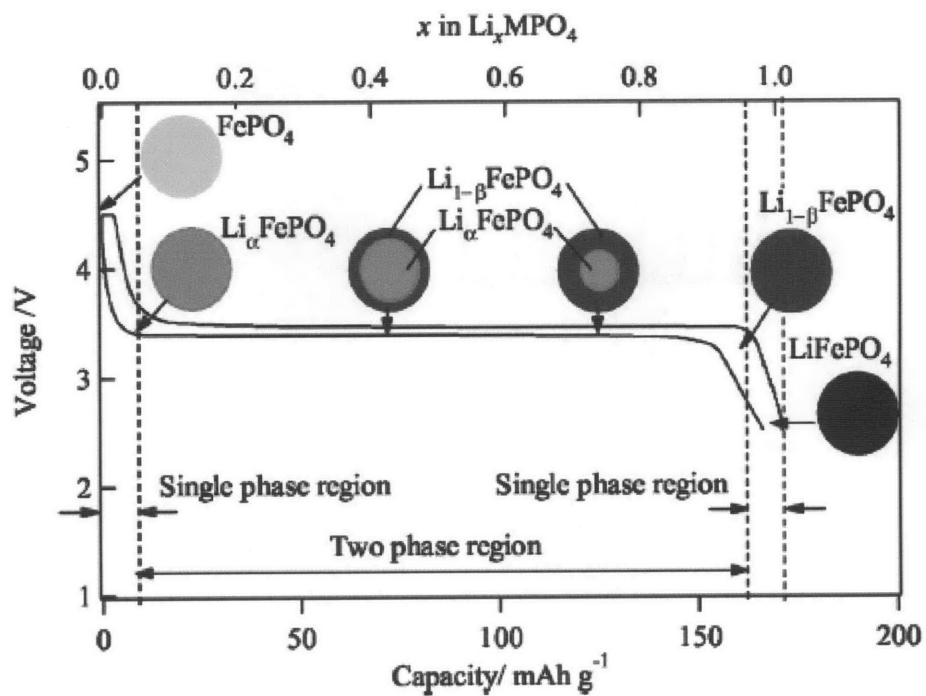
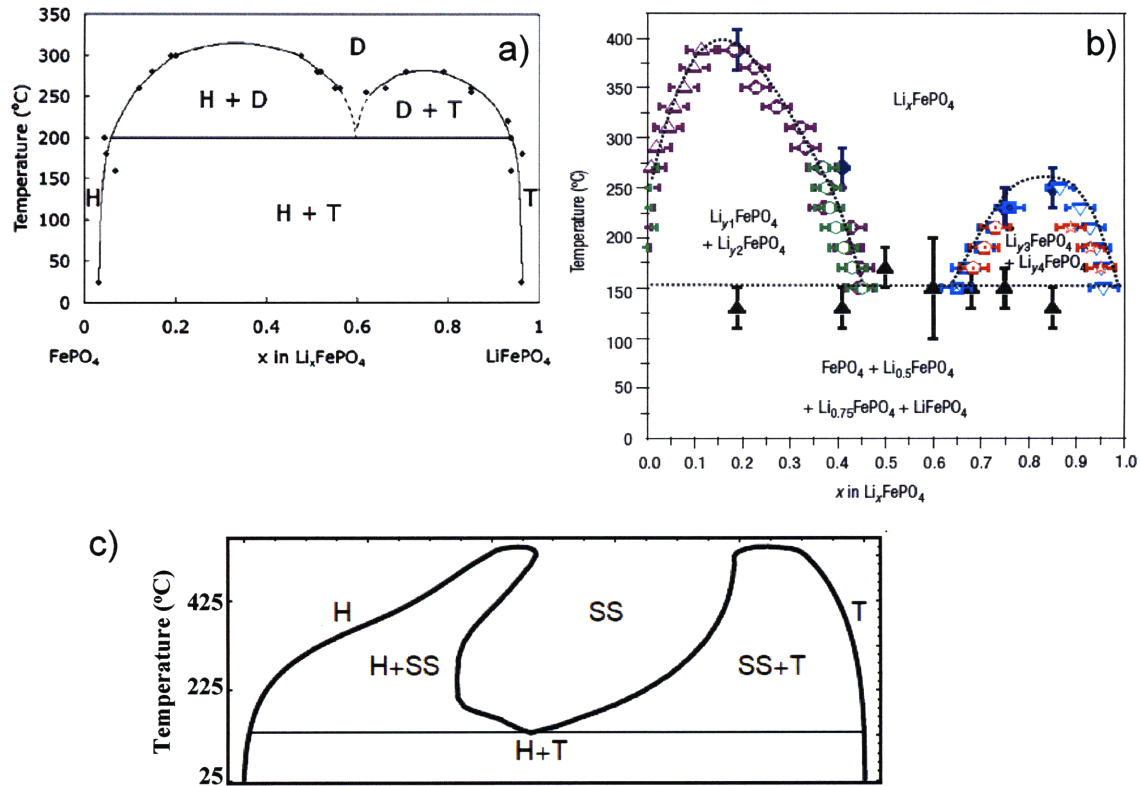


Figure 2-3: Schematic illustration of the “core-shell” model explaining the discharge process of Li<sub>x</sub>FePO<sub>4</sub> proposed by Srinivasan and Newman.<sup>15</sup>



**Figure 2-4: Phase diagram comparison of conventional coarse-grained  $\text{LiFePO}_4$  studied by a) Dodd et al.,<sup>23</sup> b) Delacourt et al.,<sup>22</sup> and c) Zhou et al.,<sup>24</sup> showing existence of miscibility gap in this system. At low temperature, two-phase coexistence of the Li-rich (triphylite or T) and Li-poor (heterosite or H) end-members is observed. At intermediate temperatures, the proposed phase diagram resembles a eutectoid system, with eutectoid point at around  $x = 0.45\text{-}0.65$  and  $150 - 200$  °C. The disordered (D) or solid solution phase (SS) is proposed at high temperatures.**

**Table 2-I: Lattice parameters and unit cell volume for triphylite and heterosite phases as determined by Rietveld refinement, by Andersson et al.<sup>16</sup>**

Lattice constant	Triphylite ( $\text{LiFePO}_4$ )	Heterosite ( $\text{FePO}_4$ )
a (Å)	10.329	9.814
b (Å)	6.007	5.789
c (Å)	4.691	4.782
Volume (Å <sup>3</sup> )	291.1	271.7

# Chapter 3

## Size-Dependent Phase Diagram of $\text{Li}_{1-x}\text{FePO}_4$

In this chapter, the size-dependence of the miscibility gap in undoped  $\text{Li}_{1-x}\text{FePO}_4$  was measured over the temperature range  $-20^\circ\text{C}$  to  $+45^\circ\text{C}$ , using nanoscale powders of varying particle diameters. Samples A and B are powders with average particle diameter of 34 and 42 nm, respectively. Sample C is a commercially available “carbon-added”  $\text{LiFePO}_4$  powder with an average particle diameter of 112nm. Electrochemical and X-ray diffraction techniques were used. A new PITT technique for measuring solid-solution limits in phase-transforming systems without the application of overpotentials was demonstrated. The miscibility gap contracts systematically (increased solid solution limits) with decreasing particle size and increasing temperature, reaching a minimum measured width in this work of  $\sim 20\%$  lithium deficiency and  $\sim 20\%$  lithium excess in triphylite and heterosite, respectively, at 34nm and  $45^\circ\text{C}$ . These effects suggest that the miscibility gap completely disappears below a critical size even near room temperature. The implications of increased miscibility on transport properties and the electrochemically-driven first-order phase transition are discussed.

---

Reprinted in part with permission from *Electrochem. Solid State Lett.*, **10**, A134 (2007).

Copyright 2007, The Electrochemical Society.

## Introduction

Nanoscale powders have been used in materials technology since long before the systematization of nanoscale phenomenon that began in the 1980s. In describing the uniqueness of nanoscale materials, it is useful to distinguish between those variations in properties that are predictable from known size-scaling laws and unexpected behavior arising at nanoscale dimensions.<sup>1</sup> In this respect, the marked increase in rate capability of doped nanoscale lithium-iron phosphate reported by Chung et al.,<sup>2</sup> e.g., > 110 mAh/g specific capacities at 20C discharge rates at room temperature, which was followed by several reports of improved rate capability in nominally “undoped” but nanoscale olivines,<sup>3-5</sup> has raised the question: are there fundamental changes in physical properties of these materials in the nanoscale regime? Some have suggested that the improved properties can be completely explained by the size scaling expected from conventional Fickian transport.<sup>6</sup> However, as we will show in Chapter 4, the doped nanoscale lithium-iron phosphates studied by Chung et al.<sup>2</sup> exhibit, at room temperature, nearly ten times the lithium nonstoichiometry<sup>7</sup> of conventional coarse-grained  $\text{LiFePO}_4$ .<sup>8-10</sup>

In the present work, we conducted a systematic study of the size and temperature dependence of the miscibility gap in nominally undoped  $\text{LiFePO}_4$ . While the extent of solid solution at the equivalent particle size is about a factor of two less than that reported in Ref. 7, a clear and systematic increase in solid-solution nonstoichiometry with decreasing size and increasing temperature is observed.

## Experimental Section

### Test Materials

We performed comparative electrochemical tests and X-ray structural analysis of lithium-iron phosphate powders of three characteristic sizes. Figure 3-1 shows the process flow chart for these powders. The powders were synthesized using lithium carbonate  $\text{Li}_2\text{CO}_3$  (99.999%, Alfa-Aesar, Ward Hill, Massachusetts, USA), iron (II) oxalate  $\text{FeC}_2\text{O}_4 \cdot 2\text{H}_2\text{O}$  (99.99%, Aldrich, Milwaukee, Wisconsin, USA), and ammonium phosphate  $\text{NH}_4\text{H}_2\text{PO}_4$  (99.998%, Alfa-Aesar, Ward Hill, Massachusetts, USA) as the source of the main

components. The starting materials were mixed by ball-milling for 24 hours using zirconia milling media, in acetone, followed by drying, then grinding with a mortar and pestle in an Argon filled glove box before calcining at 350 °C for 10 hours in flowing Argon. Heat treatment to final firing temperatures of 600 and 700°C resulted in powders (samples A and B, respectively) having specific surface areas as measured by the Brunauer, Emmett, and Teller (BET) method of 48.8 and 39.8 m<sup>2</sup>/g, respectively, corresponding to equivalent spherical particle diameters of 42 and 34 nm. These powders had a fairly narrow particle size distribution, as shown in Figure 3-2. The difference in average particle size between samples A and B is difficult to resolve in a small sampling of particles by transmission electron microscopy (TEM). However, both the absolute values and relative differences between these samples indicated by the specific surface area are consistent with the values obtained by Rietveld refinement, discussed later. Both are significantly finer in size than sample C, a commercially available “carbon-added” LiFePO<sub>4</sub> (Aldrich Chemical) having 14.8 m<sup>2</sup>/g specific surface area and 113 nm equivalent spherical particle diameter. This material also had a broader particle size distribution than the other two, and the added carbon material could be clearly seen, Figure 3-2. Samples A and B showed no signs of a discrete carbon phase.

### **Electrochemical Tests**

Electrochemical tests were performed using electrodes formulated with 79 wt % positive active material, 10 wt % conductive carbon black (Super P), M.M.M. Carbon, Brussels, Belgium), and 11 wt % Kynar 2801 binder, using acetone as the solvent. The formulation was coated onto aluminum foil current collectors at a loading of ~5 mg/cm<sup>2</sup> of active material and assembled in Swagelok type or coin cells using Li metal foil as the counter electrode, a microporous polymer (Celgard 2400, Hoechst Celanese Corporation, Charlotte, NC, USA) or glass fiber separator, and liquid electrolyte mixtures containing 1:1 by weight ethylene carbonate/dimethyl carbonate (EC/DMC) or EC/diethyl carbonate (DEC) and 1 M LiPF<sub>6</sub> as the conductive salt. Arbin or Maccor instrumentation was used for the galvanostatic and potentiostatic tests.

## **Structural Analysis**

For X-ray diffraction structural analysis, fresh Swagelok cells were taken to 50% state-of-charge (SOC) and disassembled. About 0.5 mg Si powder (Alfa Aesar, USA) was embedded in the top surface of the electrodes as a standard. X-ray patterns were obtained using a Rigaku RTP500RC instrument with a rotating anode and Cu  $K_{\alpha}$  radiation and were slow-scanned at  $0.15^{\circ}/\text{min}$  over a  $2\theta$  range from 15 to  $135^{\circ}$ . The structural parameters were refined by Rietveld analysis using PANalytical X'Pert HighScore Plus software. The refinements gave the lattice parameters, crystallite size, and residual strain of each sample in Table 3-I.

## **Results and Discussion**

### **Low-Rate Galvanostatic Tests**

Room-temperature galvanostatic charging and discharging measurements performed at C/50 rate on each of the samples are shown in Figure 3-3. (Note that charge/discharge rates are usually reported in C-rate convention, or C/n, where n is the time in hours for complete charge or discharge of the nominal capacity measured. In this case, C/50 rate means that it takes 50 hours to completely charge the cell to the cut-off voltage). Similar results were seen at a still lower current rate of C/100 (not shown). The voltage-capacity curves show significant deviations from the two-phase plateau voltage at the beginning of charge and discharge, respectively. The capacity at which the plateau voltage is reached upon charge or discharge increases as the particle size decreases, suggesting miscibility gap that shrinks systematically with decreasing particle size. Upon charge, the coarsest sample, C, also shows a peak in voltage at the onset of the two-phase plateau that is absent for the other two samples. This feature has been associated with an elastic energy barrier to transformation.<sup>7</sup> With decreasing particle size, the two-phase plateau voltage also increases in small but measurable increments of a few millivolts. Similar changes were observed in the open-circuit voltage (OCV) measurements, discussed later.

## Potentiostatic Intermittent Titration Tests (PITT)

Although the polarization of the cells in galvanostatic measurements was small, suggesting that the observed voltages are close to equilibrium values, sloping voltage curves at low and high states of charge are nonetheless commonly seen as a result of kinetic limitations in electrochemical cells. We sought a measurement that could provide definitive measurements of the extent of equilibrium nonstoichiometry. Galvanostatic intermittent titration tests (GITT), in which voltage relaxation after the application of current pulses is measured, is often used to establish the thermodynamic voltage as a function of composition. However, in systems having a first-order phase transition, such as the present one, the current pulsing needed in GITT inherently leads to an increase in overpotential, which could introduce hysteresis effects due to the nucleation or growth of a new phase. Although GITT measurements generally gave results consistent with those presented here, we consider the following potentiostatic intermittent titration tests (PITT) measurements to be more exacting because they measure the extent of nonstoichiometry without any overpotential, as is now explained. We use  $x$  to denote lithium deficiency in the lithium-rich triphylite endmember (e.g.,  $\text{Li}_{1-x}\text{FePO}_4$ ) and  $y$  to denote lithium excess in the lithium-poor heterosite endmember (e.g.,  $\text{Li}_y\text{FePO}_4$ ). To measure  $x$  and  $y$ , the capacity was measured at small constant-voltage increments progressing through the OCV of the cell (Figure 3-4). The results are plotted in Figure 3-4 in a manner resembling cyclic voltammograms (CVs), except that the vertical axis is capacity and not current. First, the open-circuit potential of each cell at 50 mol % lithiation well within the two-phase field was measured to  $\pm 2$  mV precision. Then, PITT measurements were taken in which, starting from a fully discharged state (discharged to 2.0 V), the voltage was increased in 5 mV increments and the capacity available at each constant-voltage step measured until the current dropped to a  $C/50$  rate. Thus, the capacity available at finely resolved voltage steps with respect to the equilibrium two-phase potential was measured. To determine the lithium deficiency of the triphylite phase,  $x$  in  $\text{Li}_{1-x}\text{FePO}_4$ , the cumulative capacity up to 5 mV below the OCV was measured. Parameter  $x$  was taken to be the fraction of the total charge capacity represented by this capacity. Similarly, to measure the solid-solution lithium concentration in the heterosite phase,  $y$  in  $\text{Li}_y\text{FePO}_4$ ,

the cell was taken to a fully charged state (3.8 V), then discharged at 5 mV voltage decrements, with the current being measured at each voltage step. The value of  $y$  was taken to be the cumulative capacity measured to within 5 mV above the OCV, relative to the total discharge capacity. Because only data obtained below the OCV during charging is used to determine  $x$ , and above the OCV during discharging to determine  $y$ , it is assured that the nonstoichiometry is measured in the absence of any electrochemical driving force for the phase transformation. In galvanostatic or GITT measurements, even at  $C/50$  or slower current rates, polarization resulting in an applied potential above the OCV, corresponding to two-phase coexistence, is possible. Thus, the charge capacity accumulated below the OCV can be attributed to the formation of a lithium-deficient triphylite solid solution prior to the nucleation of heterosite. Similarly, upon discharge, the discharge capacity accumulated above the OCV voltage can be attributed to the formation of a lithium-excess heterosite solid solution prior to the nucleation of triphylite. These procedures should estimate the true extent of solid solution, because even with an applied voltage exactly equal to the OCV, nucleation of the new phase should be difficult. Figure 3-4a shows the PITT results measured at three temperatures for sample A having the smallest average particle size, and Figure 3-4b shows the results for sample C having the largest average particle size. The OCVs measured for each sample at each temperature are also given. The insets show the detail in the vicinity of the OCVs on an expanded scale. Perhaps the most prominent feature of these capacity spectra is the peaks of high capacity. The highest capacity peak in each measurement occurs at an overpotential corresponding to the maximum amount of phase transformation, and the kinetics can be examined in detail to understand the rate capability of each sample.<sup>7</sup> It is seen that with decreasing temperature a greater overpotential is necessary to propagate the first-order phase transformation. However, these peaks are not a direct measure of the nonstoichiometry. Focusing on the capacity in the region near the OCVs of each sample, it can be seen that for sample A, at both 23 and 45°C there is a continuous distribution of capacities over the voltage range near the OCV upon both charging and discharging (Fig. 3-4a). From the capacity distribution, the equilibrium nonstoichiometry is obtained as described above. By comparison, sample C having the largest particle size (Fig. 3-4b) clearly shows less capacity distributed near the OCV. Results for sample B are not



plotted but were similar to those in sample A. The phase diagram for nanoscale lithium-iron phosphate, obtained from the PITT measurements of all three samples at all four test temperatures, is shown in Figure 3-5. It is clearly seen that the two-phase field shrinks with decreasing particle size and that for each particle size, the miscibility gap shrinks with increasing temperature. At 45°C, the 34 nm particle size sample (A) exhibits a maximum solid solution in both endmembers of approximately 20%. Projecting these data to higher temperatures, it appears that the extent of nonstoichiometry in the heterosite phase ( $\text{Li}_y\text{FePO}_4$ ) increases at a higher rate than that in the triphylite phase ( $\text{Li}_{1-x}\text{FePO}_4$ ). We attempted to resolve the phase diagram at temperatures above 45°C but were not able to obtain reliable data due to noticeable self-discharge in the electrochemical cells used in this study. Up to 45°C, repeat PITT measurements yielded closely agreeing results as long as self-discharge was not evident. In fact, in Figure 3-5, the data points shown for sample C at 45°C are actually three overlapping measurements. For samples A and B, the 45°C measurements of  $x$  include duplicate measurements as well. Figure 3-6 shows the results plotted against the equilibrium phase diagram of Dodd et al.<sup>10</sup>

Although there may be practical limits to the particle sizes that can be used in real applications, it is interesting to speculate whether there exists a size below which a complete solid solution may be obtained near room temperature in this system. Figure 3-7 plots the particle size dependence of lithium nonstoichiometry for three test temperatures. The dashed curves are hand-drawn extrapolations through the data at 23°C which while highly approximate, intersect at a finite particle size. Thus, we suggest that a complete solid solution is achievable below about 15 nm particle sizes at room temperature; at 45°C, the data suggest a larger critical size of ~ 25 nm.

### **Diffraction Studies of Size-Dependent Miscibility at Room Temperature**

As an independent measurement of the limits of solid solution for comparison with the electrochemical tests, we carried out X-ray diffraction measurements of the lattice parameters of samples that were electrochemically cycled to 50% SOC at room temperature. Rietveld refinement provided lattice parameters for the coexisting triphylite

and heterosite phases, as well as the crystallite strain and crystallite size of each phase. Whereas the PITT measurements approach the solid-solution limits (Figure 3-5) from compositions outside the miscibility gap, the X-ray diffraction experiment approaches equilibrium from compositions within the gap, where the phases coexist. Because diffraction measures the volume-averaged properties of the sample, those results also allow us to determine whether the size-dependent nonstoichiometry is a surface or bulk effect. It is possible that in a high-surface-area powder, excess nonstoichiometry arises from surface sites differing in Li chemical potential from bulk intercalation sites or from space-charge surface layers<sup>12</sup> penetrating into the crystal, although the high defect concentration of the present materials implies a very compact (sub-nanometer) space-charge width. Figure 3-8 shows the X-ray diffraction patterns collected at room temperature for each sample. The corresponding lattice parameters and unit cell volumes are given in Table 3-I. The crystallite sizes obtained from Rietveld refinement are also shown and are in good agreement with the BET-derived results. Applying Vegard's law to the unit cell volumes and using results from Ref. 8 as the values for the completely stoichiometric endmembers, the values of  $(1 - x)$  and  $y$  in Table 3-II were obtained. As with the galvanostatic and PITT data, the extent of solid solution obtained from Vegard's law increases monotonically with decreasing particle size. Comparing in detail with the PITT-derived values of  $(1 - x)$  and  $y$ , for sample C the values obtained by the two techniques are within 1% of each other. However, for samples A and B, with one exception ( $y$  in sample B), the Vegard's law values are smaller than those obtained by PITT. Yamada et al.<sup>13</sup> also have found, in a sample of unspecified particle size, that values of  $x$  and  $y$  obtained from lattice parameters assuming Vegard's law are smaller than those obtained from galvanostatic titration and neutron diffraction-determined site occupancies. At 25°C, galvanostatic titration yielded values of  $(1 - x) = 0.89$  and  $y = 0.05$ , suggesting that their sample is in between samples C and B in average particle size. Yamada et al.<sup>13</sup> have also recently reported Vegard's law results showing an increase in the  $x$  value at room temperature from 0.02 in a sample of 280 nm particle size to 0.09 in a 88 nm particle size, which is greater than the present Vegard's law results but in reasonable agreement with the PITT derived values.

Another important structural feature that is available from the Rietveld refinement is the strain within each phase. For these samples analyzed at 50% SOC, Figure 3-7 shows that A and B have a much greater retained strain than does C. Notice that the largest strain (sample A) occurs in the sample with the smallest misfit in lattice parameters and unit cell volume between the triphylite and heterosite phases. In contrast, sample C has the largest lattice misfit between phases and the least retained strain. One possible explanation is that coherency stresses arise when the misfit between triphylite and heterosite phases in a partially transformed particles is small enough to retain a coherent interface.<sup>7</sup> As the misfit increases, as in sample C, incoherent interfaces are created that relieve the strains. As discussed below, both coherency stresses and the Gibbs-Thomson effect may make important contributions to the free energy and phase equilibria.

### **Origin of Size-Dependent Nonstoichiometry**

Decreases of miscibility-gap widths in Figure 3-6 appear at about 100 nm particle diameter, and this size-correlated enhanced solubility continues to increase with decreasing mean particle size. These changes in miscibility gap stem from particle-size-associated modifications to the molar free energy of mixing for one or both phases. We suggest the possibility of at least two different origins for these particle size effects: (i) increases due the relative contribution of particle-matrix surface energy and surface stress, and (ii) coherency or compatibility stresses in two-phase particles with a coherent interface. First considering the energy contributions from particle-surface area  $A$ , assuming a surface energy of  $\gamma \approx 1 \text{ J/m}^2$ , typical for inorganic solids, the excess surface energy,  $\gamma A$  for particles of the sizes studied here (3 kJ/mole for 100 nm particles) are several times larger than the heat of demixing in  $\text{Li}_{1-x}\text{FePO}_4$ , measured by Dodd et al. to be 500–700 J/mole.<sup>10</sup> At small particle sizes,  $\gamma A$  may therefore be a significant contribution to a phase's molar free energy of mixing. Similarly, the effect of surface tension also produces an additional pressure,  $P$ , within each particle. The contributions of  $\gamma A$  and  $P\Delta V$  are not independent. However, the molar free energies of both phases should be increased by similar amounts because the two phases have similar densities, surface tensions, and compressibilities. The common tangent and tangency points would translate to higher energies, but effects on the miscibility gap will depend only on small

differences between composition-dependent densities, surface tensions, and compressibilities. The considerations of Gibbs-Thomson on the increased chemical potential of a soluble component as a function of particle size apply whether the particles are of the same phase or not.<sup>15</sup> However, the present case concerns the mutual solubility of two phases of the same particle size in the same medium rather than the relative solubility of a single phase with different particle sizes in the same medium. Coherency stresses can, however, result in a contraction of the miscibility gap with decreasing particle size.<sup>15</sup> Rietveld analyses of the X-ray diffraction data indicates that the distribution of strain increases with decreasing particle size. To test the hypothesis that coherency stresses contribute to the increased strain distribution, we consider a model where the coherent interface lies within an isolated two-phase particle. This coherent interface could be produced by nucleation of a second phase (triphylite or heterosite) in a formerly single phase (triphylite or heterosite) particle. In either coherent interface case, the triphylite phase is under compressive stress because of its higher molar volume, and the heterosite phase is under tensile stress. Due to the positive partial molar volume of lithium in both phases (as opposed to  $\text{LiCoO}_2$ , for example, in which the lattice expands upon initial extraction of Li), the compressive stress in triphylite should decrease its Li solubility relative to tensile-stressed heterosite. Thus, the scaling of coherency stresses in the present samples is qualitatively consistent with the variation in lithium miscibility. Detailed quantitative analyses will appear elsewhere. While this interpretation is consistent with the experimental results, there may well be other contributions to the free energy occurring at nanoscale sizes that should be taken into account, including antisite disorder or other lattice defects. And, there is some possibility that differences exist in the two types of samples due to their different synthesis methods. Furthermore, a distribution of particle sizes may cause Gibbs-Thomson influenced variations in lithium miscibility. In other crystalline systems, it has been known that coherency between coexisting phases produces changes in phase equilibria very much analogous to those observed here.<sup>15-17</sup> The data for present materials suggests that retained coherency is promoted with decreasing particle size at nanoscale dimensions. We will consider phenomenon further within the context of nucleation models that take into account the contribution of elastic energy to phase transformation.

## Summary and Conclusions

The effect of particle size in a series of undoped samples ranging in size from 113 to 34 nm and temperatures from -20 to 45 °C on phase diagram of LiFePO<sub>4</sub> has been studied using x-ray diffraction and potentiostatic titration tests. We found dramatic changes in the miscibility gap compared to previous published phase diagram in which the miscibility gap in undoped nanoscale Li<sub>1-x</sub>FePO<sub>4</sub> powders contracts with decreasing particle size and increasing temperature. We predict that below ~15 nm, a complete solid solution can be obtained at room temperature. The implications of increased miscibility on transport properties and the electrochemically-driven first-order phase transition as well as the thermodynamics illustration of how elastic stresses should be incorporated in thermodynamic treatments of electrochemistry are discussed.

## References

1. Y.-M. Chiang, *J. Electroceram.*, **1**, 205 (1997).
2. S. Y. Chung, J. T. Bloking, and Y.-M. Chiang, *Nat. Mater.*, **1**, 123 (2002); S. Y. Chung, J. T. Bloking, and Y. M. Chiang, *Nat. Mater.*, **2**, 702 (2003).
3. E. M. Bauer, C. Bellitto, M. Pasquali, P. P. Prosini, and G. Righini, *Electrochem. Solid-State Lett.*, **7**, A85 (2004).
4. N. H. Kwon, T. Drezen, I. Exnar, I. Teerlinck, M. Isono, and M. Graetzel, *Electrochem. Solid-State Lett.*, **9**, A277 (2006).
5. C. Delacourt, P. Poizot, S. Levasseur, and C. Masquelier, *Electrochem. Solid-State Lett.*, **9**, A352 (2006).
6. K. Striebel, J. Shim, V. Srinivasan, and J. Newman, *J. Electrochem. Soc.*, **152**, A664 (2005).
7. N. Meethong, H.-Y. S. Huang, S. A. Speakman, W. C. Carter, and Y.-M. Chiang, *Adv. Funct. Mater.*, **17**, 1115 (2007); Y.-M. Chiang, N. Meethong, S. Chang, H.-Y. S. Huang, W. C. Carter, A. S. Gozdz, and A. Shiao, The Electrochemical Society Meeting Abstracts, Vol. MA2006-02, Cancun, Mexico, Oct 29–Nov 3, 2006.

8. A. Yamada, H. Koizumi, N. Sonoyama, and R. Kanno, *Electrochem. Solid-State Lett.*, **8**, A409 (2005).
9. C. Delacourt, P. Poizot, J.-M. Tarascon, and C. Masquelier, *Nat. Mater.*, **4**, 254 (2005).
10. J. L. Dodd, R. Yazami, and R. B. Fultz, *Electrochem. Solid-State Lett.*, **9**, A151 (2006).
11. P. Gibot et al., *Nat. Mater.*, **7**, 741 (2008).
12. See, for example, Y.-M. Chiang, A. F. Henriksen, W. D. Kingery, and D. Finello, *J. Am. Ceram. Soc.*, **64**, 383 (1981); J. A. S. Ikeda and Y.-M. Chiang, *J. Am. Ceram. Soc.*, **76**, 2437 (1993); J. A. S. Ikeda, Y.-M. Chiang, A. J. Garratt-Reed, and J. B. Vander Sande, *J. Am. Ceram. Soc.*, **76**, 2447 (1993).
13. A. Yamada, Y. Takei, H. Koizumi, N. Sonoyama, R. Kanno, K. Ito, M. Yonemura, and T. Kamiyama, *Nat. Mater.*, **5**, 357 (2006).
14. A. Yamada, Abstract, 360, IMLB 2006, June 18–23, 2006, Biarritz, France.
15. R. W. Balluffi, S. M. Allen, and W. C. Carter, *Kinetics of Materials*, pp. 445–448, Wiley and Sons, 2005.
16. J. W. Cahn and F. Larché, *Acta Metall.*, **32**, 1915 (1984).
17. R. O. Williams, CALPHAD: Comput. Coupling Phase Diagrams Thermochem., **8** (1), 1 (1984).

## Chapter 3 Figures and Tables

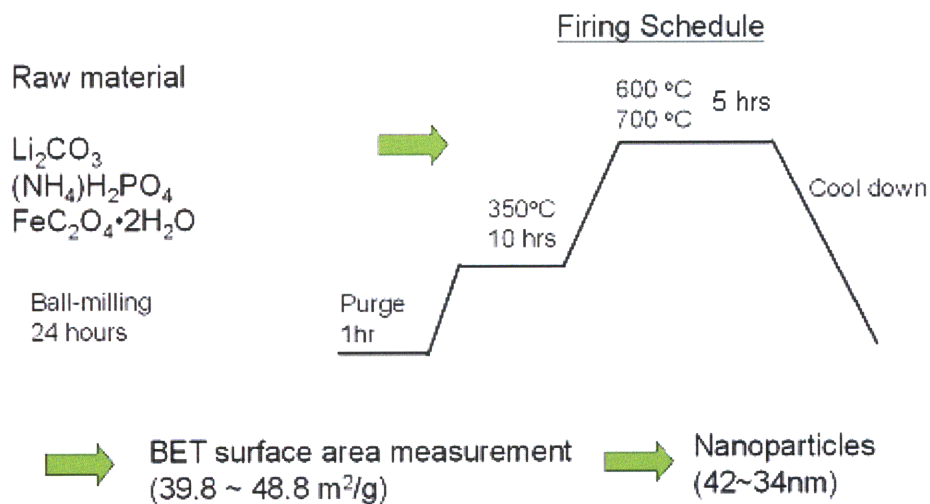


Figure 3-1: Sample preparation and firing schedule for the studied powders.

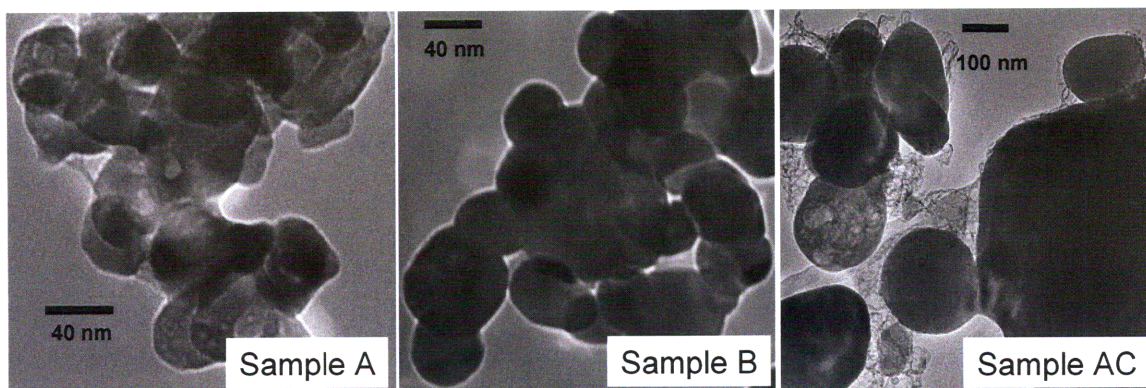
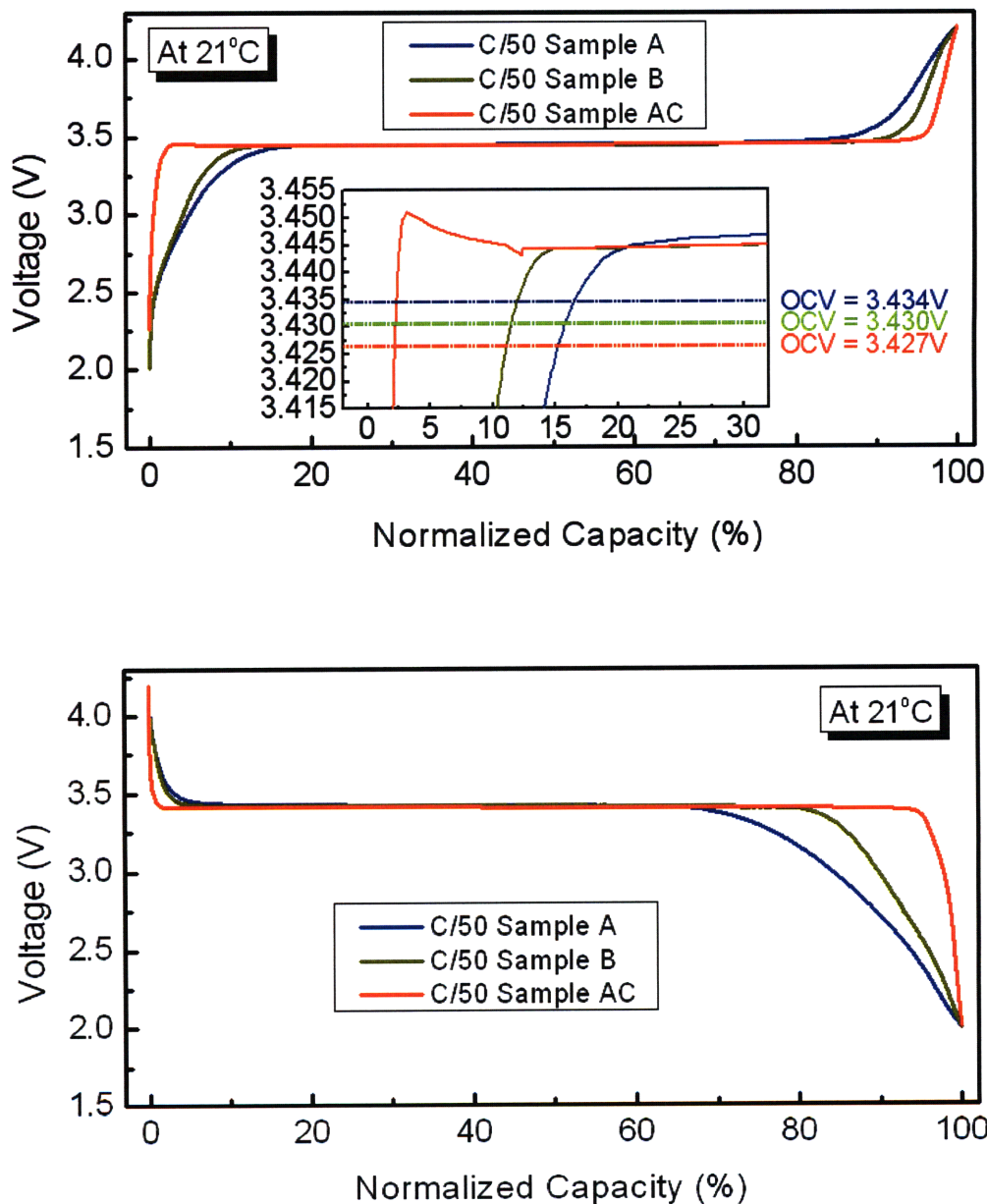
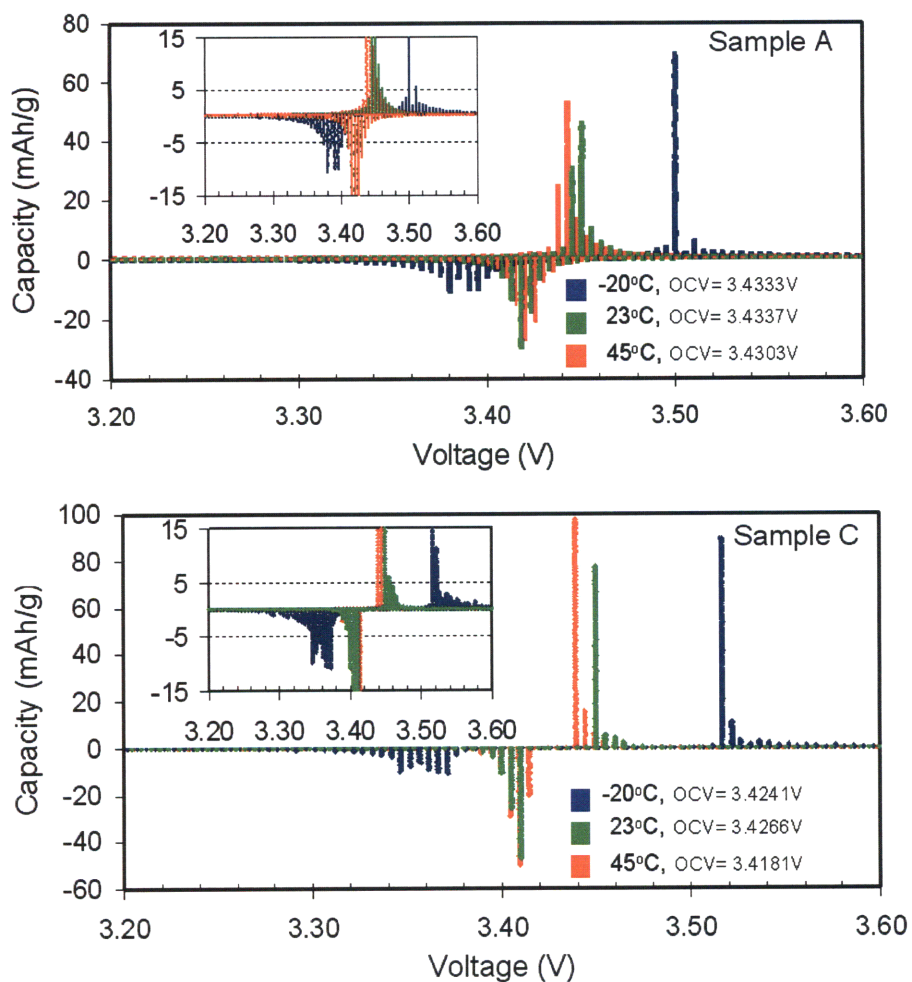


Figure 3-2: Transmission electron microscopy (TEM) images of three powder samples tested, having the following BET specific surface areas and equivalent spherical particle diameters. (A) 48.8 m<sup>2</sup>/g, 34 nm; (B) 39.8 m<sup>2</sup>/g, 42 nm; (C) 14.8 m<sup>2</sup>/g, 113 nm. Sample C is a “carbon added” commercial sample in which fibrillar carbon can be seen, in contrast to samples A and B which have no detectable carbon phase.



**Figure 3-3:** Galvanostatic charging (top) and discharging (bottom) at C/50 rate shows the narrower composition range over which smaller size particles exhibit a constant cell voltage corresponding to two-phase coexistence. Note also the overpotential measured on charge for the coarsest sample C as the two-phase plateau voltage is approached, absent for finer particle size samples A and B (inset). The two-phase plateau voltage also differs measurably for the three samples.





**Figure 3-4:** Lithium solubility in the triphylite and heterosite phases is determined from the capacity vs. voltage measured potentiostatically upon charge and discharge in 5 mV steps. The OCV measured by taking each cell to 50% SOC and allowing voltage relaxation is indicated for each sample. Sample A has average particle diameter of 34 nm while sample C average particle diameter of 113 nm.

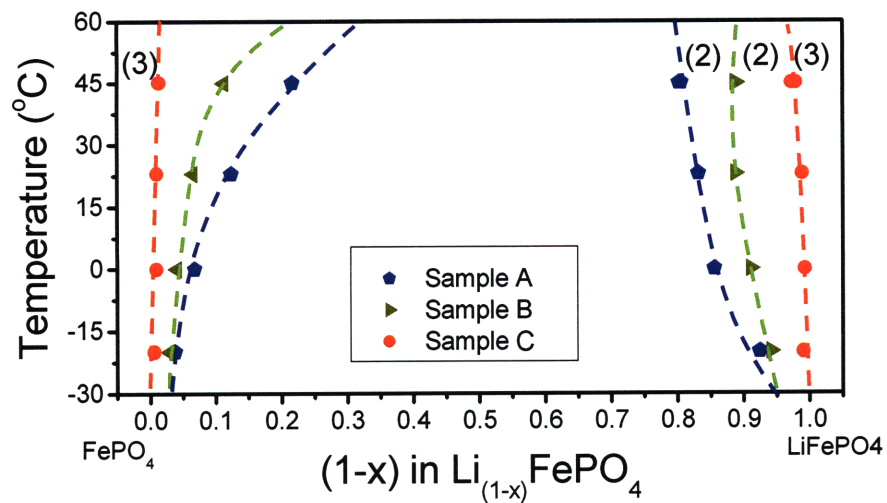


Figure 3-5: Phase diagram for nanoscale lithium iron phosphate showing that the miscibility gap contracts systematically (increased solid solution limits) with decreasing particle size and increasing temperature. Numbers in parenthesis indicate the number of data points taken at that temperature to ensure consistency of the results.

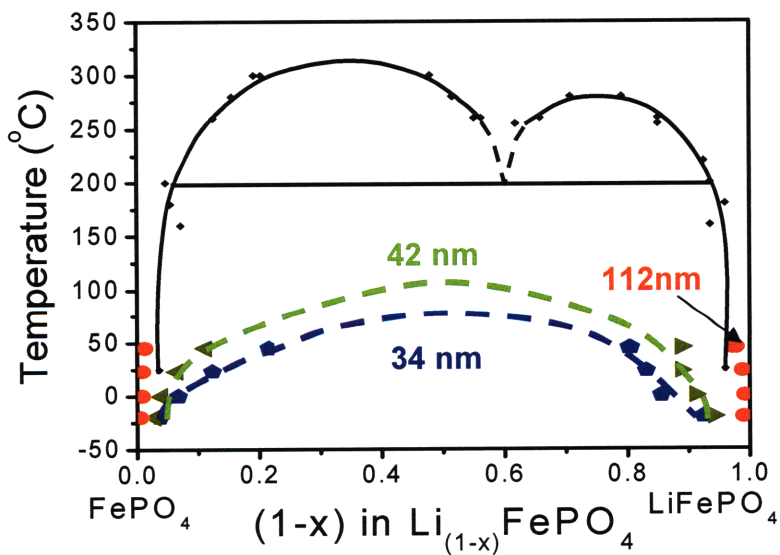


Figure 3-6: Phase diagram for nanoscale lithium iron phosphate plotted against the equilibrium phase diagram of Dodd et al.<sup>10</sup>

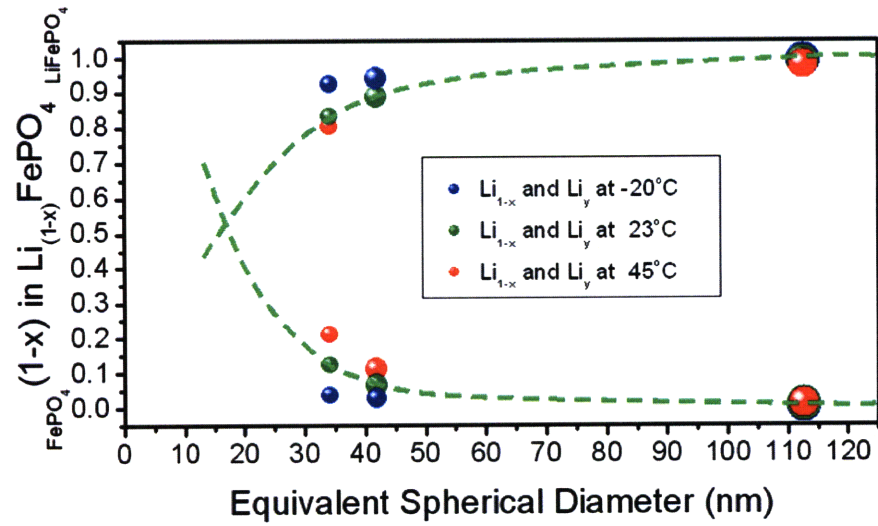
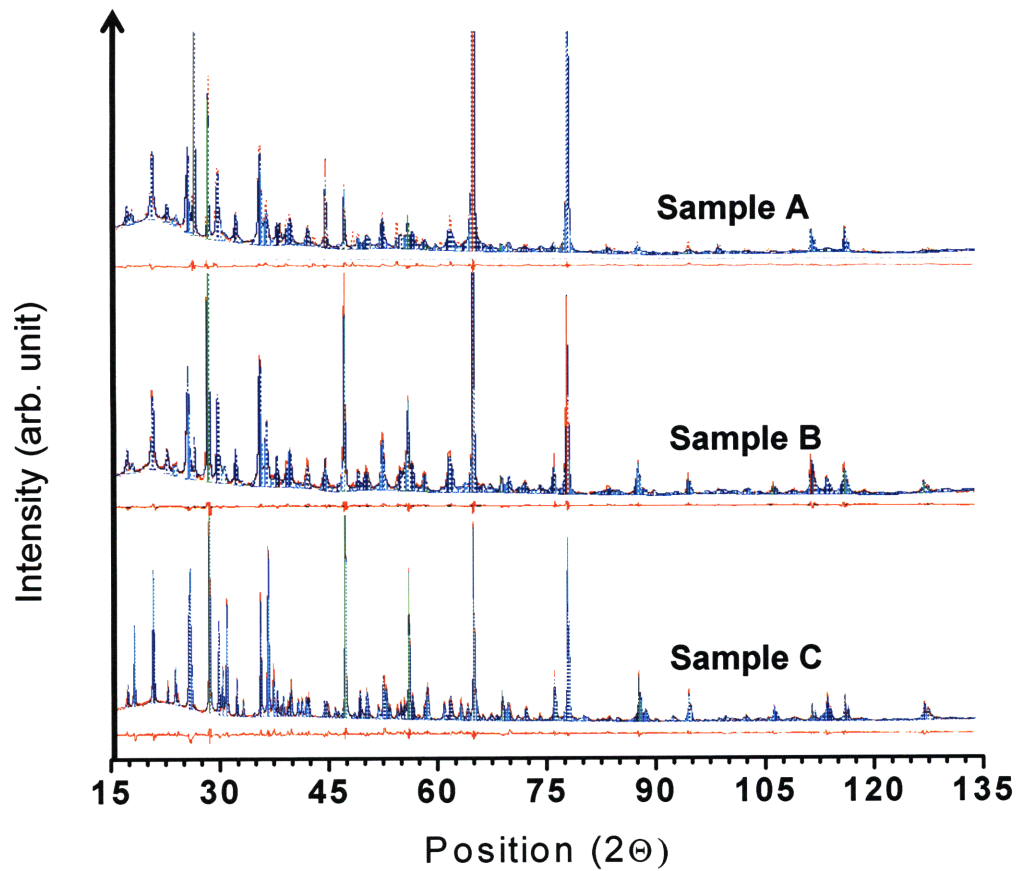


Figure 3-7: Lithium nonstoichiometry as a function of equivalent spherical diameter plot shows that below ~15 nm particle diameter, the miscibility gap may disappear completely at room temperature.



**Figure 3-8: Rietveld refined X-ray patterns for samples A, B, and C respectively, taken on samples at ~ 50% state of charge, including the fit to Si powder added as an internal standard. The observed intensity data are shown by the solid red line, and the dashed blue, aqua, and green lines overlying them are the calculated intensity of  $\text{LiFePO}_4$ ,  $\text{FePO}_4$ , and Si respectively. The difference between the observed and calculated intensities is shown for each of the patterns.**

**Table 3-I: The corresponding structural parameters obtained from the refinements of X-ray diffraction spectra (Figure 3-8).**

<b>Composition-state</b>	<b>Sample A</b>	<b>Sample B</b>	<b>Sample AC</b>
	<b>~50% SOC</b>	<b>~50% SOC</b>	<b>~50%SOC</b>
Specific Surface Area (m <sup>2</sup> /g)	48.8	39.8	14.8
Carbon content (wt%)	3.48	2.27	1-3
R <sub>expected</sub> (%)	6.956	6.596	5.794
R <sub>weighted profile</sub> (%)	7.199	10.422	10.711
<b>LiFePO<sub>4</sub> phase</b>			
a (angstroms)	10.266(1)	10.3079(7)	10.3289(3)
b (angstroms)	5.9789(6)	5.9973(4)	6.0069(2)
c (angstroms)	4.7060(5)	4.6999(4)	4.6905(2)
V (angstroms <sup>3</sup> )	288.8542	290.533	291.0224
Strain (%)	0.39	0.129	0.02
Crystallite size (Å)	382	386.9	1145.4
<b>FePO<sub>4</sub> phase</b>			
a (angstroms)	9.860(2)	9.854(4)	9.8267(3)
b (angstroms)	5.8291(8)	5.815(2)	5.7944(1)
c (angstroms)	4.774(1)	4.787(3)	4.7832(1)
V (angstroms <sup>3</sup> )	274.3775	274.3125	272.3572
Strain (%)	0.365	0.245	0.05
Crystallite size (Å)	273.1	388.9	799.6

**Table 3-II: Comparison of lithium solid-solution limits obtained from Rietveld refinement of X-ray diffraction spectra (Figure 3-8), assuming Vegard's law, with those obtained by PITT.**

23 °C	Particle Diameter (nm)	1-x (XRD)	y (XRD)	1-x (PITT)	y (PITT)
Sample A	34	0.8811	0.1151	0.8315	0.1236
Sample B	42	0.9608	0.0802	0.8876	0.0656
Sample C	113	0.9738	0.0149	0.9890	0.0100

# Chapter 4

## Phase Behavior of Nanoscale $\text{Li}_{1-x}\text{FePO}_4$ and Criterion for Selecting Materials for High-Power Rechargeable Batteries

High energy lithium-ion batteries have improved performance in a wide variety of mobile electronic devices. A new goal in portable power is the achievement of safe and durable high-power batteries for applications such as power tools and electric vehicles. Towards this end, olivine-based positive electrodes are amongst the most important and technologically enabling materials. While certain lithium metal phosphate olivines have been shown to be promising, not all olivines demonstrate beneficial properties. The mechanisms allowing high power in these compounds have been extensively debated.

In this chapter, we will show that certain high rate capability olivines are distinguished by having extended lithium nonstoichiometry (up to ca. 20 %), with which is correlated a reduced lattice misfit as the material undergoes an electrochemically driven, reversible, first-order phase transformation. The rate capability in several other intercalation oxides can also be correlated with lattice strain, and suggests that nanomechanics plays an important and previously unrecognized role in determining battery performance.

---

Reproduced in part with permission from *Adv. Funct. Mater.*, **17**, 1115 (2007). Copyright 2007, WILEY-VCH Verlag GmbH & Co. KGaA, Weinheim.

## Introduction

Following the first journal publication describing the use of olivine compounds as rechargeable battery electrodes,<sup>1</sup> the potential for reduced cost and improved safety<sup>2</sup> of this class of materials was quickly appreciated, but, because of the lower volumetric energy compared with compounds such as  $\text{LiCoO}_2$  and the poor rate capability, the practical utility was unclear. Interest in high power applications grew rapidly after Chung et al.<sup>3</sup> demonstrated high capacity at charge/discharge rates well above 5 C in doped nanoscale  $\text{LiFePO}_4$  (e.g.,  $115 \text{ mAh g}^{-1}$  for 20 C continuous discharge at room temperature<sup>4</sup>), but it also raised controversy over the origin of the exceptional rate performance.<sup>5-10</sup> The ability to obtain high power while retaining reasonably high energy, along with inherent safety and long cycle life (many thousands of charge/discharge cycles), seems likely to enable many new classes of applications. However, not all olivines have exhibited high rate capability, a notable exception being  $\text{LiMnPO}_4$ , which is otherwise attractive for its higher theoretical energy.<sup>11-13</sup> Numerous studies have attributed the rate capability of olivines purely to chemical diffusion limitations.<sup>1,3,6-8,10-12,14</sup> Indeed, either electronic or ionic conductivity can be rate-limiting under certain conditions. However, noting that this class of olivines undergoes a first-order phase transition upon electrochemical cycling, we reasoned that an equally important goal should be to maximize the rate of phase transformation, regardless of the rate-limiting step. Thus, we considered whether the phase transformation kinetics, which corresponds directly to the rate of lithium exchange, might be affected by other, structural, factors.

## Experimental Section

### Test Materials

We performed comparative electrochemical tests and X-ray structural analysis on two types of lithium iron phosphates. The first was a recently synthesized material, cation-doped  $\text{LiFePO}_4$  prepared for earlier publications,<sup>3,4</sup> denoted NC. Figure 4-1 shows the discharge capacity versus rate behavior for a sample of similar performance to those originally described. For comparison, we used a high-surface-area “carbon-added”

LiFePO<sub>4</sub> (Aldrich Chemical), denoted AC, of similar carbon content to the NC samples (Table 4-I). This material has a higher rate capability than untreated pure LiFePO<sub>4</sub>, but its capacity at rates above 1 C is well below that of the NC sample (Figure 4-1). Identical formulations, active material loadings, and preparation methods were used to prepare samples for electrochemical testing, as described in the Experimental section. It is emphasized that neither material is believed to represent the state-of-the-art capability of any particular manufacturer, and, the samples are not selected for maximum contrast in rate capability, but because all of the experiments discussed herein were performed on them. At the time this study was initiated, sample AC was the only commercially available “battery grade” LiFePO<sub>4</sub>. For NC-type samples, partial data were also available for a number of similar materials and are consistent with the results presented here.

Table 4-I shows the physical and structural characteristics of the two samples along with data for olivines from several literature reports. The NC sample of Li<sub>0.99</sub>Nb<sub>0.01</sub>FePO<sub>4</sub> composition was prepared according to a published procedure,<sup>3</sup> and has a specific surface area of 39.2 m<sup>2</sup> g<sup>-1</sup>, corresponding to an equivalent spherical particle diameter of 43 nm. Sample AC has a specific surface area of 14.8 m<sup>2</sup> g<sup>-1</sup> corresponding to a 113 nm diameter, which is high compared to lithium battery cathodes such as LiCoO<sub>2</sub> and LiMn<sub>2</sub>O<sub>4</sub> (typically < 1 m<sup>2</sup> g<sup>-1</sup>). Although we attempted to increase the particle size of both materials through heat treatment in order to obtain systematic size variations, significant changes were not achieved except under temperatures and gas ambient that also produced detectable amounts (by X-ray) of impurity phases, primarily metal phosphides. Nonetheless, the samples in this study can be compared with those of several previous publications, listed in Table 4-I, all of which are expected to have lower rate performance than either of the two sample types measured here. It should also be noted that in the case of sample NC, a comparative study of the high rate performance of various olivines by Striebel et al.<sup>7</sup> included results for an Massachusetts Institute of Technology (MIT)-supplied electrode that were inferior to those described here and in the original publications,<sup>3,4</sup> namely, only ca. 100 mAh g<sup>-1</sup> at 10 C rate. There may be a simple explanation for this discrepancy—Striebel et al. comment that a large additional impedance was necessary to model the electrode provided,<sup>7</sup> which suggests that



delaminating of the electrode coating from the current collector had occurred. In our measurements, samples of the same type retained up to 85 mAh g<sup>-1</sup> capacity (50% of the theoretical value) at 50 C-rate at room temperature. Applied in larger-scale cells, similar materials used in cylindrical lithium ion cells of 26 mm diameter and 65 mm length provide ca. 3 kWkg<sup>-1</sup> power density and ca. 110 Wh kg<sup>-1</sup> energy density.<sup>15</sup>

### **Electrochemical Tests**

Electrochemical tests were performed on electrodes formulated with 79 wt% positive active material, 10 wt% conductive carbon black (Super P, M.M.M. Carbon, Belgium) and 11 wt% Kynar 2801 binder, using acetone as the solvent. The formulation was coated onto aluminum foil current collectors at a loading of < 5 mg.cm<sup>-2</sup> of active material, and assembled in Swagelok<sup>TM</sup> type or coin cells using Li metal foil as the counter electrode, a microporous polymer (Celgard 2400, Hoechst Celanese Corporation, Charlotte, NC, USA) or glass fiber separator, and liquid electrolyte mixtures containing 1:1 by weight ethylene carbonate: dimethyl carbonate (EC:DMC) or ethylene carbonate: diethyl carbonate (EC:DEC), and 1 M LiPF<sub>6</sub> as the conductive salt. Arbin or Maccor instrumentation was used for the galvanostatic and potentiostatic tests. Charge/discharge rates are reported in the C-rate convention, or *C/n*, where *n* is the time (h) for complete charge or discharge of the nominal capacity measured at low rates. High rate discharge capacities were obtained by first charging at *C/2* rate to 3.8 V and holding until the current decayed to *C/25*, followed by galvanostatic discharge at the desired rate to 2.0 V. For the PITT measurements, the open-circuit potential of each cell at 50 mol% lithiation (well within the two-phase field) was first measured to ±2 mV precision, then 10 mV steps were taken starting from the fully discharged or fully charged state, and the capacity measured at each voltage increment until a *C/50* lower current limit was reached.

### **Structural Analysis**

For X-ray diffraction structural analysis, the Swagelok cells were taken to 50% state of charge, rested for > 24 h, and disassembled. About 0.0005 g Si powder (Alfa Aesar, USA) was embedded in the top surface of the electrodes as a standard. X-ray patterns

were obtained using a Rigaku RTP500RC instrument with a rotating anode and  $\text{CuK}\alpha$  radiation, and were slow scanned at  $0.15^\circ \text{ min}^{-1}$  over a  $2\theta$  range from  $15^\circ$  to  $135^\circ$ . The structural parameters were refined by Rietveld analysis using a PANalytical X'Pert HighScore Plus software. The Rietveld refinements gave the structural parameters in Table 4-I with goodness of fit and weighted residual error parameter (GOF and  $R_{\text{wp}}$ ) values of less than 4.0 and 10.0, respectively, indicating reliable refinements.

### **Thermodynamic Model**

The elastic energy of spherical shell and spherical cap configurations were modeled using Ansys 8.0 software (Ansys Inc., Canonsburg, PA) by Dr. H.Y Huang in Prof. Carter group. A thermal conduction model of the same geometry was constructed first and tested, following which the structural model was constructed by switching to an equivalent structural element. Materials properties and structural symmetry boundary conditions were specified, and the overall elastic energy was calculated for the different geometrical configurations.

## **Results and Discussion**

### **Electrochemical Measurements**

Galvanostatic charging and discharging measurements were first performed using lithium half-cells (Figure 4-2). For each sample, only a small difference in polarization was seen between C/50 and C/100 rate measurements, indicating that kinetic limitations were negligible at these slow rates (Figure 4-2). The voltage–capacity curves show deviations from the two-phase plateau voltage at the beginning and end of charge that suggest a compositionally narrower two-phase field for the NC materials, Figure 4-2. The plateau voltage is slightly higher for the NC sample. This is not due to greater polarization, but instead, due to a difference in the open-circuit voltage (OCV) of about 0.006 V between the two materials (confirmed by repeat measurements), which reflects a thermodynamic difference. Although the polarization of these cells was small, suggesting that the observed voltages are close to equilibrium values, sloping voltage curves at low and high states of charge in galvanostatic measurements are commonly attributed to kinetic

limitations. Therefore, we sought a measurement that could provide definitive measurements of the extent of equilibrium nonstoichiometry. Galvanostatic intermittent titration tests (GITT), in which voltage relaxation after the application of current pulses is measured, is often used to establish the thermodynamic voltage versus composition. However, when a first-order phase transition is present, current pulsing inherently leads to an increase in the overpotential, which could introduce hysteresis effects when nucleation of the new phase or migration of the phase boundary occurs. (GITT was nonetheless performed on some NC samples and gave results consistent with those presented here.)

Instead, a potentiostatic intermittent titration test (PITT) was used in which the capacity was measured at small voltage increments progressing through the open-circuit voltage (OCV) of the cell (Fig. 4-3). After each voltage step, the current decay (to a  $C/50$  rate or less) provided the charge or discharge capacity available at that voltage. The OCV was first measured to  $\pm 2$  mV precision with the cells at 50% lithiation, a composition that is well within the two-phase field. PITT was then conducted starting from the discharged or charged states, approaching the two-phase voltage in 5 or 10 mV steps. By conducting the measurement in this manner, no thermodynamic driving force is applied for the phase transformation during charging until the open-circuit voltage (OCV) corresponding to two-phase coexistence is exceeded. Thus, any charge capacity accumulated below the OCV can be attributed to states available to lithium ions before the new phase is nucleated; that is, it is due to the formation of a lithium-excess solid solution, starting with a delithiated material. Similarly, upon discharge from a higher voltage, there is no driving force for the phase transition until the applied voltage falls below the OCV (we will refer to both instances as the imposition of an “overpotential”). Here, any charge capacity accumulated above the OCV voltage can be attributed to the formation of a lithium excess solid solution in the lithiated starting material. We use  $x$  to denote lithium deficiency in the lithium-rich end-member (e.g.,  $\text{Li}_{1-x}\text{FePO}_4$  and  $\text{Li}_{0.99-x}\text{Nb}_{0.01}\text{FePO}_4$ ) and  $y$  to denote lithium excess in the lithium-poor end-member (e.g.,  $\text{Li}_y\text{FePO}_4$  and  $\text{Li}_y\text{Nb}_{0.01}\text{FePO}_4$ ). The results of the PITT measurements are plotted in Figure 4-3 in a manner resembling cyclic voltammograms (CV) except that the vertical axis is capacity

and not current. Sample NC (Fig. 4-3a) exhibits substantial capacity upon both charging and discharging before the two-phase OCV is reached, while sample AC (Fig. 4-3b) exhibits virtually no capacity upon either charge or discharge until an overpotential of ca. 30 mV is applied. The maximum extent of solid-solution nonstoichiometry,  $x$  and  $y$ , measured with the last voltage increments being within 10 mV of the OCV, is 19.6% and 11.7 %, respectively, for sample NC, and 1.4% and 1.0 %, respectively, for sample AC. Results for sample AC are consistent with previous findings<sup>1,9,16,17</sup> of very limited lithium nonstoichiometry in both end-members near room temperature. A recent neutron diffraction study does suggest somewhat higher stoichiometry than that derived from lattice constants.<sup>18</sup> Chung et al.<sup>3</sup> proposed that the improved properties of their doped nanoscale materials resulted from extended lithium solid solubility not achievable in conventional LiFePO<sub>4</sub>. The present electrochemical measurements as well as the structural data presented below support their original interpretation.<sup>4</sup>

### **Diffraction Studies**

We determined whether the excess nonstoichiometry measured electrochemically is a surface or bulk effect. It is possible that in a high-surface-area powder, excess nonstoichiometry can arise from surface sites differing in Li chemical potential from bulk intercalation sites. Surface chemical activity can also lead to the formation of space charge surface layers<sup>19</sup> penetrating into the crystal, although the high defect concentration of the present materials implies a very compact (sub-nanometer) space charge width. To distinguish nonstoichiometry occurring at the surface alone from that occurring within the volume of the particles, we carried out powder X-ray diffraction on samples that were electrochemically cycled to 50% state-of-charge (SOC). The coexistence of the lithiated and delithiated phases means that each is at its maximum limit of mutual solid solubility (maximum nonstoichiometry) at the test temperature. The electrochemically cycled cells were allowed to rest for more than 24 h before being disassembled and analyzed by X-ray diffraction (Figure 4-4). The X-ray diffraction results showed that the lattice parameters of the coexisting phases vary in accordance with the electrochemically determined nonstoichiometry, indicating that bulk effects must be considered. Rietveld refinement provided lattice parameters for the coexisting lithium- rich and lithium-poor phases, as

well as the crystallite strain and crystallite size of each phase. As shown in Table 4-I, the X-ray crystallite sizes for samples NC and AC are in good agreement with those deduced from their specific surface areas. In each case the delithiated phase has the smaller unit cell volume, with smaller a and b parameters and a larger c parameter. For sample AC, the absolute values of the lattice parameters and the unit cell volume are in good agreement with literature (Table 4-I). However, in sample NC, the unit cell volumes of the lithiated and delithiated phases are lower and higher, respectively, consistent with the lithium nonstoichiometry measured electrochemically. Applying Vegard's law to the unit cell volume and using the lattice constants reported in the literature,<sup>16</sup> the nonstoichiometry in sample NC is  $x = 19.5\%$  and  $y = 16.5\%$ , while the nonstoichiometry in sample AC is nominally zero since the unit cell volumes of the triphylite and heterosite phases are slightly larger and smaller respectively than the literature data, Table 4-I. Extended lithium nonstoichiometry is therefore inferred in the NC samples from three independent tests: low-rate galvanostatic tests (Figure 4-2), PITT tests (Figure 4-3), and lattice parameter measurements (Table 4-I). Note that the galvanostatic and PITT measurements approach the phase boundary from a limiting solid solution that is either fully lithiated or fully delithiated, and thus measures the maximum nonstoichiometry that can be obtained without requiring nucleation of the other phase. In contrast, the structural measurements are performed on samples that approach equilibrium from a two-phase coexistence, namely, from within the two-phase field. The good agreement between these measurements indicates that the nonstoichiometry is a true, equilibrium feature of the phase diagram for the NC samples and that the primary cause of the lattice parameter variations is indeed lithium nonstoichiometry. How the doping combined with nanoscale particle size in the NC samples stabilizes such large nonstoichiometry is not completely clear, but we note that the small heat of demixing in the  $\text{LiFePO}_4/\text{FePO}_4$  system (ca.  $600 \text{ J mol}^{-1}$ )<sup>17</sup> implies sensitivity of the phase stability to small changes in composition and introduced defects. A related study<sup>20</sup> of undoped nanoscale  $\text{LiFePO}_4$  has shown that the miscibility gap shrinks systematically as the particle size decreases, demonstrating clearly the existence of a size-dependent nonstoichiometry. However, at equivalent size (ca. 40 nm) the extent of solid solution is only about one-half of that measured in sample NC. Regardless of the origin, the availability of such large nonstoichiometry within both solid

solution phases, corresponding to coexistence of  $\text{Fe}^{2+}$  and  $\text{Fe}^{3+}$ , suggests that the electronic structure and transport properties will differ from those of the pure end-member phases ( $\text{LiFePO}_4$  and  $\text{FePO}_4$ ) considered in most studies to date.

### **Coupling between Elastic Misfit, Lithium Nonstoichiometry, and Rate Capability**

In correlation with the extended nonstoichiometry (increased mutual solid solubility) is a large decrease in the lattice misfit between the lithiated and delithiated phases. The percentage misfit between the lithiated and delithiated phases for the  $a$ ,  $b$ , and  $c$  parameters, the unit cell volume ( $abc$ ), and the unit cell faces  $ab$ ,  $ac$ , and  $bc$  are given in Table 4-I. There is significantly lower lattice misfit in the high rate NC sample compared to all others. The volume misfit in sample AC is 6.63 %, within the range 6.45–6.87% published for  $\text{LiFePO}_4$ , whereas in sample NC it is reduced by one third to 4.15 %. Even more striking is the difference in misfit between the principal crystal planes. Given the relatively isotropic elastic constants of  $\text{LiFePO}_4$ ,<sup>21</sup> from purely elastic considerations, we expect the interface between coexisting phases to form preferentially on the plane of minimum strain, which is the  $bc$  or  $\{100\}$  plane. Chen et al.<sup>22</sup> have recently observed that cycled  $\text{LiFePO}_4$  cracks along the  $\{100\}$  plane, consistent with this expectation. Equally important, their observations show that the misfit in conventional  $\text{LiFePO}_4$  is large enough, even along the plane of minimum strain, to cause rupture. The fracture plane appears to be dominated by these simple elastic considerations, even though faster lithium diffusion along the  $b$  axis might be expected to produce a preference for growth of the  $ac$  plane ( $\{010\}$  plane). For sample AC as well as the literature data, the strain in this plane is 1.65–1.79 %. By contrast, in the high rate sample NC, the strain is reduced to 0.73 %, which, as we show, should allow the interface to remain coherent and permit facile phase propagation with reduced accumulated elastic or plastic strains. The PITT tests also provided a direct measurement of each sample's transformation rate as a function of overpotential. During two-phase coexistence, and assuming no capacitive current, no short circuits, or other regions of lithium accumulation, the current measured in PITT is exactly linear to the phase transformation rate. The PITT data showed completely different kinetics in the two types of samples (Figure 4-5). Firstly, a smaller overpotential (ca. 15 mV) is required to propagate the first-order phase transition in

sample NC compared with sample AC (ca. 30 mV). The NC sample shows a maximum current at the start of each voltage increment, followed by rapid but monotonic decay. Significantly, sample AC shows a completely different response in which the current is initially low, rising slowly to reach its maximum value ca. 4 h later. This kinetic response clearly cannot be modeled by any “simple” diffusional process, and suggests a phase transformation barrier that is gradually overcome at constant potential as the phase transformation proceeds. Similar results were obtained upon discharge, and after multiple cycles. The amount of retained crystallographic strain in the partially transformed materials further shows that these materials can be distinguished on the basis of elastic misfit. The formation of a coherent interface implies that the adjoining crystals, if misfitting, have been strained in order to maintain the coherence. On the other hand, the formation of an incoherent interface implicitly relaxes lattice strain. These effects are well-known for other phase transformations and in the growth of epitaxial thin films. Because of the high elastic moduli of inorganic compounds, percent-level differences in strain can have enormous impact on failure and coherency (the strain to failure of ceramic crystals is typically much less than 1 %). Even in very thin films, less than ca. 1% lattice strain is typically required in order to obtain a coherent interface.<sup>23</sup> Sample NC, despite having a lower lattice misfit than sample AC, nonetheless shows higher retained strain in both the triphylite and heterosite phases, 0.66% and 0.36 %, respectively (Table 4-I). This suggests that if coherency is producing the retained strain, the misfit has not been relieved. Sample AC, by contrast, has negligible retained crystallographic strain (0.02% and 0.05 %). This would be consistent with the formation of incoherent, strain-relieving interfaces. However, an alternative explanation for the retained strain is a variation in lithium stoichiometry due to a distribution of particle sizes. Although particles within a composite electrode such as those used here are expected to rapidly come to equilibrium with one another, the Gibbs–Thomson effect dictates that their individual compositions may vary. The importance of this effect can be evaluated once the particle size distributions are known.

## Thermodynamic Model

Stored elastic energy may therefore contribute to the thermodynamics of two-phase reactions. While electrochemically induced volume changes leading to fracture of storage materials have been widely postulated as a cause of capacity loss and poor cycle life (these strains have also recently been used to advantage for mechanical actuation<sup>24,25</sup>), to our knowledge the thermodynamic effects of mechanical strain energy have not been treated. Interfacial energy terms may also be important in opposing or promoting phase transformation, especially in nanoscale materials. The following nucleation theory for strained intercalation compounds takes these contributions into account. Although the principles apply to any intercalation compound that undergoes a volume change with composition (i.e., the ions occupy interstitial sites), including materials cycled predominantly within a solid-solution field such as  $\text{LiCoO}_2$  and  $\text{LiMn}_2\text{O}_4$ , for simplicity we consider compounds that undergo a first-order phase transition, a class that includes the olivines,  $\text{Li}_4\text{Ti}_5\text{O}_{12}$ ,<sup>26</sup> and the “lithiated spinel”  $\text{Li}_2\text{Mn}_2\text{O}_4$ .<sup>27</sup> The molar free energy versus lithium concentration at fixed temperature for two coexisting bulk phases in the absence of elastic energy is depicted in Figure 4-6a. Considering a positive electrode and a negative electrode of constant lithium chemical potential (e.g., lithium metal), the cell voltage is  $\mu_{\text{Li}} = \phi^+ - \phi^-$ , the difference in chemical potential is  $\mu_{\text{Li}} = \mu_{\text{Li}}^+ - \mu_{\text{Li}}^-$ , and at equilibrium the two are related by  $ZF\Delta\phi = -\Delta\mu_{\text{Li}}$  if there are no other effects accompanying the production of a second phase such as those considered below. Electroneutrality requires  $Zn_e$  moles of electrons to be transferred for  $n\text{Li}$  moles of the ion;  $Z=1$  for lithium. The tangent to the free energy curve intersects the right vertical axis (representing one mole of lithium transported at chemical potential  $\mu_{\text{Li}}^+$ ) at a value  $-F\Delta\phi(x)$  that gives the equilibrium cell voltage. The cell voltage  $\Delta\phi(x)$  decreases with increasing lithium concentration for compositions in the left single-phase field up to  $x = x^1$ , has a constant value for compositions in the two-phase field between  $x^1$  and  $x^2$ , and decreases again within the right single-phase field for  $x > x^1$ . Now consider the formation of a new phase with lattice distortion compared to the pre-existing phase. If the interface between the two phases does not permit sliding (i.e., a perfectly coherent interface) or the geometry of the two phases within the particle prohibits sliding (e.g., a spherical shell



surrounding a sphere of one phase), then the stored elastic energy raises the system's potential energy. Considering reversible isothermal changes in the system's potential energy, it can be shown that two-phase equilibrium occurs when

$$FZ\Delta\phi = \Delta\mu_L + \frac{V_M^I}{C} \frac{du_{elstc}}{V_f} \quad (1)$$

where  $V_f$  is the volume fraction of phase 2 in a total volume  $V_T$  of electrode material,  $C$  is the number of lithium atoms to convert phase 1 to phase 2,  $V_M^I$  is the molar volume of initial phase 1, and  $u_{elstc}$  is the elastic energy per volume  $V_T$ .

A "core/shell" model<sup>1</sup> whereby the newly formed phase uniformly coats the pre-existing phase has been widely adopted to explain the behavior of olivines. Approximating the electrode material as spherical particles, the new phase would form a spherical shell, in which case  $u_{elstc}$  can be calculated exactly and directly from the equations of isotropic elastic equilibrium assuming identical elastic constants  $E$  (Young's modulus) and  $\nu$  (Poisson's ratio) for both phases. For small  $\Delta V_M/V_M^I$ , this exact result for the elastic energy density is approximated by

$$u_{elstc} \approx \frac{\left(\frac{\Delta V_M}{V_M^I}\right)^2 EV_f (V_f - 1)}{9(1 - \nu)} \quad (2)$$

where  $\Delta V_M = V_M^{II} - V_M^I$  is the difference in molar volume.

For at least two reasons, the assumption of a shell of uniform thickness is implausible. First, there are alternative configurations of lower elastic energy. We used a finite element method to calculate  $u_{elstc}$  for a geometry consisting of a spherical cap of phase 2 with a flat coherent interface separating it from the rest of the sphere of phase 1. The calculated elastic energy is less than that of the shell (Eq. 2) by a factor of 10/3 as shown by Figure 4-7. In anisotropic crystals such as the present one, the ability to choose planes of low misfit and orientations of lower elastic modulus further reduces the energy of the cap configuration. Although the computed increases to the equilibrium potential  $\Delta\phi$  due

to elastic energy alone are modest, on the order of tens of millivolts, the cap configuration is clearly preferred. A second reason the spherical shell geometry is not preferable derives from nucleation considerations: the first infinitesimal increment in  $V_f$  requires a finite interfacial area (the sphere area) for the spherical shell configuration but an infinitesimal interfacial area for the cap configuration. Thus to formulate a nucleation model, we first take the major components of the volumetric energy to be the chemical and elastic energies. Referring to Figure 4-6b, a slightly super-saturated solid solution of the delithiated phase (e.g.,  $\text{Li}_y\text{FePO}_4$ ) that is stress-free has a lower equilibrium potential  $\Delta\phi(x)$  than that of the equilibrium composition. When any portion of the supersaturated solution then transforms to a two-phase configuration, the molar free energy change, represented by the vertical distance  $\Delta A^{\text{ovr}}$ , can be positive or negative depending on the lattice misfit, elastic constants, geometrical configuration of the initial and nucleated phases, and the magnitude of the applied overpotential. Evaluating numerically, we find that a several folds larger overpotential is required for  $\Delta A^{\text{ovr}}$  to become negative for the spherical shell than for the cap configuration. Upon adding the interfacial energy between phases 1 and 2, which is the product of interfacial tension,  $c$ , and the interfacial area (readily written in terms of  $V_T$  and  $V_f$  for the shell and cap geometries), the driving force for the energetically-preferred spherical cap configuration is

$$\Delta A_{\text{net}}^{\text{cap}}(V_f) = \Delta A^{\text{ovr}} V_T V_f + g \gamma V_f^{2/3} V_T^{2/3} \quad (3)$$

where  $g$  is a geometrical constant of order unity related to the interfacial area. Note that the first term is negative and the second positive; both include a dependence on the transformed fraction,  $V_f$ . There exists a critical  $V_f$  at which the driving force for transformation becomes negative (otherwise a solid solution is preferred), given by  $V_{f,\text{crit}}$

$$V_{f,\text{crit}} = \frac{-8g^3 \gamma^3}{27(\Delta A^{\text{ovr}})^3 V_T} \quad (4)$$

A large negative volume energy  $\Delta A^{\text{ovr}}$  reduces the critical fraction while the strong sensitivity to interfacial energy,  $c$ , indicates that a large misfit creating incoherent interfaces will increase the overpotential needed to induce transformation. The interfacial

energy barrier to nucleation is minimized by having low interface tension  $c$ , which for the present olivines is probably best satisfied by interfaces forming on the  $\{100\}$  plane. Although the present calculation is for spheres, this will be true for any relatively equiaxed particle shape, as well as anisometric shapes where the smallest cross-section falls on the  $\{100\}$  plane. Returning to the experimental data, in light of these considerations, for sample AC, both an abrupt overpotential seen during the continuous charging at the beginning of the two-phase voltage plateau (Figure 4-2) and the unusual kinetic response at constant overpotential (Figure 4-5) strongly suggest that a barrier to phase transformation must be overcome. Both features are absent in the high rate capability sample NC of lower misfit. Note that the form of the elastic energy versus volume fraction transformed (Figure 4-6b and Figure 4-7) is similar to the rate of phase transformation (current flow) versus extent of transformation at a constant overpotential in Figure 4-5.

### **Kinetic Limitations in the Presence of Incoherent Interfaces**

For sufficiently large elastic misfit, other, kinetic limitations must also be considered. We hypothesize that for large enough lattice misfit, and at a critical volume fraction, interface dislocations are nucleated and cause the interface to become incoherent. The incoherent interface should have a markedly slower migration rate. Unlike a coherent interface that can migrate due to Li transport alone, the strain-accommodating dislocations in an incoherent interface comprise discontinuities in the other atomic sub-lattices of the olivine structure (e.g., Fe, P, or O) and cannot be removed simply by the addition or removal of lithium. Instead, as with other such interfaces, the phase boundary may only move at a rate slow enough to allow the dislocations to be annihilated by climb and glide processes to the particle surface. This means that diffusion of an atomic species other than lithium may become rate-limiting. Under cyclic conditions, we may imagine that the transforming crystal faces the following dilemma. Either the phase transformation proceeds at a slow rate limited by dislocation migration, or additional dislocations may be generated with each pass of the interface. The first creates a rate-limiting step that is likely much slower than the chemical diffusion rate of lithium, and the second presents an additional energy barrier to the transformation, as well as accumulating damage that can

eventually cause fracture of the particles. Indeed, transmission electron microscopy of sample AC after 30 high-rate charge/discharge cycles reveals a high density of dislocations (Figure 4-8), as observed in other compounds such as  $\text{LiCoO}_2$ .<sup>28</sup> Extended defects of any kind were difficult to detect in the NC particles.

### **Summary and Conclusions**

Extended lithium nonstoichiometry has been observed in both end-member phases of high rate doped nanoscale lithium iron phosphates, associated with which is a reduction in the lattice misfit between coexisting phases in comparison to conventional materials. In the NC sample studied here, the nonstoichiometry measured at room temperature would otherwise be attained in a conventional material only at elevated temperatures of 200–400 °C.<sup>9,17</sup> The coexistence of  $\text{Fe}^{2+}$  and  $\text{Fe}^{3+}$  in the solid solution, and the associated changes in lattice parameters and bond lengths of the nonstoichiometric solid solutions, should be expected to alter the electronic structure, increase electronic conductivity, and possibly influence ionic conductivity in comparison with conventional samples. As proposed previously,<sup>3</sup> it is likely that electronic conductivity will be improved to where it is no longer rate-limiting. Beyond altered transport coefficients, however, the elastic strain affects both thermodynamic and kinetic aspects of the phase transition. It is suggested that high-rate materials are able to retain coherent interfaces throughout nucleation and growth of the new phase, providing “facile” phase transformation. A partially transformed material may consist of two-phase particles, or may relax to an assembly in which each particle is purely one phase or the other in order to avoid the energy penalty of a retained interface. However, lithiation or delithiation of the assemblage as a whole will require nucleation and propagation of a new phase within individual particles. In olivines, reduced misfit along the {100} plane may be an important factor. This, we suggest, is as important to high rate capability as improvements in ionic and electronic transport. Generality of the proposed model is suggested by correlations between elastic misfit and rate capability in several other lithium intercalation oxides exhibiting first-order phase transitions. The poor rate capability of  $\text{LiMnPO}_4$  compared to  $\text{LiFePO}_4$  has been attributed solely to its low electronic conductivity.<sup>11,12</sup> However, there is also a much larger misfit between the

phases (ca. 10 vol %, Table 4-I) than in  $\text{LiFePO}_4$ . The fact that even nanoscale  $\text{LiMnPO}_4$  has a much poorer rate capability<sup>13</sup> than conventional  $\text{LiFePO}_4$ -based materials suggests that lattice misfit plays an important role.  $\text{Li}_4\text{Ti}_5\text{O}_{12}$ , on the other hand, is a cubic spinel known for having nearly zero dimensional change between its lithiated and delithiated phases,<sup>26</sup> and is also known for having exceptional rate capability when produced in nanoscale form.<sup>28</sup> A third example is the spinel  $\text{LiMn}_2\text{O}_4$ . Between the composition limits  $\text{MnO}_2$  and  $\text{Li}_{0.5}\text{MnO}_2$ , there exists a continuous solid-solution cubic spinel that is known for its high rate capability—this spinel is the basis for certain high-power lithium-ion batteries. However, upon further lithiation, a first-order phase transition from  $\text{Li}_{0.5}\text{MnO}_2$  to tetragonal “ $\text{Li}_2\text{Mn}_2\text{O}_4$ ” occurs with a 5.6% volume misfit and 16% change in the  $c/a$  ratio.<sup>26,29</sup> The rate capability in this regime is found to be markedly inferior to that of the cubic spinel.<sup>30</sup> We know of no counterexamples in which high rate capability is obtained for a phase transformation of large misfit. Thus, a strain-based predictive criterion for the design and selection of high power battery electrode compounds is suggested.

## References

1. A. K. Padhi, K. S. Najundaswamy, J. B. Goodenough, *J. Electrochem. Soc.*, **144**, 1188 (1997).
2. A. S. Andersson, J. O. Thomas, B. Kalska, L. Häggström, *Electrochem. Solid-State Lett.*, **3**, 66 (2000).
3. S. Y. Chung, J. T. Bloking, Y.-M. Chiang, *Nat. Mater.*, **1**, 123 (2002).
4. S. Y. Chung, J. T. Bloking, Y.-M. Chiang, *Nat. Mater.*, **2**, 702 (2003).
5. Ravet et al. [6] contended that the high rate capability was due to inadvertent carbon coating, despite TEM evidence to the contrary [2]. Striebel et al. [7] attributed the rate capability to particle size alone, arguing that their “core/shell” transport model could adequately model the behavior without changing the assumed chemical diffusion coefficient of lithium. Subramanya Herle et al. [10] argued that the high electronic conductivities reported by Chung et al. were due to nanoscale networks of phosphide-carbide phases, but their observations were of sintered pellets and no electrochemical measurements were reported. Delacourt et al. [8,9] have argued firstly that aliovalent doping of  $\text{LiFePO}_4$  is not possible, and

secondly that the process used by Chung et al. results in conductive coatings of carbon or metal phosphides on the particles, again despite high-resolution microscopy results refuting both [3]. Neither Delacourt et al. [8] nor Subramanya Herle et al. [10] provided electrochemical tests of their doped materials.

6. N. Ravet, A. Abouimrane, M. Armand, *Nat. Mater.*, **2**, 702 (2003).
7. K. Striebel, J. Shim, V. Srinivasan, J. Newman, *J. Electrochem. Soc.*, **152**, A664 (2005).
8. C. Delacourt, C. Wurm, L. Laffont, F. Sauvage, J.-B. Leriche, R. Bouchet, M. Morcrette, J.-M. Tarascon, C. Masquelier, in *Proc. MRS Fall Meeting* (Eds: P. Knauth, C. Masquelier, E. Traversa, E. D. Wachsman), The Materials Research Society, Warrendale, PA, 321 (2004).
9. C. Delacourt, P. Poizot, J.-M. Tarascon, C. Masquelier, *Nat. Mater.*, **4**, 254 (2005).
10. P. Subramanya Herle, B. Ellis, N. Coombs, L. Nazar, *Nat. Mater.*, **3**, 147 (2004).
11. A. Yamada, S. C. Chung, *J. Electrochem. Soc.*, **151**, A1352 (2004).
12. C. Delacourt, L. Laffont, R. Bouchet, C. Wurm, J.-B. Leriche, M. Morcrette, J.-M. Tarascon, C. Masquelier, *J. Electrochem. Soc.*, **152**, A913 (2005).
13. N. H. Kwon, T. Drezen, I. Exnar, I. Teerlinck, M. Isono, M. Grätzel, *Electrochem. Solid-State Lett.*, **9**, A277 (2006).
14. V. Srinivasan, J. Newman, *J. Electrochem. Soc.*, **151**, A1517 (2004).
15. A. Chu, *Development of HEV batteries with lithium iron phosphate cathodes*, presented at the Advanced Automotive Battery Conf., Baltimore, MD, June 2006. See also: [www.A123Systems.com](http://www.A123Systems.com).
16. A. Yamada, H. Koizumi, N. Sonoyama, R. Kanno, *Electrochem. Solid-State Lett.*, **8**, A409 (2005).
17. J. L. Dodd, R. Yazami, B. Fultz, *Electrochem. Solid-State Lett.*, **9**, A151 (2006).
18. A. Yamada, Y. Takei, H. Koizumi, N. Sonoyama, R. Kanno, K. Ito, M. Yonemura, T. Kamiyama, *Nat. Mater.*, **5**, 357 (2006).
19. See for example: a) Y.-M. Chiang, A. F. Henriksen, W. D. Kingery, D. Finello, *J. Am. Ceram. Soc.*, **64**, 383 (1981). b) J. A. S. Ikeda, Y.-M. Chiang, *J. Am. Ceram.*

- Soc.*, **76**, 2437 (1993). c) J. A. S. Ikeda, Y.-M. Chiang, A. J. Garratt-Reed, J. B. Vander Sande, *J. Am. Ceram. Soc.*, **76**, 2447 (1993).
20. N. Meethong, H.-Y. S. Huang, W. C. Carter, Y.-M. Chiang, *Electrochem. Solid-State Lett.*, **10** (5), A134 (2007).
  21. T. Maxisch, G. Ceder, *Phys. Rev. B*, **73**, 174 112 (2006).
  22. G. Chen, X. Song, T. Richardson, *Electrochem. Solid-State Lett.*, **9**, A295 (2006).
  23. E. A. Fitzgerald, *Dislocations in Strained-Layer Epitaxy: Theory, Experiments, and Applications*, North-Holland, New York (1991).
  24. Y. Koyama, T. E. Chin, U. Rhyner, R. K. Holman, S. R. Hall, Y.-M. Chiang, *Adv. Funct. Mater.*, **16**, 492 (2006).
  25. T. E. Chin, U. Rhyner, Y. Koyama, S. R. Hall, Y.-M. Chiang, *Electrochem. Solid-State Lett.*, **9**, A134 (2006).
  26. K. Ariyoshi, R. Yamato, T. Ohzuku, *Electrochim. Acta*, **51**, 1125 (2005).
  27. M. M. Thackeray, *Prog. Solid State Chem.*, **25**, 1 (1997).
  28. H. Wang, Y.-I. Jang, B. Huang, D. R. Sadoway, Y.-M. Chiang, *J. Electrochem. Soc.*, **146**, 473 (1999).
  29. L. Kavan, J. Procházka, T. M. Spitler, M. Kalbáč, M. Zúkalová, T. Drezen, M. Grätzel, *J. Electrochem. Soc.*, **150**, A1000 (2003).
  30. Y.-M. Chiang, H. Wang, Y. Jang, *Chem. Mater.*, **13**, 53 (2001).
  31. N. Meethong, D.-W. Kim, Y.-M. Chiang, unpublished.
  32. A. Yamada, S.-C. Chung, *J. Electrochem. Soc.*, **148**, A960 (2001).
  33. A. S. Anderson, J. O. Thomas, *J. Power Sources*, **81**, 463 (1999).

## Chapter 4 Figures and Tables

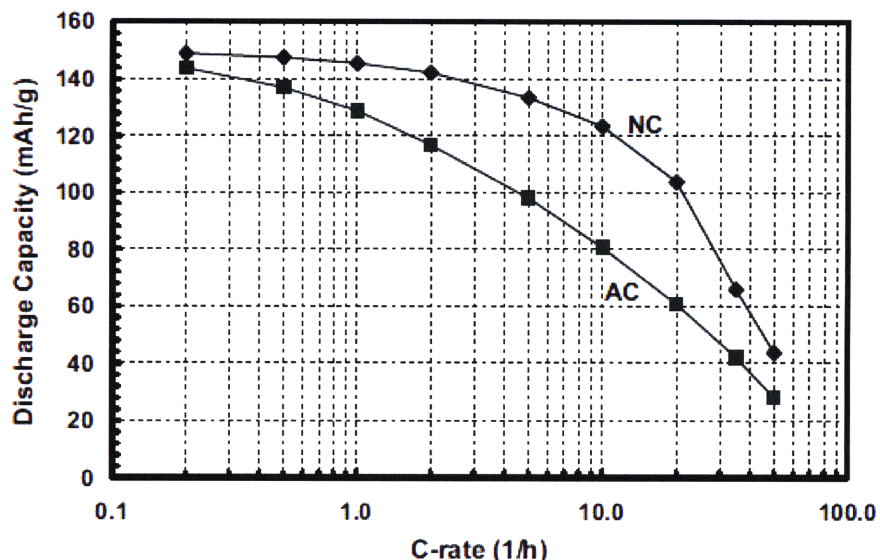


Figure 4-1: Comparison of specific discharge capacity versus galvanostatic C rate for samples NC (top) and AC (bottom), representing high-rate doped nanoscale and “carbon-added” lithium iron phosphates respectively, measured in lithium half-cells of Swagelok™ type. Before each discharge, cells were charged at C/2 rate and held at 3.80 V until the current decays to C/25 rate.

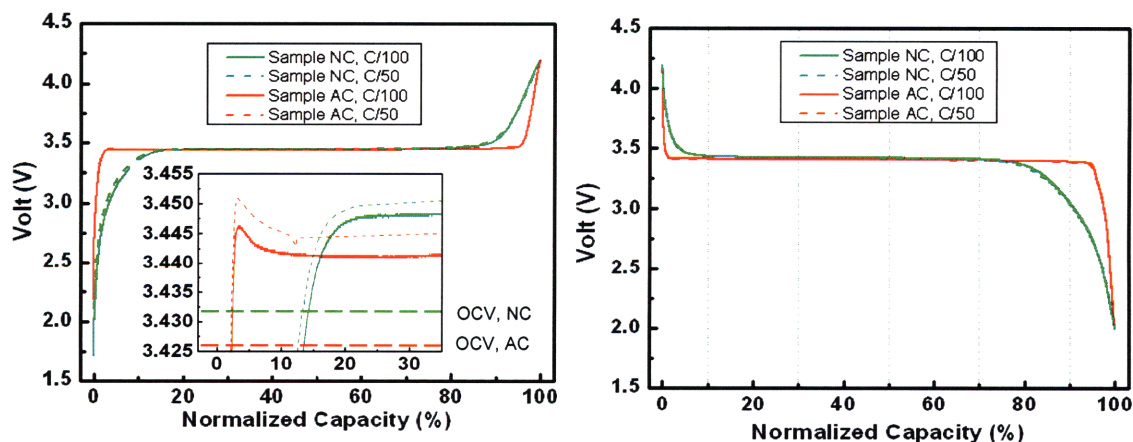


Figure 4-2: Galvanostatic charging (left) and discharge (right) at C/50 and C/100 rates shows the narrower composition range over which high rate doped nanoscale powders (sample NC) exhibit a constant cell voltage indicating two-phase coexistence, compared to the lower rate carbon-added sample AC. Note also the overpotential measured on charge for sample AC as the two-phase plateau voltage is approached, absent for sample NC (inset). OCV differs slightly for the two samples as discussed in text, indicated in inset.



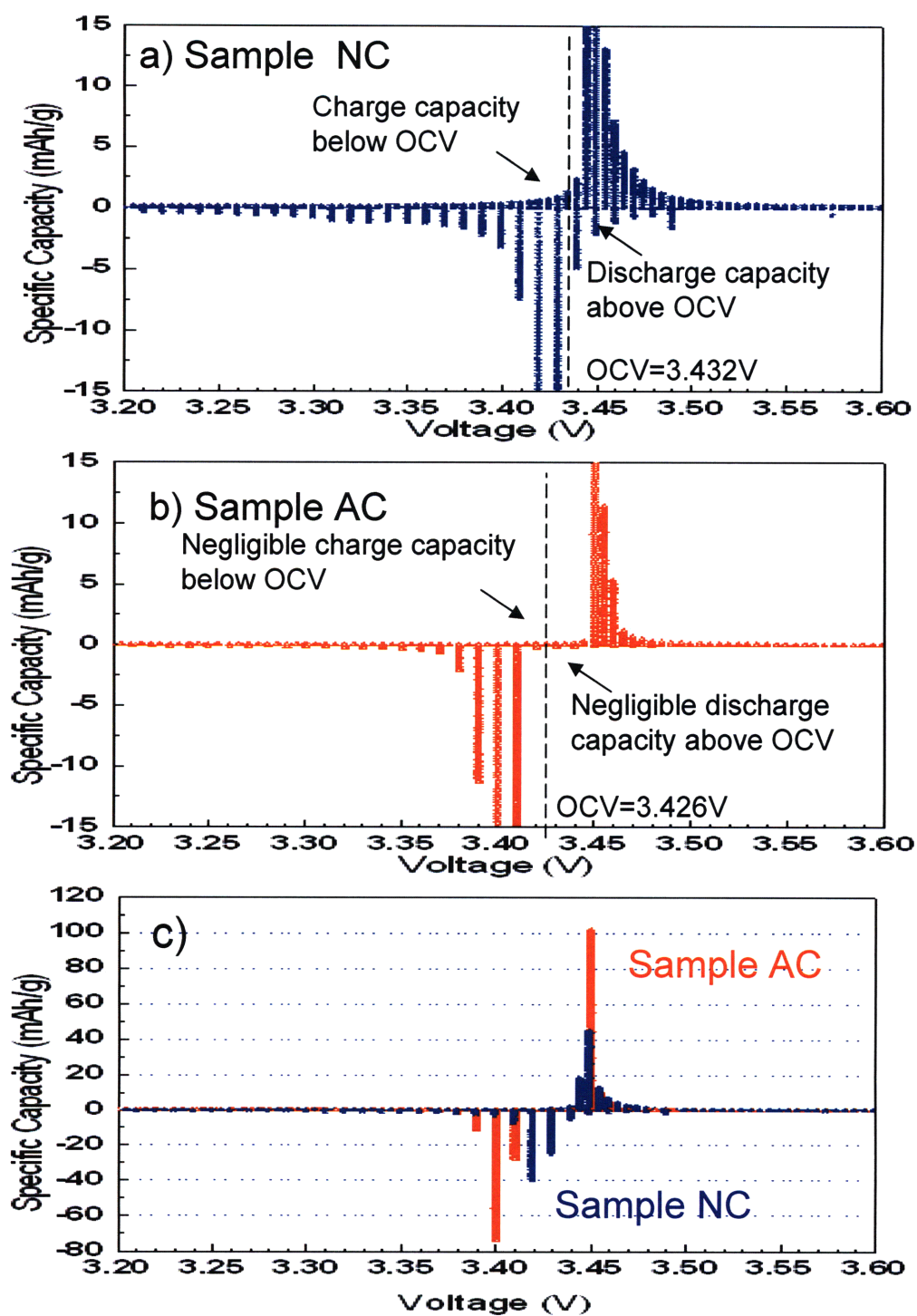


Figure 4-3: Capacity versus voltage measured potentiostatically upon charge and discharge in 10 mV steps. The OCV is indicated for each cell. a) Nb-doped nanoscale sample NC; b) carbon-added undoped  $\text{LiFePO}_4$  sample AC. c) Full-scale representation of the data.

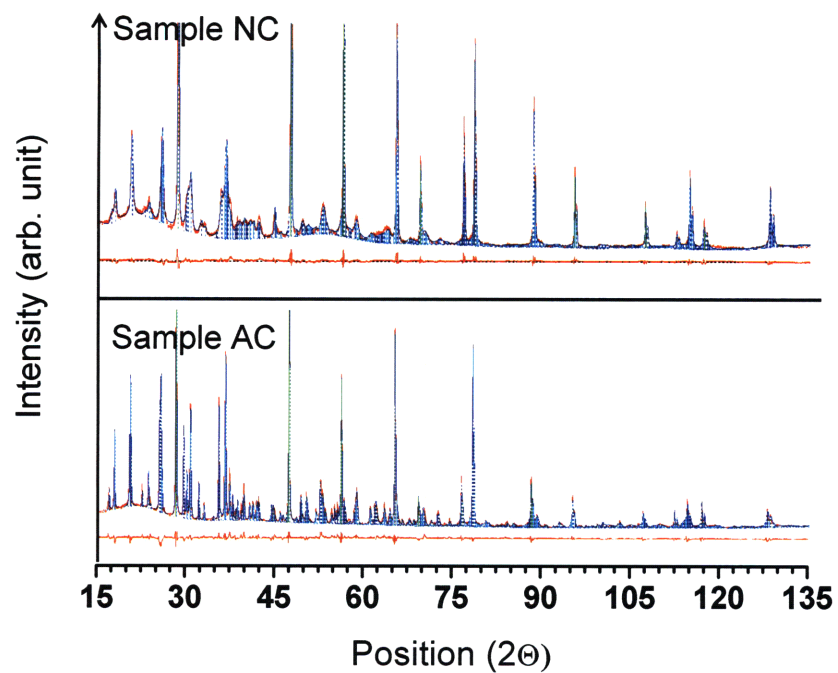


Figure 4-4: Rietveld refined X-ray patterns for samples NC and AC respectively at ca. 50% state of charge, including the fit to Si powder added as an internal standard. The observed intensity data are shown by the solid red line, and the dashed blue, aqua, and green lines overlying them are the calculated intensity of  $\text{LiFePO}_4$ ,  $\text{FePO}_4$ , and Si respectively. The dashed lines are the calculated intensity of the aluminum peaks from the current collector. The difference between the observed and calculated intensities is shown for each of the pattern. The structural results are shown in Table 4-I.

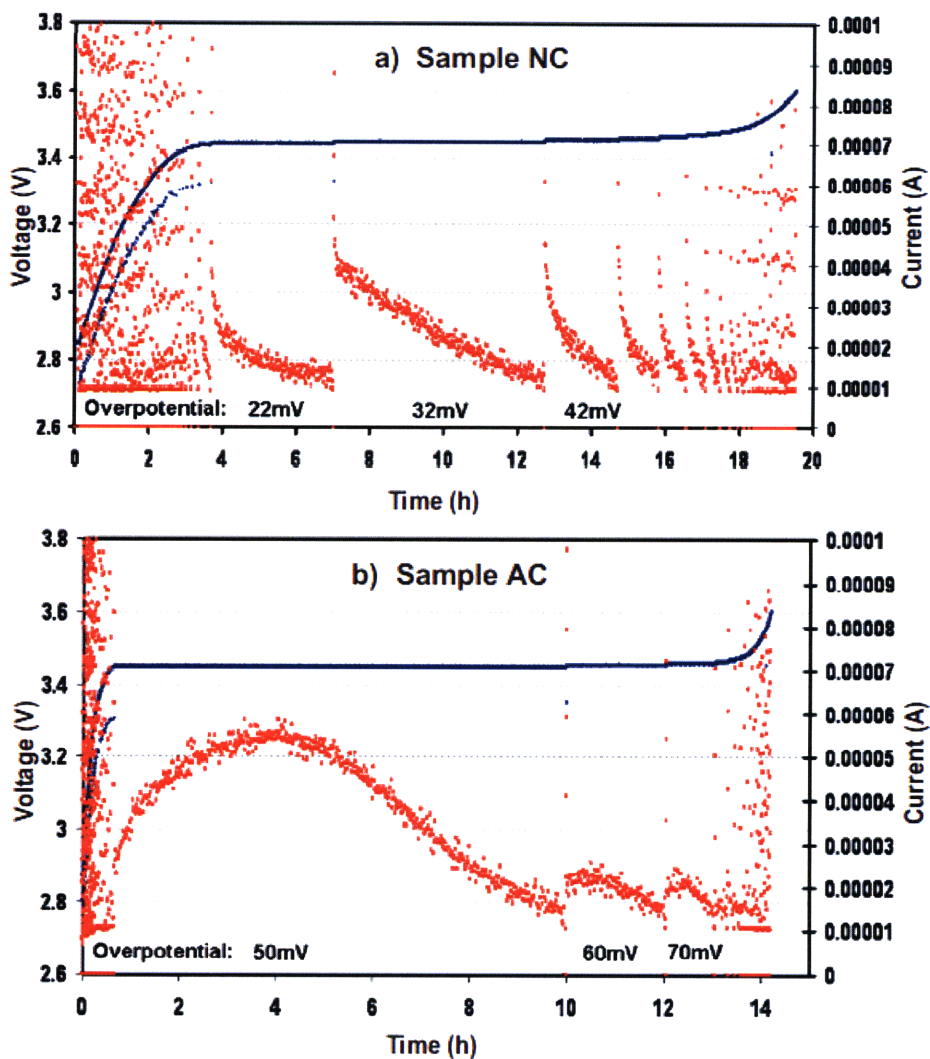
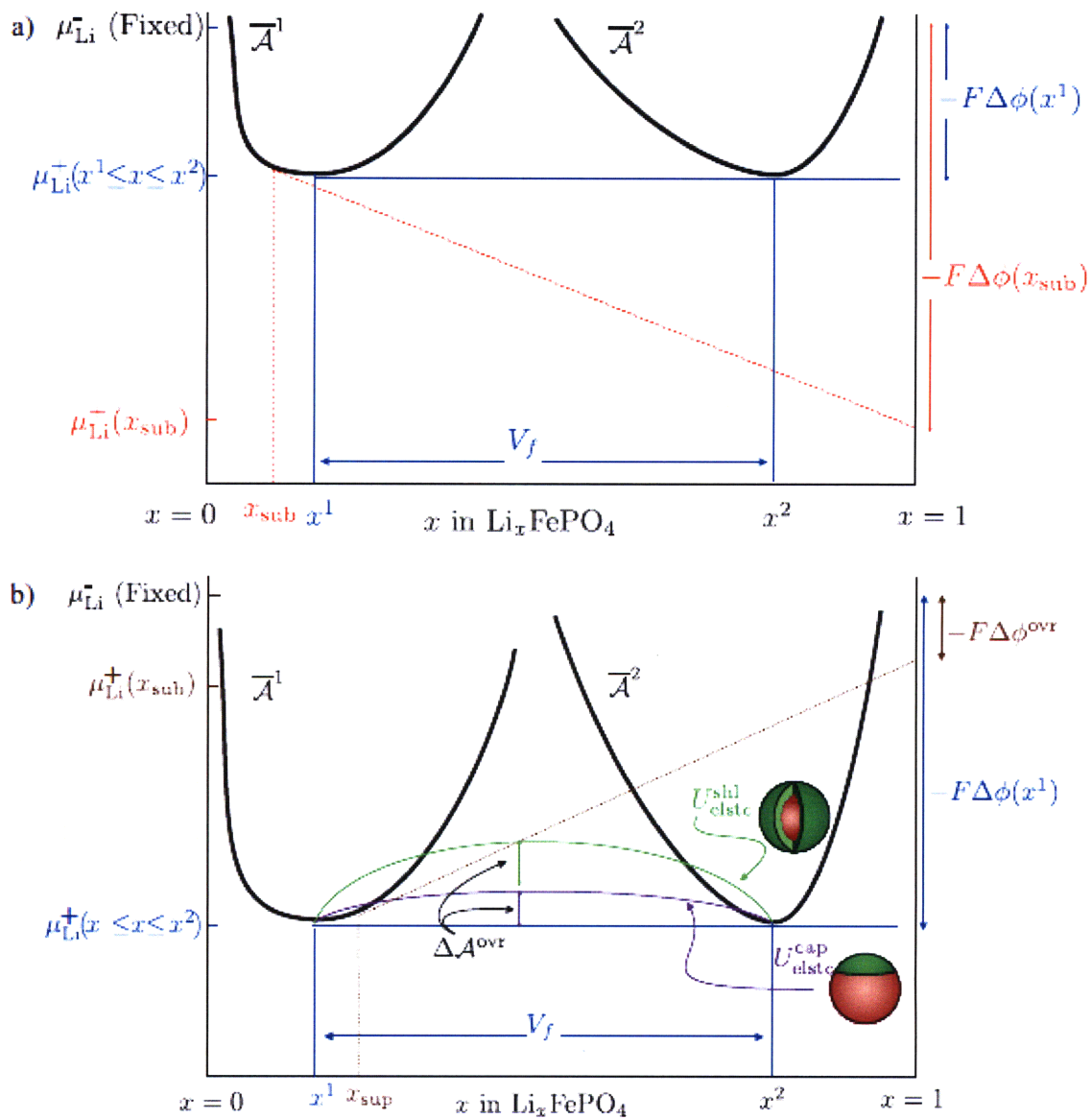


Figure 4-5: Voltage steps (black) and corresponding current relaxation (red) during PITT measurements (10 mV steps,  $C/50$  current cutoff) in the second charge cycle, indicating rate of phase transformation as a function of the applied potential. a) Doped nanoscale sample NC exhibits peak current at the start of each voltage step, followed by monotonically decaying current, at all overpotentials. b) Comparison sample AC exhibits a slow increase in the current at constant voltage, peaking nearly 4 h after the application of overpotential, indicating a time-varying barrier to phase transformation. Higher overpotentials are also required for phase transformation.



**Figure 4-6:** a) Molar free energy of two positive electrode phases illustrating tangent construction relating chemical potential differences and electromotive force in the absence of stored elastic energy. The reference energies are scaled so that the common tangent has zero slope. b) Within the two-phase region, a coherent interface between phases differing in molar volume produces an additional contribution to the molar free energy and is illustrated for the case of a spherical shell and spherical cap.

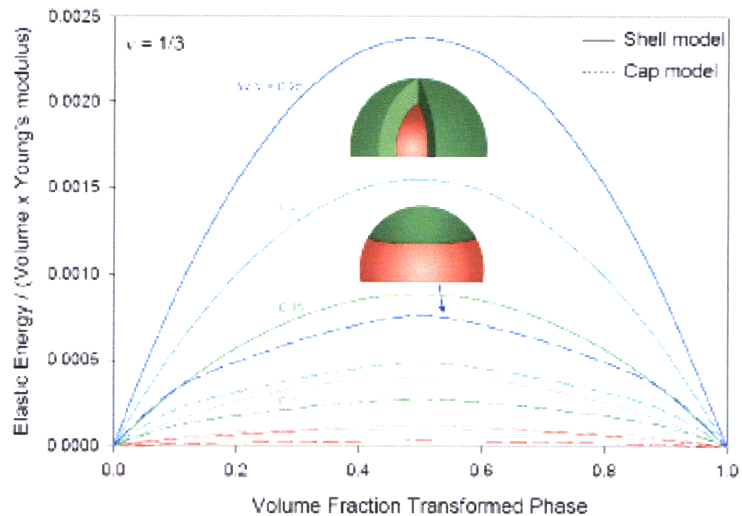


Figure 4-7: Elastic energy normalized to volume and Young's modulus  $E$ , vs. volume fraction transformed phase, for the case of a spherical shell and a spherical cap. Poisson's ratio  $\nu$  is assumed to be  $1/3$ .

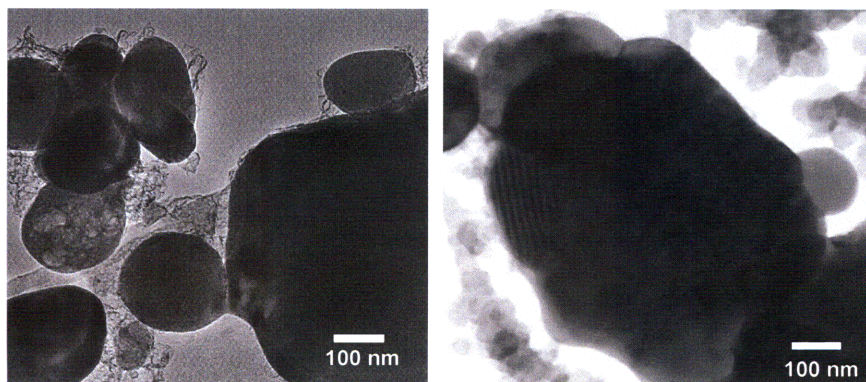


Figure 4-8: Transmission electron micrographs of starting powders of Sample AC (left) and after high rate cycled showing a high density of dislocations (right).

**Table 4-I: Physical and structural characteristics of a high rate doped nanoscale (Sample NC) and lower-rate “carbon-added” lithium iron phosphate (Sample AC), compared with literature data for  $\text{LiFePO}_4$  and  $\text{LiMnPO}_4$ .**

	Sample NC	Sample AC	Padhi (1)	Yamada (16)	Yamada (16)	Yamada (18)	Andersson (33)	Yamada (32)
Compositional state	~50% SOC	~50%SOC	Stoichiometric	Stoichiometric	Solid solution limits	Stoichiometric	Stoichiometric	Stoichiometric
Specific Surface Area ( $\text{m}^2/\text{g}$ )	39.2	14.8	Not reported	7-13	7-14	Not reported	Not reported	Not reported
Carbon Content (wt%)	2.4	1-3*	Not reported	8	8	Not reported	Not reported	Not reported
<b><math>\text{LiFePO}_4</math> phase</b>								<b><math>\text{LiMnPO}_4</math></b>
<i>a</i> (Å)	10.232	10.3289	10.334	10.323	10.309	10.32287	10.329	10.46
<i>b</i> (Å)	5.941	6.0069	6.008	6.0065	6.001	6.00496	6.0065	6.11
<i>c</i> (Å)	4.73	4.6905	4.693	4.693	4.698	4.69094	4.6908	4.75
V (Å <sup>3</sup> )	287.502	291.0224	291.392	290.99	290.64	290.784	291.02	303.58
Strain (%)	0.66	0.02						
Crystallite size (Å)	266	1145.4						
<b><math>\text{FePO}_4</math> phase</b>								<b><math>\text{MnPO}_4</math></b>
<i>a</i> (Å)	9.887	9.8267	9.821	9.817	9.829	9.81465	9.8142	9.64
<i>b</i> (Å)	5.838	5.7944	5.792	5.79	5.7995	5.7887	5.7893	5.92
<i>c</i> (Å)	4.7786	4.7832	4.788	4.7822	4.7793	4.78107	4.782	4.773
V (Å <sup>3</sup> )	275.824	272.3572	272.357	272.82	272.44	271.632	271.7	272.39
Strain (%)	0.355	0.05						
Crystallite size (Å)	276.3	799.6						
<b>Misfit (%)</b>								
Linear Strain								
<i>a</i> axis	3.430	4.983	5.091	5.025	4.767	5.047	5.111	8.159
<i>b</i> axis	1.749	3.601	3.661	3.671	3.415	3.667	3.683	3.159
<i>c</i> axis	-1.022	-1.957	-2.004	-1.883	-1.716	-1.903	-1.926	-0.483
Volume strain	4.146	6.626	6.753	6.445	6.464	6.811	6.867	10.830
Planar Strain								
<i>a-b</i> plane	5.178	8.581	8.747	8.691	8.179	8.711	8.790	11.311
<i>a-c</i> plane	2.408	3.027	3.087	3.143	3.052	3.145	3.187	7.677
<i>b-c</i> plane	0.727	1.645	1.657	1.788	1.700	1.765	1.757	2.676

\*Quoted by manufacturer

\*\*Taken as the difference/mean value

# Chapter 5

## Electrochemically Induced Phase Transformation in Nanoscale Olivines $\text{Li}_{1-x}\text{MPO}_4$ (M = Fe, Mn)

We previously documented several key differences in phase transformation behavior between conventional particle sized and nanoscale (<100 nm) olivine positive electrodes. Using electrochemical titration and structural (Vegard's law) measurements, it was shown that nanoscale (<50nm)  $\text{Li}_{1-x}\text{FePO}_4$  has a size-dependent, reduced miscibility gap compared to coarser-grained materials (Chapter 3). In doped nanoscale phosphates the miscibility gap is narrower still (Chapter 4). To further study stability and phase transformation kinetics of  $\text{Li}_{1-x}\text{MPO}_4$  olivines, in this chapter, nanoscale (<100 nm primary particle size)  $\text{Li}_{1-x}\text{FePO}_4$  and  $\text{Li}_{1-x}\text{MnPO}_4$  are chosen as model systems for comparison with a coarser-grained  $\text{LiFePO}_4$  that exhibits a conventional two-phase reaction.

Here, the state-of-charge and time dependence of the open-circuit voltage of half-cells and detailed examination of the structural parameters and phase content were investigated. It is shown that the phase transformation path differs significantly between the nanoscale and (<100nm) and conventional  $\text{Li}_{1-x}\text{MPO}_4$  materials. The evolution of structural parameters supports the existence of a coherency-stress influenced crystal-crystal transformation. However, an additional response, the preferential formation of amorphous phase at nanosize scale, is identified. In  $\text{Li}_{1-x}\text{MnPO}_4$  of 78 nm particle size, the electrochemically formed delithiated phase is highly disordered. These phenomena are interpreted from the effect of surface and bulk energetic on phase stability of a nanoscale material.

---

Reproduced with permission from *Chem. Mater.*, **20**, 6189 (2008). Copyright 2008, The American Chemical Society.]

## Introduction

Although the applications for lithium transition metal olivine cathodes were initially uncertain due to their inferior energy density compared to, for instance,  $\text{LiCoO}_2$ , the recent commercialization of compositionally modified nanoscale olivines in applications such as cordless power tools<sup>1</sup> and hybrid electric vehicles (HEV)<sup>2,3</sup> suggests an important future role in high power, safe, long-lived rechargeable batteries. In these applications, the phase behavior and phase transformation kinetics are critical, given that the equilibrium phase diagram shows limited solubility between the lithiated and delithiated phases<sup>4-6</sup> and requiring a first-order phase transformation during electrochemical cycling. We previously documented several key differences in phase transformation behavior between conventional particle sized and nanoscale (<100 nm) olivine positive electrodes. Using electrochemical titration and structural (Vegard's law) measurements, it was shown that nanoscale (<50nm)  $\text{Li}_{1-x}\text{FePO}_4$  has a size-dependent, reduced miscibility gap compared to coarser-grained materials.<sup>7</sup> In doped nanoscale phosphates the miscibility gap is narrower still.<sup>8,9</sup> A size-dependent phase diagram has also been reported for  $\text{Li-TiO}_2$  by Wagemaker *et al.*<sup>10</sup> In the olivines, it was furthermore shown that when the lattice mismatch between the co-existing lithium-rich and lithium-poor phases is sufficiently reduced, the phase transformation kinetics as measured by potentiostatic intermittent titration test (PITT) are qualitatively different than for samples of even slightly coarser size (113nm) in which the coexisting phases have a larger misfit.<sup>8</sup> At small overpotentials, the latter show nucleation-limited behavior with phase transformation rates that increase slowly over many hours and cannot be modeled by any simple diffusion law,<sup>11</sup> while the doped nanomaterials show facile transformation with a rapid, monotonic decay in transformation rate. Combined with X-ray diffraction evidence for higher retained strain in the nanomaterials, it was proposed that relief of the misfit strain facilitates high rate capability.<sup>8</sup> It was suggested that reducing the elastic misfit was a fruitful approach to obtaining high ion exchange rates in phase-transforming systems in general.

There may furthermore be differences in the way a single particle accommodates the phase transformation compared to a multiparticle assembly that is able to redistribute



lithium between particles in order to reduce excess energy. Clearly a single particle that is partially transformed must accommodate both phases within the same crystallite, assuming no fracture. However, a partially-transformed multiparticle system can relax to a more energetically favorable assembly consisting of a mixture of single-phase particles of the two phases, since the retention of partially transformed particles possessing either coherency stresses or incoherent interfaces is metastable. Whether this state is achieved in practice depends on kinetics: the rate of lithium redistribution relative to the time scale on which the material is being electrochemically cycled. This led us to expect a possible evolution of the phase distribution over time in electrodes that are at a fixed overall composition (i.e., state-of-charge).

The increased surface area to volume ratio alone of nanoparticles may also lead to a contribution of surface defects or solute segregation to the observed phase behavior. To cite some previous examples, interfacial solute segregation has been observed to increase the “macroscopic” solubility limit of CaO in nanocrystalline TiO<sub>2</sub>,<sup>12</sup> and increased nonstoichiometry has been observed in nanoscale CeO<sub>2-x</sub> due to the lower oxygen vacancy formation enthalpy at interfaces.<sup>13</sup> The well-known formation of space-charges at surfaces and grain boundaries in ionic compounds also arises from the segregation of native defects or solutes.<sup>14-16</sup> While the high bulk defect concentration of lithium intercalation compounds implies a very compact space-charge layer, changes in composition at the surface or the “core” of the grain boundary nonetheless will contribute to deviations in overall composition or nonstoichiometry if there is preferential segregation of solutes or defects.

These and other effects occurring in nanoscale intercalation compounds may be measurable through a combination of structural and electrochemical methods. We expected internal stress to be a function of the state-of-charge and time, possibly resulting in measurable changes in the lithium chemical potential. To explore this we measured the time- and state-of-charge dependence of the open-circuit voltage (OCV, vs. Li/Li<sup>+</sup>), and the corresponding crystal lattice parameters in electrochemically cycled olivines. Nanoscale (defined as <100 nm primary particle size) Li<sub>1-x</sub>FePO<sub>4</sub> is compared with a coarser-grained LiFePO<sub>4</sub> that serves as an example of the conventional two-phase

reaction. The electrochemically-induced transformation in  $\text{Li}_{1-x}\text{MnPO}_4$  is examined as well. We find support for the coherency stress effect where each crystalline phase affects the structure and composition of the other. However, we also identify an additional response, which is the formation of a co-existing amorphous state upon cycling materials of nano size scale. This tendency to disorder appears to be greater for  $\text{Li}_{1-x}\text{MnPO}_4$  than for  $\text{Li}_{1-x}\text{FePO}_4$ . These phenomena are interpreted from the elastic misfit between co-existing phases and the effect of surface energetics on nanoscale phase stability.

## **Experimental Section**

### **Test Materials**

Model nanoscale materials of undoped  $\text{LiMPO}_4$  compositions were selected for comparison. For examination of the lithium iron phosphate system we compared in detail two triphylite samples from a previous study representing the limiting cases of a “conventional” material and a nanoscale sample showing significant contraction of the miscibility gap.<sup>7</sup> Transmission electron microscopy (TEM) images and specific capacity vs. C-rate tests of the samples studied are shown in Figure 5-1.

The nanoscale sample (sample A) has a specific surface area measured by the BET method (Brunauer, Emmett and Teller) of  $48.8 \text{ m}^2/\text{g}$ , corresponding to an equivalent spherical particle diameter of 34 nm, and was synthesized as described in ref 17. In brief,  $\text{Li}_2\text{CO}_3$ ,  $\text{FeC}_2\text{O}_4 \cdot \text{H}_2\text{O}$  (or  $\text{MnCO}_3$ ), and  $\text{NH}_2\text{H}_2\text{PO}_4$ , each assayed by the manufacturer or by us in order to determine the true metals content, were weighed in an Ar-filled glovebox (<3ppm oxygen and water), then mixed by ball-milling in acetone for 24 h using zirconia milling media. The powder was dried and calcined at  $350^\circ\text{C}$  for 10 h in flowing Argon, then at  $600^\circ\text{C}$  in flowing Argon for 5 h. The crystallite size in sample A as derived from X-ray line broadening (Scherrer formula) was 32 nm, in good agreement with the measured specific surface area as well as the TEM images. The TEM results also show that the powder particles are equiaxed in shape, exhibiting no apparent faceting on any particular crystal plane. Sample A showed the smallest miscibility gap (largest mutual solid-solubility) between the triphylite and heterosite phases in the previous study

of undoped  $\text{Li}_{1-x}\text{FePO}_4$ , based on both X-ray measurements of lattice constants (Vegard's law) as well as electrochemical titration tests.<sup>7</sup> Sample C is a commercially purchased "carbon-added"  $\text{LiFePO}_4$  (Aldrich Chemical) having  $14.8 \text{ m}^2/\text{g}$  specific surface area and 113 nm equivalent spherical particle diameter. TEM showed that this material had a broader particle size distribution than sample A as well as a clearly observable carbon phase. The specific discharge capacity vs. C-rate performance of samples A and C are shown in Figure 5-1. A lithium manganese phosphate (lithiophilite) sample, sample M, was also examined in this study; this material was also made by the method of ref 17 and had a specific surface area of  $22.2 \text{ m}^2/\text{g}$  corresponding to an equivalent spherical diameter of 78 nm, consistent with the TEM imaging of this sample in Figure 5-1C.

### **Electrochemical Tests**

Electrochemical tests were performed using electrodes formulated with 79 wt% positive active material, 10 wt% conductive carbon black (Super P™, M.M.M. Carbon, Brussels, Belgium) and 11 wt% Kynar 2801 binder, using acetone as the solvent. The formulation was coated onto aluminum foil current collectors at a loading of  $\sim 5 \text{ mg}/\text{cm}^2$  of active material, and assembled in Swagelok™ type cells using Li metal foil as the counterelectrode, a microporous polymer (Celgard 2400™, Hoechst Celanese Corporation, Charlotte, NC, USA), and liquid electrolyte mixtures containing 1:1 by mole ethylene carbonate: dimethyl carbonate (EC:DMC) or ethylene carbonate: diethyl carbonate (EC:DEC), and 1 M  $\text{LiPF}_6$  as the conductive salt. Arbin or Maccor instrumentation was used for the galvanostatic and potentiostatic tests.

For X-ray diffraction structural analysis of the electrochemically transformed materials, freshly assembled Swagelok™ cells were first galvanostatically cycled through two complete cycles. This was done at a C/10 rate at room temperature for samples A and C, from which the specific capacity of the material was established. Then, each cell was charged at the same rate to a percentage of the C/10 capacity corresponding to a desired state-of-charge (SOC). Thus the SOC is here defined with respect to the practical capacity measured at the experimental voltage limits, rather than the theoretical capacity. Sample M was galvanostatically cycled at C/50 rate at 50°C (due to its slower kinetics at

room temperature), following which it was charged at the same rate to a desired SOC. A freshly assembled cell was used for each measurement of OCV or structure in order to avoid accumulating any history-dependent effects. Over the course of this study over 100 cells were constructed and tested. For the lithium iron phosphate samples the cycling voltage limits were 2.0-4.2V while for the lithium manganese phosphate it was 2.0-4.5V.

To measure the equilibrium OCV as a function of the SOC, cells were galvanostatically charged or discharged to the desired SOC, and then the OCV was allowed to relax for 200h, after which the rate of voltage decay,  $dV/dt$ , was less than  $10^{-7}$  V/h. These measurements were carried out with the cells being held in a temperature-controlled oven at  $22^{\circ}\text{C} \pm 0.2^{\circ}\text{C}$ . The voltage was measured to 0.1 mV resolution. The average OCV measured at 1h intervals over the last 20h was used as the equilibrium or “fully relaxed” electrical potential.

### **Structural Analysis**

For measurement of structure by X-ray diffraction as a function of the SOC, cells were galvanostatically charged or discharged to a desired SOC, then immediately disassembled in an argon-filled glovebox. The positive electrodes of sample C were mounted on an aluminum sample holder for X-ray diffraction. X-ray patterns were obtained using a Rigaku RTP500RC instrument with a rotating anode and  $\text{Cu-K}_{\alpha}$  radiation, at a slow scan rate of  $0.18^{\circ}/\text{min}$  over a  $2\theta$  range from  $15$  to  $135^{\circ}$ . For nanocrystalline samples A and M, the delithiated phases were found to be very sensitive to air exposure, exhibiting an exposure-related loss of crystallinity that may be due to reaction with air-borne water. In order to exclude such effects, XRD spectra were obtained using sample holder designed by the manufacturer for air-sensitive samples, which we sealed using 2 layers of 7.5 micron thick Kapton™ tape. These samples were characterized using  $\text{Cu-K}_{\alpha}$  x-rays and the PANalytical X'Pert PRO XRD system using a slow scan rate of  $0.15^{\circ}/\text{min}$  over a  $2\theta$  range from  $15$  to  $135^{\circ}$ . Control experiments were conducted which showed that the cycled samples did not change over the time scale of the measurements. The structural parameters of all X-ray data were refined by Rietveld analysis using PANalytical X'Pert HighScore Plus software and the backgrounds were manually fitted. Note that the

backgrounds for the electrodes will include contributions from the binder, electrolyte, and possibly side reaction products. As a result, the appearance of amorphous phases upon cycling of the active materials can be difficult to detect. We instead used crystalline phase fractions quantified by careful Rietveld refinement of high quality X-ray spectra obtained in slow scan experiments carried out at various SOC. For the spectra obtained from sample C, the best estimate residual parameter ( $R_{\text{exp}}$ ) and weighted residual profile error parameter ( $R_{\text{wp}}$ ) values were less than 2.0 and 7.0%, respectively, indicating excellent data quality and reliable refinements. For the spectra obtained from sample A, the background profiles also included contributions from the Kapton<sup>TM</sup> tape and therefore the signal to noise was slightly worse. Nonetheless,  $R_{\text{exp}}$  and  $R_{\text{wp}}$  for sample A were still less than 3.0 and 12.0%, respectively, again indicating high data quality and reliable refinements. Crystalline size and micro-strain were determined using the Williamson-Hall analysis and NIST silicon 640c was used as an external standard.

## **Results and Discussion**

### **Time- and State-of-Charge Dependence of OCV**

In the conventional view of intercalation compounds undergoing a two-phase reaction, the lithium chemical potential is pinned at a constant value (at constant temperature and pressure) as required by the Gibbs phase rule, and the positive electrode potential relative to  $\text{Li}/\text{Li}^+$  should theoretically be constant across the two-phase coexistence field. This was found not to be true in the present materials when the OCV is examined at a sub-millivolt scale of resolution. For sample A, panels A and B in Figure 5-2 show the time dependence of OCV after charging and discharging, respectively, to various SOC (or state-of-discharge, SOD) between 20 and 80%. There is a clear relaxation of the OCV that takes place over tens of hours. This is remarkable given that sample A can be effectively cycled at rates  $>10\text{C}$  (Figure 5-1), which corresponds to roughly a  $1 \times 10^4$  shorter time constant and suggests that the phase assemblage produced by electrochemical cycling is metastable. This phase assemblage nonetheless clearly has high lithium exchange rate. It is also seen that the OCV is not in fact constant with composition but increases with SOC in sample A. For sample C, the OCV relaxation

during charging to various SOC is shown in Figure 5-2C. Here also, a relaxation of the OCV over 20-40 h as well as an SOC dependence is observed. However, the relaxation occurs faster for sample C, the variation of OCV with SOD is weaker, and has opposite sign to that in sample A.

To compare the composition range over which the OCV varies with the phase diagram of the respective materials, we plot in Figure 5-3A the temperature-dependent miscibility data for samples A and C from ref. 7, as well as the equilibrium phase diagram of Dodd et al.<sup>6</sup> for bulk  $\text{Li}_{1-x}\text{FePO}_4$ . The dramatic shrinking of the miscibility gap at nanoscale particle size is clearly seen here.

The terminal (fully-relaxed) OCV for sample A at room temperature is shown as a function of SOC in Figure 5-3B. Results for both charge and discharge are shown, and galvanostatic curves for the same material measured upon charge and discharge at a C/50 rate are also plotted for comparison. The SOC range of 30 to 75% lies within the room temperature miscibility gap. The OCV measured upon both charge and discharge shows a slight increase with increasing SOC within the miscibility gap. There is also a hysteresis in the OCV between charge and discharge of about 7 mV. The variations in OCV seen here is much greater than can be accounted for by temperature variation during the experiment. For comparison, in Ref. 7 we measured the OCV of sample A at 50% SOC and temperatures ranging from  $-20^\circ\text{C}$  to  $+45^\circ\text{C}$ , and found it to vary by 3mV over this temperature range. The variation in OCV with SOC of sample A, shown in Fig. 5-3B, is  $\sim 10$  mV despite temperature being constant to  $\pm 0.2^\circ\text{C}$ . Thus the OCV variation cannot be attributed to temperature variation. Figure 5-3C shows the relaxed OCV and the C/50 galvanostatic curve for sample C compared to those for sample A. The wider SOC range over which the OCV is shown corresponds to the wider miscibility gap (Figure 5-3A). However, sample C also shows a measurable variation of OCV with SOC. Interestingly, it has the opposite slope, with the OCV decreases with increasing SOC. Furthermore, within its miscibility gap, sample C has a lower OCV by between 5 and 10 mV than sample A, which at room temperature corresponds to a difference in lithium chemical potential of 500-1000 J/mole. Clearly, the co-existing phase

assemblages and/or compositions are not identical in samples A and C during electrochemical cycling.

### **State-of-Charge Dependence of “Triphylite” and “Heterosite” Phase Fractions**

We next compare the evolution of the lithium-rich (“triphylite”) and lithium-poor (“heterosite”) phase fractions as a function of SOC in samples A and C, as determined by Rietveld refinement of the X-ray diffraction spectra. The compositions of both phases can be nonideal; consistent with previous notation<sup>7,8</sup> we will use  $\text{Li}_{1-x}\text{FePO}_4$  to denote the lithium-rich endmember having a lithium deficiency  $x$  with respect to its ideal composition (e.g., triphylite or lithiophilite) and  $\text{Li}_y\text{FePO}_4$  to denote the lithium-poor endmember having a lithium excess  $y$  with respect to its ideal composition (e.g., heterosite or purpurite). The evolution of phase fractions in sample C followed nearly ideal two-phase behavior. Figure 5-4A shows a sequence of X-ray diffraction spectra taken as a function of SOC from starting material through 95% SOC. The systematic variation in intensity of the heterosite (200), (201), and (301) peaks (labeled “H”) relative to the same peaks for triphylite (labeled “T”) with SOC is clearly seen. “C” refers to the (002) peak of graphite, resulting from the carbon additive used in the electrode formulation. Even at 5 and 95% SOC, the minority phases heterosite and triphylite respectively were readily detected. Figure 4B shows the evolution of the triphylite and heterosite phase fractions between 5 and 95% SOC, obtained by Rietveld-refinement of X-ray spectra taken after 200h relaxation time. They vary linearly with SOC, as expected from the ideal two-phase model. The unit cell volumes determined from Rietveld refinement of the triphylite and heterosite structure as a function of SOC are also shown in Figure 5-4B. Note that the triphylite unit cell volume remains essentially constant across the entire SOC range; there is no evidence for induced nonstoichiometry  $x$  upon formation of the heterosite phase. However, the heterosite unit cell volume is measurably higher when the phase is first nucleated, then decreases with increasing SOC. We attribute this behavior to size and strain effects. Since the initially nucleated  $\text{Li}_y\text{FePO}_4$  will have finer length scale and/or different morphology than the triphylite phase, it may be expected to have higher lithium nonstoichiometry  $y$  if, for example, coherency stresses are initially present between the parent triphylite and nucleated heterosite phase. As the

heterosite fraction grows, the evolution of unit cell volumes shows that both phases become “fully-relaxed” and approach limiting values consistent with previous literature data for these two compounds as bulk phases. The microstrain obtained from Rietveld refinement was consistent with this interpretation, with the triphylite phase having ~0.05% strain across the SOC range while the heterosite phase had an initially higher microstrain of 0.15% when first measured at 5% SOC, declining to 0.09% by 50% SOC and remaining at that value to 95% SOC. The difference in unit cell volume approaches 6.6%, which is typical of coarse-grained  $\text{Li}_{1-x}\text{FePO}_4$ .<sup>7,8</sup>

In Figure 5-4C, we compare the normalized mole fractions of triphylite and heterosite with the C/50 galvanostatic voltage curve for sample C. The deviations in voltage at the very beginning and end of charge corresponding to the formation of heterosite and disappearance of triphylite are seen. With the exception of the deviation in unit cell volume when the heterosite phase first forms, sample C behaves in a manner completely consistent with the conventional two-phase reaction viewpoint. The slight decrease in OCV as the heterosite unit cell volume relaxes to its bulk value indicates that the Li chemical potential is actually slightly higher (OCV lower) when both phases are fully relaxed.

Figure 5-5 shows that the phase-evolution behavior is markedly different for the nanocrystalline material, sample A. X-ray diffraction spectra for this sample as a function of SOC from starting material through 100% SOC are shown in Figure 5-5A. Here, 100% SOC corresponds to the extraction of lithium from a fully lithiated (discharged) material to a specific capacity of  $155 \text{ mA h g}^{-1}$ . The higher background is due to the Kapton™ tape used to hermetically seal the sample holder.

The normalized phase fractions of  $\text{Li}_{1-x}\text{FePO}_4$  and  $\text{Li}_y\text{FePO}_4$ , these being the only detectable crystalline phases aside from the carbon additive, are shown in Figure 5-5B as a function of SOC, along with their unit cell volumes. The nonstoichiometry parameters  $x$  and  $y$  calculated from Vegard’s law are also given next to each unit cell volume datum. The triphylite  $\text{Li}_{1-x}\text{FePO}_4$  unit cell volume decreases monotonically with increasing SOC even at compositions within the miscibility gap where two crystalline phases are present.



The decreasing unit cell volume corresponds to increasing lithium deficiency  $x$  in the  $\text{Li}_{1-x}\text{FePO}_4$  phase. Note that with increasing SOC, there is a small but sudden decrease in the unit-cell volume of  $\text{Li}_{1-x}\text{FePO}_4$  occurring concurrently with the first appearance of the heterosite  $\text{Li}_y\text{FePO}_4$  crystalline phase at  $\sim 30\%$  SOC. The initial  $\text{Li}_y\text{FePO}_4$  formed at 25-30% SOC also has slightly larger unit-cell volume, corresponding to larger lithium concentration ( $y \sim 0.139-0.146$ ) than it does at higher SOC values ( $y \sim 0.130-0.140$ ). At 100% SOC, the  $\text{Li}_y\text{FePO}_4$  unit cell volume reaches its minimum value, as expected. The difference in unit-cell volume at intermediate SOC values when both phases coexist is about 5.2%, significantly lower than for the coarse-grained sample C. The microstrain obtained from Rietveld refinement was significantly higher across the entire SOC range than for sample C, consistent with the presence of coherency stresses.<sup>8</sup> The microstrain in the  $\text{Li}_{1-x}\text{FePO}_4$  phase was in the range of 0.2 to 0.3%, while that in the  $\text{Li}_y\text{FePO}_4$  phase varied from 0.2 to 0.5%.

At the beginning and end of charge when only a single phase exists, we expect the unit cell volume to vary continuously due to the existence of a single phase field. Judging from the SOC values at which the minor phase is first detected by XRD in Figure 5-5, the solid solution fields extend to  $x \sim 0.25$  and  $y \sim 0.2$ , respectively, which are larger values than are observed for the same sample after charging to 50% SOC and allowing a long period of rest.<sup>7</sup> Within the miscibility gap, however, the present data indicate a significant new result: even in two phase coexistence, the compositions evolve continuously. This is completely consistent with the results above (Figure 5-3) showing that the OCV varies with SOC continuously within the two-phase field. The initial decrease in  $\text{Li}_{1-x}\text{FePO}_4$  unit-cell volume when  $\text{Li}_y\text{FePO}_4$  nucleates, the continuous variation over the SOC range where they coexist, and the smaller difference in unit-cell volume when both phases coexist as compared to sample C, are all consistent with the coherency stress model<sup>7,8</sup> in which the mechanical constraint imposed by each phase upon the other causes their respective lattice constants (and lithium concentrations) to approach one another due to Vegard's stresses. Thus in sample A, the compositions of the crystalline fractions behave as we have described previously.<sup>7</sup>

However, further anomalous behavior becomes evident when the phase fractions are quantified. In Figure 5-5C, the crystalline phase fractions and the C/50 galvanostatic charge curve for sample A are shown as a function of SOC. The boundaries of the miscibility gap at this temperature are drawn as broad vertical lines, encompassing the range of numerical values determined from PITT measurements and Vegard's law.<sup>7</sup> The phase fractions shown are the Rietveld-refined results for the two crystalline phases. It is seen that the variation of phase fraction with SOC is nonlinear, namely in violation of the lever rule for co-existence of two phases within a fixed immiscibility field. Specifically, there is a deficiency of  $\text{Li}_y\text{FePO}_4$  relative to that expected from the lever rule below 60-65% SOC, and an excess above. The converse is true for the crystalline  $\text{Li}_y\text{FePO}_4$  phase, the behavior of which is furthermore anomalous in that it is not detected until the sample reaches 25% SOC, a composition that is well within the crystalline miscibility gap determined in the previous study.<sup>7</sup> (In contrast, this phase was clearly detectable in sample C at 5% SOC, Figure 5-4.) The triphylite  $\text{Li}_{1-x}\text{FePO}_4$  phase also disappears by 80% SOC, before the Li-rich phase boundary is reached.

### **Additional Amorphous or Disordered Phases**

Using the graphite (002) peak from the carbon additive as a qualitative internal standard (Figures 5-4A and 5-5A), we had noted that the integrated intensity of the crystalline phase peaks in sample A appeared to be much lower than that in sample C. Given the nearly identical specific capacities of the two samples at C/5 rate (Figure 5-1), this alone suggested a substantial noncrystalline fraction in sample A. TEM analysis of the samples indeed showed the presence of amorphous particles, but we could not rule out the possibility that these formed upon exposure to air. However, quantification of the amount of amorphous or disordered phase was possible because we had experimental measurements of three independent quantities: 1) the crystalline phase compositions, via the unit cell volumes; 2) the crystalline phase fractions from Rietveld refinement of the diffraction data, and 3) the overall Li concentration from electrochemical cycling. One may then apply mass balance relationships to determine the amount or concentration of the noncrystalline phases. The simplest such relationship assumes a single amorphous

phase  $\alpha$ - $\text{Li}_2\text{FePO}_4$  co-existing with the two observed crystalline phases. At a given state of charge where the overall composition is  $\text{Li}_\beta\text{FePO}_4$ , mass balance requires that:

$$a\text{Li}_{1-x}\text{FePO}_4 + b\text{Li}_y\text{FePO}_4 + c\alpha\text{-Li}_2\text{FePO}_4 = \text{Li}_\beta\text{FePO}_4 \quad (1)$$

where  $a$ ,  $b$ , and  $c$  are the molar fractions of each respective phase ( $a + b + c = 1$ ), and lithium mass balance is given by  $(1-x)a + yb + zc = \beta$ . We currently do not know  $z$  and  $c$  independently but can place bounds on the product  $zc$ . For example, taking  $(1-x)=0.91$  and  $y=0.14$ , representing the results in Figure 5-5 at 50% SOC (with the ratio of  $\text{Li}_{0.91}\text{FePO}_4$  phase to  $\text{Li}_{0.14}\text{FePO}_4$  phase of  $\sim 2:1$ ) if the amorphous phase is assumed to be completely delithiated ( $z=0$ ), then at 50% SOC there is 51 mole% of  $\text{Li}_{0.91}\text{FePO}_4$ , 26 mole% of  $\text{Li}_{0.14}\text{FePO}_4$ , and 23 mole% of the amorphous phase  $\alpha$ - $\text{FePO}_4$ . This is a substantial fraction of amorphous phase. If the amorphous phase is assumed to be partially lithiated, then its molar percentage will be even higher than this limiting value. For example, if the amorphous phase is assumed to have composition  $\text{Li}_{0.2}\text{FePO}_4$ , then at 50% SOC we have 44 mole% of  $\text{Li}_{0.91}\text{FePO}_4$ , 22 mole% of  $\text{Li}_{0.14}\text{FePO}_4$ , and 34% of the amorphous phase  $\alpha$ - $\text{Li}_{0.2}\text{FePO}_4$ .

The curves for the crystalline phase fractions vs. SOC in Figure 5-5 have a sigmoidal shape, crossing the straight lines that define the two-phase lever rule at between 60% and 65% SOC. This means that only in this narrow range of composition is it possible to explain the overall composition  $\beta$  from a mixture of the two crystalline phases alone. (Co-existence of an amorphous phase is not ruled out, however.) Below this SOC, there is a deficiency of the delithiated phase  $\text{Li}_y\text{FePO}_4$ , and mass balance requires the presence of an additional noncrystalline delithiated phase. Above this SOC, there is a deficiency of the lithiated phase  $\text{Li}_{1-x}\text{FePO}_4$ , and the noncrystalline phase must be substantially lithiated to satisfy mass balance. It is unlikely that there is such a complex evolution where at low SOC there is first a delithiated amorphous phase, then no amorphous phase at 60-65% SOC, and finally a lithiated amorphous phase at higher SOC. Instead, we believe that an amorphous phase is present throughout, in which the lithium concentration  $z$  increases systematically with SOC. The amount of noncrystalline phase required to satisfy mass balance is in general well beyond that which can be provided by

a surface atomic layer alone, given the surface to volume ratio of these powders. Thus we do not believe the results can be explained by surface enrichment or depletion of lithium at sites having a different chemical potential than the bulk, although the amorphous phase may well form as a surface coating, as discussed later. Detailed knowledge of the amorphous phase composition will allow a more precise estimate of the phase fractions. It is also possible that more than one noncrystalline phase is present.

### **Phase Transformation upon Cycling of Nano-Li<sub>1-x</sub>MnPO<sub>4</sub>**

Experiments were also conducted on LiMnPO<sub>4</sub>, sample M, in which we expected an even greater tendency towards amorphization for reasons discussed later. Figure 5-6 shows X-ray patterns from the sample in its starting state, and after charging to 40% SOC at C/50 rate and 50°C. The sample was first given two complete cycles under these conditions. “L” and “P” in Figure 5-6 refer to lithiophilite and purpurite, the lithium-rich and lithium-poor endmembers of this system, respectively. “C” again refers to the (002) peak of graphite, resulting from the carbon additive used in the electrode formulation. It can be seen that the peaks for the delithiated Li<sub>y</sub>MnPO<sub>4</sub> phase after charging are extremely broad, indicating that the newly formed phase is highly disordered if not amorphous.

### **General Discussion**

The observed behavior of these crystalline olivines at nanoscale particle sizes bears similarities to several other surface and nanoscale phenomena in which a disordered noncrystalline phase, despite having higher volume free energy, is stabilized under the influence of surface energy, mechanical stress, or other short-range interactions. In surface premelting, which is best known for ice<sup>18-20</sup> but also occurs in certain elemental metals,<sup>21</sup> the surface of a crystal begins to melt below the bulk melting point (by ~2K for ice) due to the lower surface energy of the liquid compared to the crystal. The premelted layer is constrained in its thickness by the increase in volumetric energy upon thickening as well as by dispersion interactions across the nanometer-thick film. Similar effects cause melting point suppression in nanocrystalline metals.<sup>22, 23</sup> The surface-energy-stabilized disordered phase may be a glass rather than a liquid. In binary oxides,

nanometer-thick solid amorphous films of compositions that do not appear in the bulk phase diagram are stabilized on crystalline oxide surfaces for similar reasons.<sup>24-26</sup> These films also take on nanometer-scale thickness, as they are prevented from thickening further by their higher volume free energy compared to the crystal. Intergranular amorphous films of similar character have been widely reported; note that these are not “wetting” liquids in the conventional sense but disordered solid films that form to minimize interfacial energy.<sup>27-29</sup> Thus a nanoparticle system which has a lower surface energy for its glass than the corresponding crystal should become amorphous with decreasing size (increasing surface to volume ratio), first at the surface of the particle and eventually stabilizing the entire particle in the glassy state. This phase conversion has been shown in nanocrystalline zirconia,<sup>30</sup> where high-temperature oxide melt solution calorimetric measurements confirm the existence of a phase stability crossover from the bulk-stable monoclinic phase to metastable tetragonal and then amorphous phases with increasing specific particle surface area.

The present metal phosphates do appear to readily form disordered solids. Like other “III-V” analogs to SiO<sub>2</sub> such as AlPO<sub>4</sub>,<sup>31,32</sup> FePO<sub>4</sub> is stable at atmospheric pressure in the quartz structure<sup>33</sup> but is a good glass-former. Iron phosphate glasses are readily made by quenching from the melt,<sup>34</sup> and amorphous anhydrous FePO<sub>4</sub> is readily formed by heating of FePO<sub>4</sub> · nH<sub>2</sub>O, retaining an amorphous structure until about 500°C.<sup>35-38</sup> The latter can also be chemically lithiated without crystallization.<sup>37</sup> Thus the volume free energy difference between the glassy and crystalline form of FePO<sub>4</sub> appears to be relatively small. MnPO<sub>4</sub> is less well studied but should behave similarly. As with SiO<sub>2</sub>, a glass structure that is in general a continuous-random-network consisting of corner-linked oxygen tetrahedra<sup>38</sup> alternatively filled with Fe<sup>3+</sup> (or Mn<sup>3+</sup>) and P<sup>5+</sup> seems likely. Upon lithiation, the present experimental data as well as ref 37 indicate retention of the glassy structure, which may correspond to Li<sup>+</sup> in interstitial positions like those occupied by alkali ions in common alkali-modified silicates,<sup>40</sup> charge-compensation being provided by the Fe<sup>3+</sup> in tetrahedral coordination. However, the disordered structures of melt-quenched, dehydrated, and electrochemically transformed disordered structures (the present case) may differ significantly in the details of their short-range order. In AlPO<sub>4</sub>,

what was thought to be a simple crystal-to-glass transition under high pressure was later shown to be, first, a transition to a disordered crystalline phase with short-range order, prior to true amorphization at higher pressures.<sup>31</sup> The electrochemically-driven crystal-to-amorphous transition in the present materials may also have complex behavior.

Glassy FePO<sub>4</sub> and MnPO<sub>4</sub> should be structurally similar in local coordination to their quartz isomorphs in the same way that amorphous SiO<sub>2</sub> is similar to quartz. If so they should have generally lower surface energy than their crystalline counterparts. Parks<sup>41</sup> compared the interfacial energies of quartz and amorphous silica based on their solubilities in aqueous solutions (Gibbs-Thomson effect), and found a difference of ~0.3 J/m<sup>2</sup>. For the free surfaces, an even larger difference is implied if the dehydroxylation energy is included. The surface energy of liquid SiO<sub>2</sub> extrapolated from high temperature data to room temperature is ~0.3 J/m<sup>2</sup>,<sup>41</sup> whereas the fracture surface energy of quartz ranges from ~0.4 J/m<sup>2</sup> (for (10 $\bar{1}$ 1) and ( $\bar{1}$ 011) orientations) to ~1 J/m<sup>2</sup> ((10 $\bar{1}$ 0) and (11 $\bar{2}$ 0) orientations). Because of the isotropic shape of the present particles (Fig. 5-1) the relevant comparison is between the amorphous glass surface and an orientational average of crystalline surface energies, which in the case of SiO<sub>2</sub> is a difference of at least 0.3 J/m<sup>2</sup>.

The avoidance of coherency stresses<sup>8</sup> is another factor that will promote amorphization. Consider a crystalline particle that is undergoing delithiation, and for which substantial crystalline misfit stresses must be accommodated if it is to transform according to the conventional two-phase reaction model. The particle may: (1) form an incoherent interface between the Li<sub>1-x</sub>MPO<sub>4</sub> and Li<sub>y</sub>MPO<sub>4</sub> phases, and accept a higher interfacial energy as the penalty for relieving lattice strain energy; (2) form a coherent interface of lower energy, and accommodate the misfit as lattice strain and corresponding deviations in the co-existing phase compositions; or (3) simultaneously relieve the interfacial energy by forming a crystal-glass interface, and the volume strains by forming the amorphous phase. Between the present work and previous publications,<sup>7-8</sup> we have evidence for each mode of behavior occurring depending on the specific material in question. LiMnPO<sub>4</sub> is clearly more prone to amorphization upon delithiation than LiFePO<sub>4</sub>. While a complete understanding of the differences between these two compounds requires additional data

on the volumetric and surface energies involved, a contributing factor may be the much larger crystalline misfit in the  $\text{LiMnPO}_4\text{-MnPO}_4$  system, 11% difference in unit cell volume for the stoichiometric compositions.<sup>8</sup> In elemental silicon, which also adopts a continuous-random-network glassy structure,<sup>39</sup> the structural misfit between parent phase and lithiated intermetallic compounds is even larger than in the present materials; and a previous study has shown that lithiation of crystalline Si results in solid-state-amorphization as well.<sup>43</sup>

The several possible phase transformation pathways between lithiated and delithiated phases elucidated by the present work are illustrated in Figure 5-7. A coarse, single crystalline particle that is effectively isolated from any neighbors undergoes conventional nucleation and growth, with the multiphase particle having excess interfacial and strain energy in the partially transformed state (Figure 5-7A). In general, the morphology will not be of a “core-shell” configuration due to the influences of anisotropy in elastic constants, diffusion, or surface energy.<sup>8,44</sup> In a multiparticle assembly (Figure 5-7B), the same partially-transformed state may initially occur. This state, however, is metastable with respect to a two-phase mixture of single-phase particles in which coherency strain and interfacial energies are removed. Whether the endpoint in Figure 5-7B is reached depends on kinetics; for example the two-phase particles observed by Chen et al.<sup>44</sup> are clearly frozen in the partially transformed state. The metastability of a delithiated olivine with respect to amorphization is illustrated in parts C and D in Figure 5-7, respectively. The additional coherency strain and interfacial energy of the partially transformed state may be relieved by forming an amorphous surface phase or grain boundary phase between particles within an aggregate (Figure 5-7C). This can simultaneously lower the surface and strain energies, although it comes with an increase in volume free energy due to the formation of the amorphous phase. Further delithiation may result in complete amorphization. (Another configuration not shown in Figure 5-7 would have an amorphous film separating the crystals in order to relieve volume strain energy; this is analogous to the amorphous grain boundary and heterointerfacial films<sup>27-29</sup> and may have been observed by Chen et al.<sup>44</sup>) Finally, for small enough particles, complete transformation to the amorphous state may occur even at partial delithiation if the

reduction of surface and strain energy is more than the increase in volume free energy (Figure 5-7D).

Each of these transformation pathways has specific implications for electrochemical performance in a practical battery system. One is that the often-cited limitation in crystalline olivines of “one-dimensional diffusion” (along the [010] lithium channel direction) may be moot, if lithium transport occurs primarily in an amorphous phase that is structurally isotropic. Another is that the relevant surface for any considerations of the influence of surface defects on electrochemical potential may be the amorphous rather than crystalline surface. Perhaps most importantly, the electrochemical response of olivines undergoing the complex phase transitions shown here is expected to be sample history dependent, and inherently hysteretic. For example, the recent observation of single phase particles in partially charged  $\text{LiFePO}_4$  by Delmas,<sup>45</sup> which are in conflict with the observation of multiphase phase particles by Chen et al.,<sup>44</sup> may reflect differences in the extent of phase redistribution following delithiation (such as Figure 5-7A vs. 7B). And an example of hysteretic response is that the OCV values upon charge and upon discharge to the same lithium composition may not ever converge (Figure 5-3). Tuning nanoscale olivines to take advantage of disorder while minimizing possible detrimental effects, may be a fruitful approach to improve materials.

To identify the actual transformation path(s) for nano- $\text{Li}_x\text{MPO}_4$ , concurrent efforts in experimental and theoretical development are necessary. Among various modeling methods at different length and time scales, continuum-level models are promising to reveal general trends in phase transformation pathways of  $\text{Li}_x\text{MPO}_4$  particles during delithiation/lithiation. For example, Johnson<sup>46</sup> considers spinodal decomposition confined in spherical particles in a generalized diffuse-interface (phase-field) model. Model calculations show that the solubility limits of the phase-separating phases increase with decreasing particle size, which may account for the observed size-dependence of miscibility gap in the  $\text{Li}_{1-x}\text{FePO}_4/\text{Li}_y\text{FePO}_4$  nanometer-scale particles. We recently applied a phase-field model<sup>47,48</sup> that treats spatial variation of structural order (“crystallinity”) in polycrystalline materials to predict the formation of intergranular amorphous films in ceramics and metallic alloys.<sup>49,50</sup> Based on this work, a modified



model, which is specific to  $\text{Li}_x\text{MPO}_4$  systems and incorporates the surface and stress effects on phase stability, is being developed to explain the experimental observations.<sup>51</sup>

## Summary and Conclusions

A comparative study of the structural and phase changes taking place during electrochemical cycling of nanoscale ( $< 100$  nm) and conventional  $\text{Li}_{1-x}\text{MPO}_4$  has been conducted. By measuring the state-of charge dependence and time dependence of the open-circuit voltage and the co-existing phase content, it is shown that the phase transformation path differs significantly between the two types of materials. Coarse-grained  $\text{LiFePO}_4$  (113 nm) is shown to undergo a conventional two-phase reaction in which crystalline  $\text{LiFePO}_4$  and  $\text{FePO}_4$  are the predominant co-existing phases. In nanoscale samples, we observe that co-existing crystalline phases have greater mutual solubility for lithium (reduced miscibility gap), and find that the appearance of each phase constrains the unit cell parameters of the other in a manner consistent with coherency stress effects. In addition, it is shown that the compositions of the crystalline phases are not constant within the miscibility gap as expected for simple two-phase co-existence, and that at least one disordered phase is simultaneously present. Thus the phase transformation path in nanoscale olivines during electrochemical cycling can be much more complex than previously thought. The possible paths, and their implications for electrochemical performance in rechargeable battery systems, are discussed.

## References

1. Macilwain, C., *Nature*, **444**, 17 (2006).
2. Chu, A. Development of HEV batteries with lithium iron phosphate cathodes, presented at the Advanced Automotive Battery Conference, Baltimore, MD, June 2006.
3. [www.A123Systems.com](http://www.A123Systems.com)
4. Delacourt, C.; Laffont, L. ; Bouchet, R.; Wurm, C.; Leriche, J.B.; Morcrette, M.; Tarascon, J.M.; Masquelier, C.; *J. Electrochem. Soc.*, **152**, A913 (2005).

5. Yamada, A.; Takei, Y.; Koizumi, H.; Sonoyama, N.; Kanno, R.; Ito, K.; Yonemura, M.; Kamiyama, T. *Nat. Mater.*, **5**, 357 (2006).
6. Dodd, J.L.; Yazami, R.; and Fultz, B. *Electrochem. Solid-State Lett.*, **9**, A151 (2006).
7. Meethong, N.; Huang, H.S.; Carter, W.C.; and Chiang, Y.M. *Electrochem. Solid-State Lett.*, **10**(5), A134 (2007).
8. Meethong, N.; Huang, H.S.; Speakman, S.A.; Carter, W.C.; and Chiang, Y.M. *Adv. Funct. Mater.*, **17**(7), 1115 (2007).
9. Kao, Y.-H.; Meethong, N.; Tang, M.; Huang, H.-Y.; Carter, W. C.; Chiang, Y.-M. Abstract 14, International Meeting on Lithium Batteries – 14, Tianjin, China, June 22-27, 2008.
10. Wagemaker, M.; Borghols, W.J.H.; and Mulder, F.M. *J. Am. Chem. Soc.*, **129**, 4323 (2007).
11. Levi, M.D. and Aurbach, D. *J. Solid State Electrochem.*, **11**, 1031 (2007).
12. Terwilliger, C.D. and Chiang, Y.M. *J. Acta Metall. Mater.*, **43**(1), 319 (1995).
13. Chiang, Y.M.; Lavik, E.B.; Kosacki, I.; Tuller, H.L.; and Ying, J.Y. *Appl. Phys. Lett.*, **69**(2), 185 (1996), and *J. Electroceramics*, **1**, 7 (1997).
14. Kliever, K.L. and Koehler, J.S. *Phys. Rev. A*, **140**, 1226 (1965).
15. Yan, M.F.; Cannon, R.M.; Bowen, H.K. *J. Appl. Phys.*, **54**, 764 (1983).
16. Ikeda, J.A.S. and Chiang, Y.M. *J. Am. Ceram. Soc.*, **76**, 2437 (1993) and Ikeda, J.A.S.; Chiang, Y.M.; Garratt-Reed, A.J. and Vander Sande, J.B. *J. Am. Ceram. Soc.*, **76**, 2447 (1993).
17. Chung, S.-Y., Bloking, J.T. and Chiang, Y.-M. *Nature Materials*, **1**, 81 (2002).
18. Dash, J.G. *Contemp. Phys.*, **30**, 89 (1989).
19. Dash, J.G.; Fu, H. and Wettlaufer, J.S. *Rep. Prog. Phys.*, **58**, 115 (1995).
20. Dash, J.G.; Rempel, A.M. and Wettlaufer, J.S. *Rev. Mod. Phys.*, **78**, 695 (2006).
21. Frenken, J.W.M. and van der Veen, J.F. *Phys. Rev. Lett.*, **54**, 134 (1985).
22. Buffat, Ph.; and Borel, J.P. *Phys. Rev. A*, **13**(6), 2287 (1976).
23. Schebarchov, D. and Hendy, S.C. *Phys. Rev. Lett.*, **96**, 256101-1 (2006).
24. Luo, J. and Chiang, Y.-M. *Acta Mater.*, **48**, 4501 (2000).
25. Luo, J.; Chiang, Y.-M.; Cannon, R.M. *Langmuir*, **21**, 7358 (2005).

26. Luo, J. *Crit. Rev. Solid State Mater. Sci.*, **32**, 67 (2007).
27. Cannon, R. M.; Esposito, L. *Z. Metallkd.*, **90**, 1002 (1999).
28. Kleebe, H. -J.; Cinibulk, M. K.; Cannon, R. M.; Rühle, M., *J. Am. Ceram. Soc.*, **76**, 1969 (1993).
29. Clarke, D.R.; Shaw, T.M.; Philipse, A. P.; Horn, R.G. *J. Am. Ceram. Soc.*, **76**, 1201 (1993).
30. Pitcher, M. W.; Ushakov, S. V.; Navrotsky, A. et al. *J. Am. Ceram. Soc.*, **88**, 160 (2005).
31. Gillet, Ph.; Badro, J.; Varrel, B.; and McMillan, P.F. *Phys. Rev. B.*, **51**, 262 (1995).
32. Gutiérrez-Mora, F.; Goretta, K.C.; Singh, D.; Routbort, J.L.; Sambasivan, S.; Steiner, K.A.; Adabie, J.; and Rangan, K.K. *J. Eur. Ceram. Soc.*, **26**, 1179 (2006).
33. Aliouane, N.; Badechet, T.; Gagou, Y.; Nigrelli, E.; and Saint-Gregoire, P. *Ferroelectrics*, **241**, 255 (2000).
34. Friebele, E.J.; Wilson, L.K.; Dozier, A.K.; and Kinser, D.L. *Phys. Status Solidi A*, **45**, 323 (1971).
35. Hong, Y.S.; Ryu, K.Y.; Park, Y.J.; Kim, M.G.; Lee, J.M.; and Chang, S.H. *J. Mater. Chem.*, **12**, 1870 (2002).
36. Song, Y.; Yang, S.; Zavalij, P.Y.; and Whittingham, M.S. *Mater. Res. Bull.*, **37**, 1249 (2002).
37. Prosini, P.P.; Lisi, M.; Scaccia, S.; Carewska,; Cardellini, F.; and Pasqualib, M. *J. Electrochem. Soc.*, **149**(3), A297 (2002).
38. Okada, S.; Yamamoto, T.; Okazaki, Y.; Yamaki, J.; Tokunaga, M.; and Nishida, T. *J. Power Sources*, **146**, 570 (2005).
39. Zallen, R. Physics of Amorphous Solids **1983**, J. Wiley and Sons, NY.
40. Chiang, Y.-M.; Birnie, D.P., III; Kingery, W.D.; Physical Ceramics **1997**, John Wiley and Sons, New York.
41. Parks, G.A. *Reviews in Mineralogy*, **23**, 133 (1990).
42. Mazurin, O.V.; Streltsina, M.V.; Shvaiko-Shvaikovskaya, T.P. *Handbook of Glass Data, Part A*, **1983**, Elsevier, New York, 126.
43. Limthongkul, P.; Jang, Y.I.; Dudney, N.; and Chiang, Y.M. *Acta Mater.*, **51**, 1103 (2003).

44. Chen, G.; Song, X.; Richardson, T. *Electrochem. Solid-State Lett.*, **9**, A295 (2006).
45. Delmas, C.; Maccario, M.; Croguennec, L.; Wattiaux, A.; Le Cras, F.; and Weill, F. presented at the 212<sup>th</sup> *Electrochem. Soc. Mtg. Abs. #270*, Washington, DC, USA, **2007**.
46. Johnson,, W. C. *Acta Mater.*, **49**, 3463 (2001).
47. Kobayashi, R.; Warren, J. A.; Carter, W. C. *Physica D*, **140**, 141 (2000).
48. Warren, J. A.; Kobayashi, R.; Lobkovsky, A.; Carter, W. C. *Acta Mater.*, **51**, 6035 (2003).
49. Tang, M.; Carter, W. C.; Cannon, R. M. *Phys. Rev. B*, **73**, 024102 (2006).
50. Tang, M.; Carter, W. C.; Cannon, R. M. *Phys. Rev. Lett.*, **97**, 075502 (2006).
51. Tang, M.; Huang, H.-Y.; Meethong, N.; Kao, Y.-H.; Carter, W. C.; Chiang, Y.-M. *Mater. Res. Soc. Symp. Proc.*, **1100**, JJ03-04 (2008).

## Chapter 5 Figures and Tables

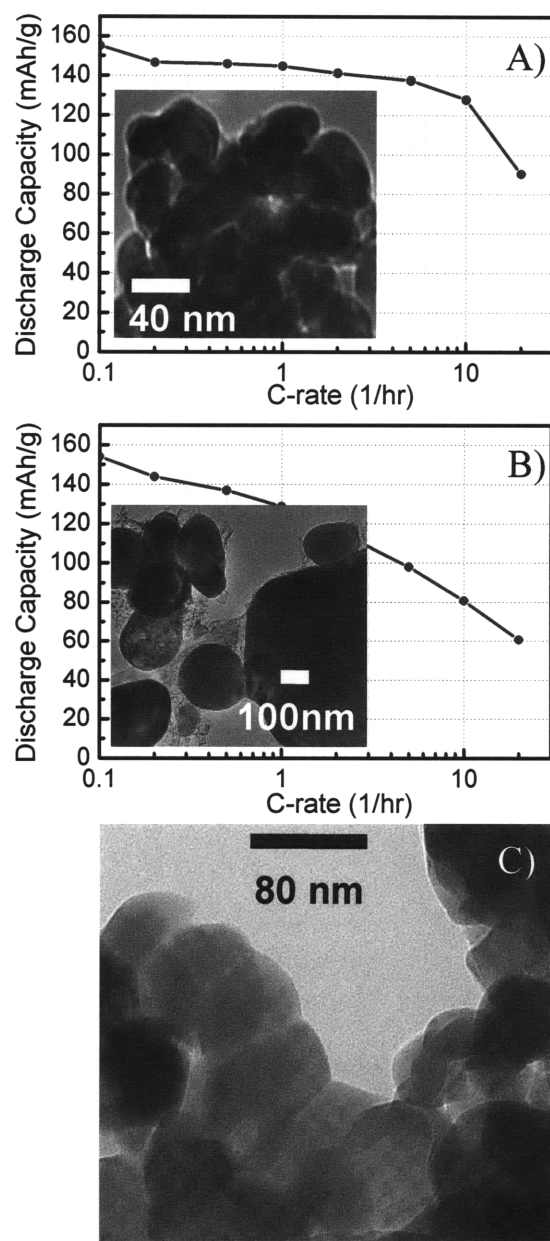


Figure 5-1: Three powders used in this study: (a) sample A,  $\text{Li}_{1-x}\text{FePO}_4$  having 34nm average particle size as determined from the BET specific surface area, (b) sample C,  $\text{LiFePO}_4$  having 113 nm average size, and (c) sample M,  $\text{Li}_{1-x}\text{MnPO}_4$  having 78 nm average particle size. The specific capacity vs. C-rate is shown for samples A and C.

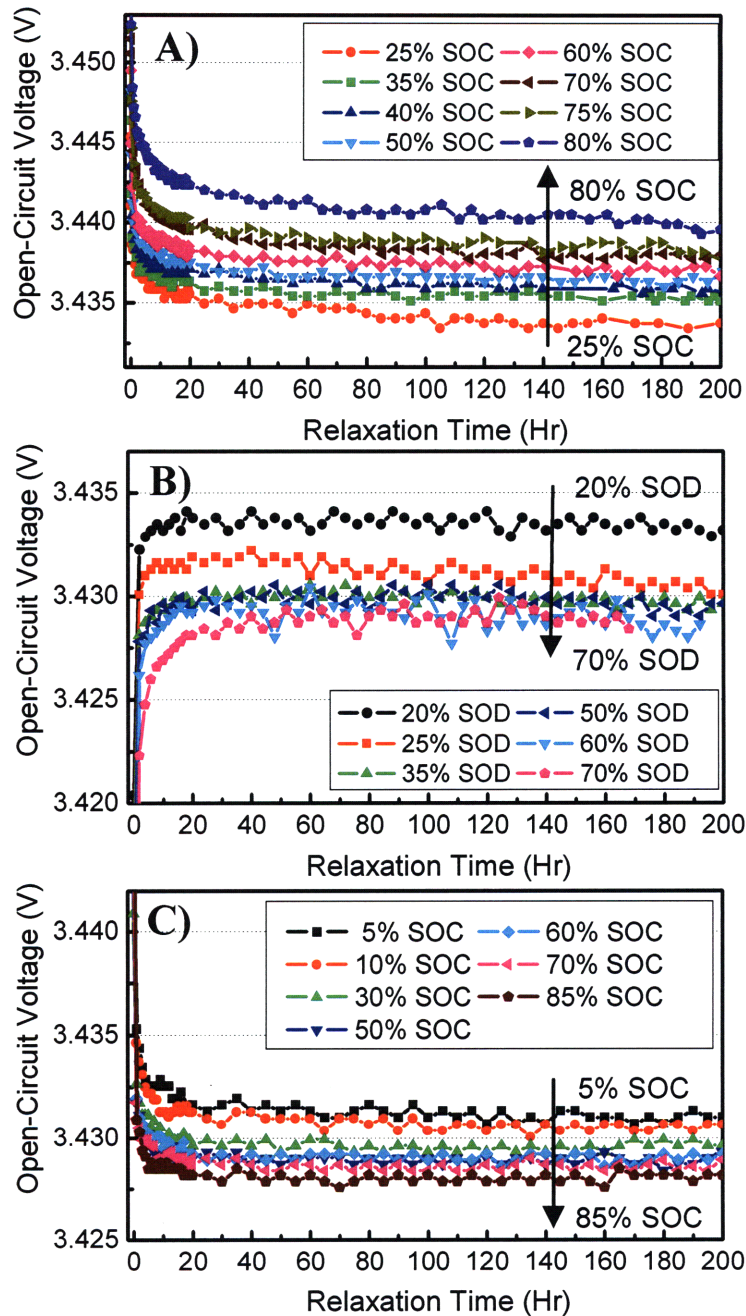


Figure 5-2: Time dependence of OCV of (A) sample A after charging to various states of charge, SOC; (B) sample A after discharging to various states of discharge, SOD; and (C) sample C after charging to various SOC. A relaxation of the OCV that takes place over as long as 100 h is seen in sample A, and over 20-40 h for sample C. The relaxed value of OCV is seen to be a function of SOC and SOD.

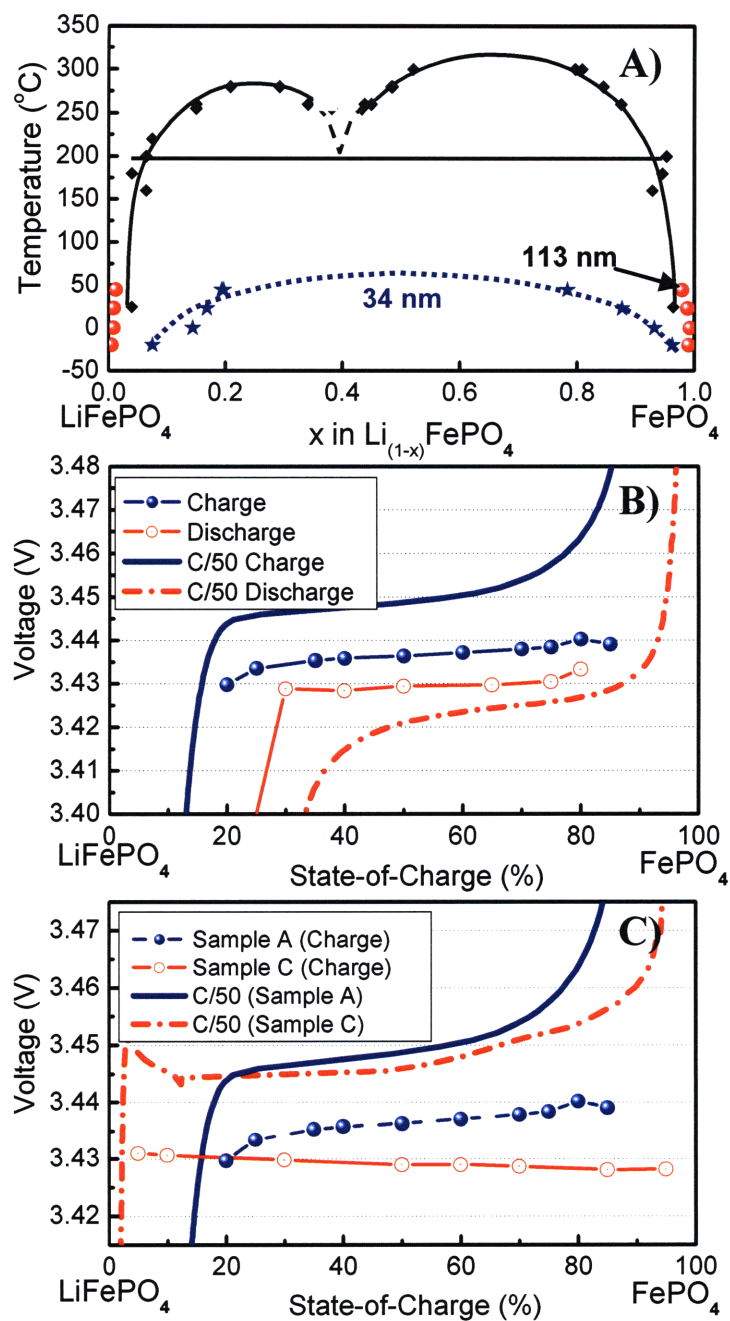
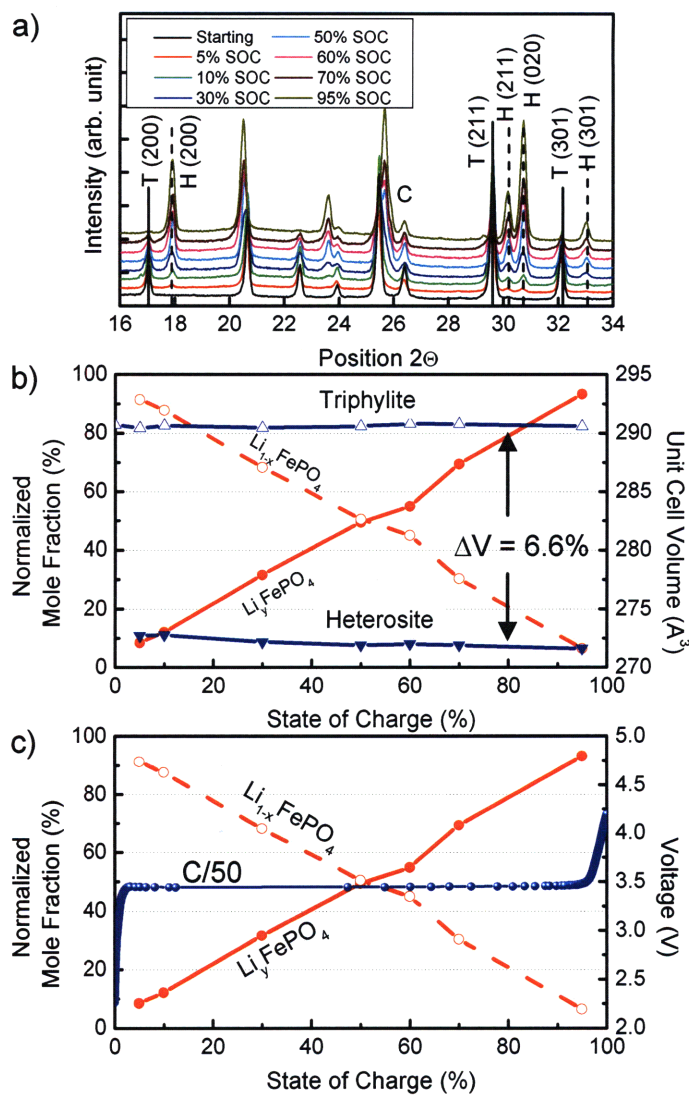
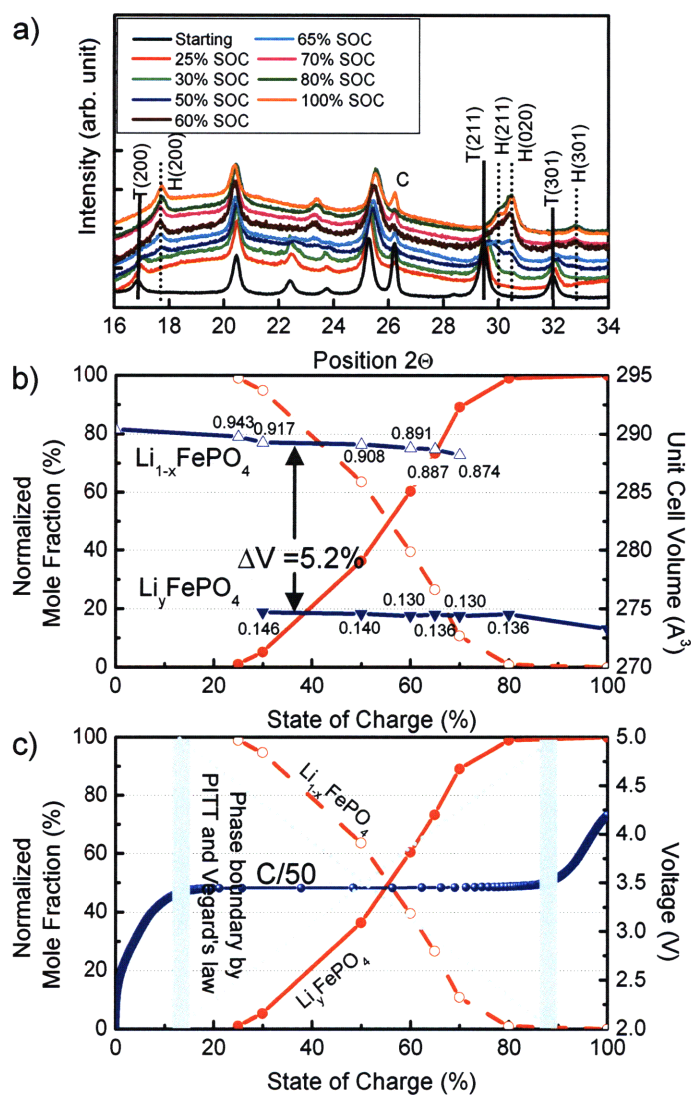


Figure 5-3: (A) Temperature dependent miscibility data for samples A and C from ref 7 plotted against the equilibrium phase diagram of Dodd et al.<sup>6</sup> (B) Room temperature terminal OCV and galvanostatic voltage curve at C/50 rate measured on both charging and discharging of sample A. (C) Terminal OCV and C/50 galvanostatic charge curves measured at room temperature as a function of state-of-charge for samples A and C.



**Figure 5-4: Results for sample C showing nearly ideal two-phase reaction. (A) XRD spectra taken as a function of state-of-charge from starting material to 95% SOC with “H” representing heterosite, “T” representing triphylite, and C denoting the graphite (002) reflection from carbon additive in the electrode formulation. Only a portion of the full spectra obtained from 15° to 135° 2-theta are shown. (B) Unit cell volumes and the normalized crystalline phase fraction of triphylite (unfilled symbols) and heterosite (filled symbols). (C) Galvanostatic voltage curve at C/50 measured at room temperature.**





**Figure 5-5: Results showing phase evolution in nanocrystalline sample A. (A) XRD spectra taken as a function of state-of-charge, from starting material to 100% SOC. Only a portion of the full spectra obtained from  $15^\circ$  to  $135^\circ$  2-theta are shown. (B) Unit cell volumes and the crystalline phase fraction of  $\text{Li}_y\text{FePO}_4$  (filled symbols) and  $\text{Li}_{1-x}\text{FePO}_4$  (unfilled symbols). The nonstoichiometry parameters  $x$  and  $y$  calculated from Vegard's law are given next to each unit cell volume datum. (C) Galvanostatic voltage curve measured at C/50 rate at room temperature. The phase boundaries measured in ref 7 by electrochemical (PITT) and x-ray diffraction (Vegard's law) techniques are shown as shaded vertical lines.**

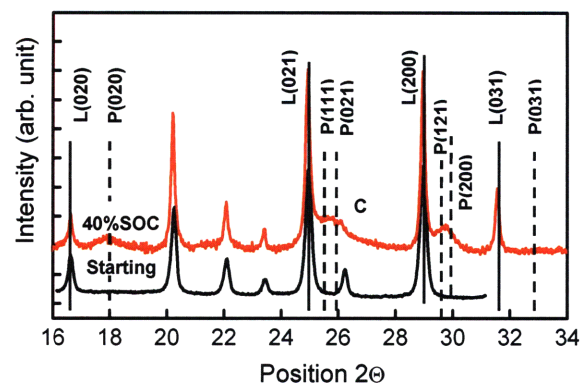


**Figure 5-6: XRD spectra of sample M in its starting state and after charging to composition  $\text{Li}_{0.60}\text{MnPO}_4$ . The sample exhibits broadened peaks for the delithiated  $\text{Li}_y\text{MnPO}_4$  (labeled “P”) phase indicating that the newly formed phase is highly disordered.**

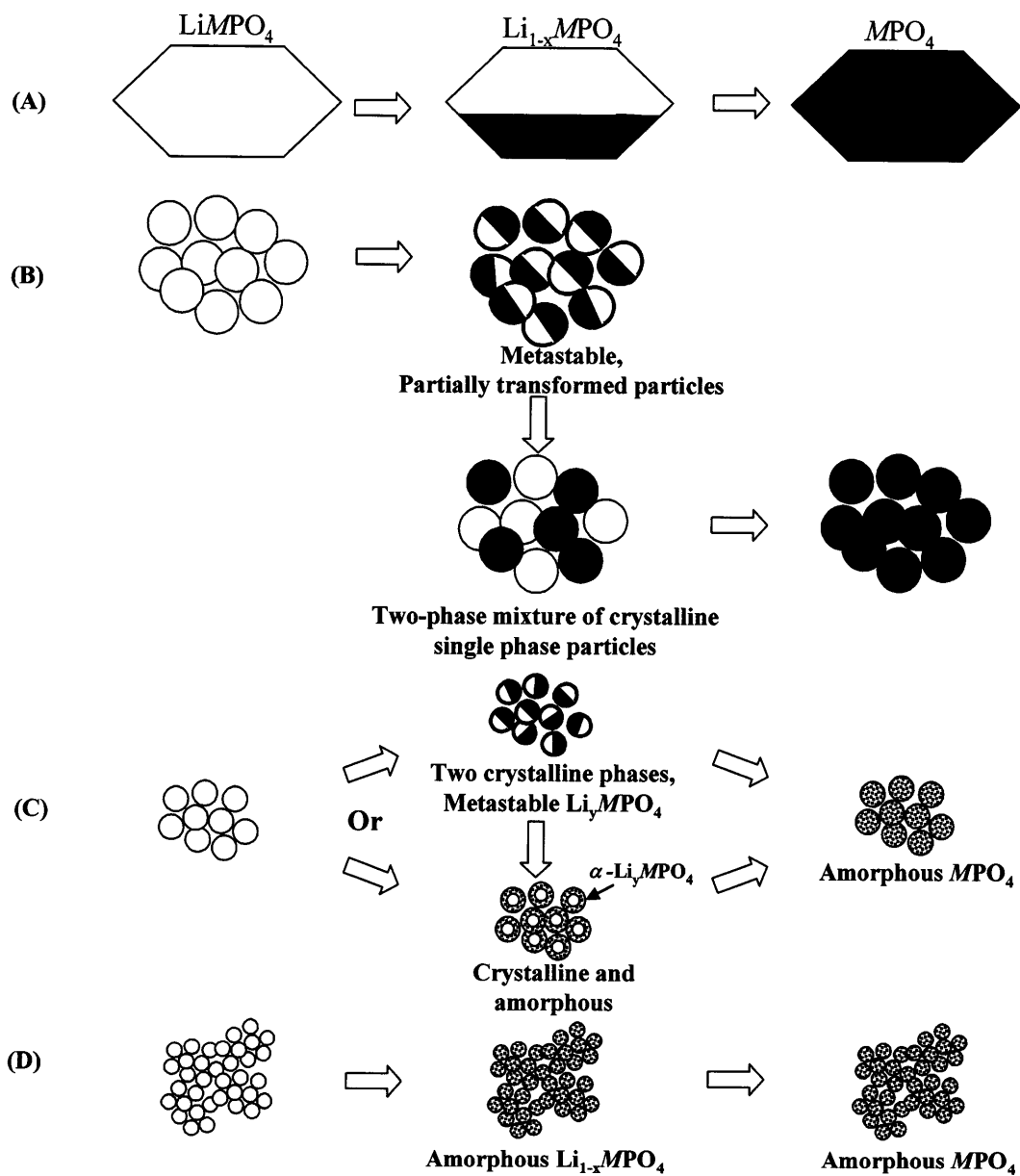


**Figure 5-7: Phase transformation pathways between lithiated and delithiated phases in  $\text{LiMPO}_4$  olivines.**

# Chapter 6

## **Aliovalent substitutions in olivine lithium iron phosphate and impact on structure and properties**

Nanoscale (<100nm) derivatives of the olivine family  $\text{LiMPO}_4$  ( $M = \text{Fe, Mn, Co, Ni}$ ) have become of particular interest for transportation and energy applications ranging in size scale from hybrid and plug-in hybrid electric vehicles to utilities-scale power regulation. Following the previous paradigm set with intercalation oxides, most studies have focused on the pure ordered compounds and isovalent transition metal substitutions. In contrast, the possibility for, and role of, aliovalent doping of the olivines has been widely debated.

In this chapter, we carry out critical tests of the plausible defect compensation mechanisms using compositions designed to accommodate  $\text{Mg}^{2+}$ ,  $\text{Al}^{3+}$ ,  $\text{Zr}^{4+}$ ,  $\text{Nb}^{5+}$  ions on the M1 and/or M2 sites of  $\text{LiFePO}_4$  with appropriate charge-compensating defects, and obtain conclusive crystallographic evidence for lattice doping, in the case of Zr up to more than 10 atomic percent added solute. Structural and electrochemical analyses show that doping can induce a reduced lithium miscibility gap, increased phase transformation kinetics during cycling, and expanded Li diffusion channels in the structure. Aliovalent modifications may be an effective tool for introducing controlled atomic disorder into the ordered olivine structure to improve battery electrode performance.

---

Reproduced with permission from *Adv. Funct. Mater.*, 7, 1 (2009). Copyright 2009, WILEY-VCH Verlag GmbH & Co. KGaA, Weinheim.

## Introduction

In previous intercalation oxides used as lithium storage electrodes for rechargeable lithium batteries, such as the ordered rock-salts  $\text{LiMO}_2$  and spinels  $\text{LiM}_2\text{O}_4$ , a highly successful route to structure and property optimization has been the mixing of transition metals and other isovalent substitutions. However, in ionocovalent compounds it is also possible to introduce aliovalent solutes along with appropriate charge-compensating point defects, and these may have as great or greater impact on structure and transport properties as isovalent substitutions. Although this possibility was first discussed for lithium iron phosphate by Chung *et al.*<sup>1</sup> in 2002, numerous groups have since challenged whether aliovalent doping is even possible in this family of compounds. For example, Ravet *et al.*<sup>2</sup> stated that “Contrary to spinels, the olivine structure is unfavorable to aliovalent doping.” and “It is thus unlikely that dopants on either M1 or M2 sites with charges varying from 1+ to 5+ could: i) dissolve in the lattice; ii) create vacancies; or iii) induce high conductivity...” Subsequently, Islam *et al.*<sup>3</sup> concluded from atomistic simulations that “ $\text{LiFePO}_4$  is not tolerant to aliovalent doping (e.g., Al, Ga, Zr, Ti, Nb, Ta) on either Li (M1) or Fe (M2) sites,” a point that is further reinforced in a recent paper.<sup>4</sup> Experimental studies from established groups that raised similar doubts include work by Delacourt *et al.*<sup>5</sup> in which it was remarked that “Nb was never observed, through elemental analysis techniques, within the  $\text{LiFePO}_4$  crystallites themselves,” and by Ellis *et al.*<sup>6</sup>, where it was concluded that “(a) Zr does not act as an internal dopant to stabilize lithium substoichiometry to any large extent; and (b) the Zr is likely primarily located on the surface of the particles.” Since the present work was completed and presented,<sup>7</sup> a communication<sup>8</sup> by some of the same authors as ref. <sup>6</sup> reverse their earlier conclusion, and reinforces some of the conclusions of the present work. Nonetheless, despite recent defect chemical studies in support of some mechanisms of aliovalent doping<sup>9</sup>, other scientific opinion is exemplified by comments such as those by Zaghib *et al.*<sup>10</sup> on “The impossibility for doping  $\text{LiFePO}_4$ ...” and that “Of course, doping  $\text{LiFePO}_4$  with pentavalent ion is even more impossible...” Clearly, aliovalent doping has not been a generally accepted mechanism of crystal-chemical modification in lithium transition

metal olivines. Research directions leading to critically needed improvements in battery technology may be overlooked with such a view.

## **Experimental Section**

### **Experimental Strategy**

We carried out an experimental strategy aimed at testing each of the most probable solute substitution mechanisms in  $\text{LiMPO}_4$ . The charge compensation of supervalent solutes requires formation of defects with a negative effective charge (herein we will use Kröger-Vink notation to denote effective charge). Like other oxides based on a close-packed oxygen sublattice, oxygen interstitials are expected to have a large free energy of formation compared to vacancy defects. Thus charge compensation of supervalent cations is most likely to be accomplished through cation vacancies. With two non-equivalent octahedral cation sites (M1 and M2), the number of distinct defect mechanisms is relatively small. Model compositions, Table 6-I, were prepared to test the four limiting-case ionic defect compensation schemes (Mechanisms 1-4). In each case, the overall cation ratios were adjusted to promote a particular solid solution mechanism, with the dopant substituting on either the M1 or M2 sites, and being charge-compensated by vacancies formed on the M1 or M2 sites. The phase content, unit cell parameters, atomic site occupancy, and dopant distribution in the experimental materials were characterized. This approach using compositions of controlled cation ratio to determine preferred mechanisms of solute incorporation has previously been used to great effect in perovskites.<sup>11</sup> To represent aliovalent cations of 2+ through 5+ valence, we used the dopants  $\text{Mg}^{2+}$ ,  $\text{Al}^{3+}$ ,  $\text{Zr}^{4+}$  and  $\text{Nb}^{5+}$ , each of which has ionic radius close to (slightly smaller than) that of the host cations  $\text{Li}^+$  and  $\text{Fe}^{2+}$ , and should readily substitute onto the host sites. Mechanism 1, formulated with the dopant on the M1 site and charge compensating vacancies also on the M1 site, and Mechanism 3, having the dopant on the M1 site and charge compensating vacancies on the M2 site, are two mechanisms specifically proposed by Chung *et al.*<sup>1</sup> Mechanism 2 with a supervalent solute substituted for Fe and charge compensated by M1 vacancies is the model which Amin *et al.*<sup>9</sup> have concluded applies to their float-grown Al-doped single crystals. In Table 6-I, the charge

compensation schemes are given in terms of the overall composition of the sample and also in Kroger-Vink notation for Mechanisms 1-4, taking  $Zr^{4+}$  as an example. Mechanism 5 represents the case where the dopant oxide  $M_xO_y$  is simply added to a stoichiometric  $LiFePO_4$  with no attempt to promote a particular defect compensation mechanism. This experimental framework allows us to determine: 1) whether aliovalent solutes are in fact soluble in the olivine structure; 2) if so, which defect compensation mechanisms provide the largest solubility and the most significant changes to the structure; and 3) the effect of doping on the phase stability and other electrochemical properties. An undoped  $LiFePO_4$  sample prepared by the same method was used as a control.

### **Test Materials**

The samples were prepared using a previously described synthesis method.<sup>1</sup> The procedure and firing schedule are depicted on Figure 6-1.  $Li_2CO_3$ ,  $FeC_2O_4 \cdot H_2O$ , and  $NH_2H_2PO_4$ , each assayed to determine the true metals content, were weighed in an Ar-filled glovebox (<3ppm oxygen and water), then mixed by ball-milling in acetone. The cation dopants were added using the following salts of reagent-grade purity (Alfa-Aesar, Ward Hill, Massachusetts, USA):  $Mg_2C_2O_4 \cdot 2H_2O$ ,  $Al(OC_2H_5)_3$ ,  $Zr(OC_2H_5)_4$ ,  $Nb(OC_2H_5)_5$ . The powder was dried and calcined at 350°C for 10 h in flowing Argon, then at 700°C in flowing Argon for 5 h. The specific surface area of the resulting powders was measured by the BET method (Brunauer, Emmett and Teller), and the equivalent spherical particle diameter calculated assuming 3.6 g/cm<sup>3</sup> crystal density.

### **Structure Analysis**

X-ray patterns of the powders were obtained using a Rigaku RTP500RC or PANanalytical X'Pert instrument with a rotating anode and Cu  $K_\alpha$  radiation, with a slow scan rate of 0.18° min<sup>-1</sup> over a 2 $\theta$  range from 15° to 135°. High quality data sets were obtained, as indicated by  $R_{exp}$  values of ~1.5. Time-of-flight (TOF) neutron diffraction data were collected at the General Purpose Powder Diffraction (GPPD) beamline at the Intense Pulsed Neutron Source at Argonne National Laboratory, USA. Neutron data were

collected at room temperature using a vanadium canister and from 3 detector banks to ensure good data quality at low, medium, and high collecting angles. The structural parameters for each of the four aliovalent dopants added at a 5 at% level according to mechanisms 1-5 were determined by Rietveld refinements of X-ray spectra. The structural parameters and site occupancy of the 5% Zr doping level according to mechanism 1 were determined through simultaneous Rietveld refinements of combined neutron and X-ray data using the *EXPGUI* interface<sup>32</sup> and the *General Structural Analysis Suite* (GSAS) software.<sup>33</sup> Starting lattice parameters and atomic positions were taken from Ref.19 and starting isotropic temperature factors were taken from Ref.20 (with conversion from  $B_{\text{iso}}$  to  $U_{\text{iso}}$  values).

### **Electron Microscopy**

Imaging and elemental mapping was done using a VG HB603 scanning transmission electron microscope operating at 250 kV accelerating voltage (Vacuum Generators, East Grinstead, UK), equipped with a Link Systems (Oxford Instrument, High Wycombe, UK) energy-dispersive X-ray analyser.

### **Electrochemical Tests**

Electrochemical tests were performed using electrodes formulated with 79 wt% positive active material, 10 wt% conductive carbon black (Super P™, M.M.M. Carbon, Brussels, Belgium) and 11 wt% Kynar 2801 binder, using acetone as the solvent. The formulation was coated onto aluminum foil current collectors at a loading of  $\sim 5 \text{ mg/cm}^2$  of active material, and assembled in Swagelok™ type cells using Li metal foil as the counterelectrode, a microporous polymer (Celgard 2400™, Hoechst Celanese Corporation, Charlotte, NC, USA), and liquid electrolyte mixtures containing 1:1 by mole ethylene carbonate: dimethyl carbonate (EC:DMC) or ethylene carbonate: diethyl carbonate (EC:DEC), and 1 M  $\text{LiPF}_6$  as the conductive salt. Electrochemical cells were galvanostatically cycled for 2 cycles within 2.0 - 4.2V voltage range at room temperature before studied with potentiostatic intermittent titration technique (PITT) with a 5 mV



voltage step within 2.0-3.8V voltage range and cut-off current of C/50 using Arbin or Maccor instrumentation.

## Results and Discussion

### Bulk Solid Solution of 2+ through 5+ Aliovalent Dopants

X-ray and neutron diffractions were used to determine structural parameters (this Section) and site occupancies (Section 5). We first compare results for each of the four aliovalent dopants added at a 5 at% level. Lattice parameters and unit cell volumes determined by Rietveld refinements of X-ray spectra are shown in Figure 6-2. The dashed horizontal lines are the values for the undoped control sample. With increasing dopant valence, we see an unmistakable increase in the  $a$  and  $b$  lattice parameters, with the  $c$ -axis changing rather less except in the instance of mechanism 1. Measurable solid solubility for each of the five composition families is clearly indicated by the systematic variation in unit cell dimensions and volume. Doping according to Mechanism 1 produces distinctly larger increases in each of the cell parameters and in the unit cell volume. In the remainder of this paper, we focus on this doping scheme, which has the aliovalent dopant (or  $\text{Fe}^{2+}$ ) occupying the M1 site with charge compensation being provided by M1 vacancies. Detailed results for the other compensation mechanisms will be published elsewhere.

A series of compositions  $\text{Li}_{1-4y}\text{Zr}_y\text{FePO}_4$  were prepared, with  $y$  ranging from 0.01 to 0.10. Figure 6-3a shows limited  $2\theta$  ranges of the X-ray diffraction spectra for seven of the compositions in this series. High-quality spectra ( $R_{\text{exp}} \sim 1.5$ ) were collected using a Rigaku RTP500RC instrument at scan rates of  $0.18^\circ \text{ min}^{-1}$  over the  $2\theta$  range from  $15^\circ$  to  $135^\circ$ . Lines for NASICON phases of several compositions are shown for comparison. At low Zr levels the predominant phase is the olivine, although vague “shoulders” around the peak at  $30^\circ 2\theta$  do not allow us to rule out the presence of trace  $\text{Fe}_2\text{P}_2\text{O}_7$ . With increasing Zr content, a single NASICON phase becomes clearly detectable and grows in amount. The peak positions for this NASICON phase shift slightly to lower angles with increasing overall Zr doping level, suggesting an evolution in composition from

$\text{Li}_2\text{FeZr}(\text{PO}_4)_3$  towards the pure Zr NASICON  $\text{LiZr}_2(\text{PO}_4)_3$ . We refined the X-ray spectra assuming a mixture of these two phases and obtained the unit cell parameters and phase fractions of olivine and NASICON. The variation in olivine unit cell volume with Zr concentration is shown in Figure 6-3b. Note that the olivine unit cell expands almost linearly in volume with the Zr doping level and has not yet saturated at 10 at%. Clearly, Zr is highly soluble in  $\text{LiFePO}_4$  when the overall composition is formulated to allow for cation substitution onto the M1 sites with charge compensating M1 vacancies. As further support, Figure 6-4 shows STEM analyses of a 5% Zr sample doped by this mechanism, in which Zr is uniformly detected in the crystallites.

In several previous studies attempting to dope  $\text{LiFePO}_4$  with aliovalent solutes,<sup>5,6</sup> the appearance of a secondary phase, such as NASICON in the present samples, has been taken to mean that the solid solubility limit has been exceeded. Here we explain why this reasoning is thermodynamically incorrect and why the appearance of one or more additional phases in such a multicomponent system does *not* mean that the solubility limit of the olivine has been exceeded. Furthermore, we present experimental evidence showing that this is precisely what occurs in Zr-doped  $\text{LiFePO}_4$ .

The Li-Fe-Zr-P-O system is a five-component system if the concentration of each element is free to vary (as in a metal alloy), but one compositional degree of freedom is lost and the number of components is reduced to four if all elements have a single valence state. This is because charge neutrality then constrains the ratios of elements in any phase. (If two iron valences are allowed in the ionic compounds a degree of freedom is gained back,  $\text{Fe}^{2+}$  and  $\text{Fe}^{3+}$  being then treated as separate components.) Taking the most restrictive condition (smallest number) of four components, at fixed temperature and pressure the Gibbs phase rule allows for three degrees of freedom ( $F = 3$ ) when olivine and NASICON are the only coexisting phases ( $P = 2$ ). ( $F = C - P + 1$ , where  $F$  is the number of degrees of freedom,  $C$  the number of components, and  $P$  the number of phases.) Allowing for another minor phase would still leave two degrees of freedom. Under such conditions the thermodynamic activity of components is not fixed, and it is perfectly permissible for the Zr solubility in the olivine to vary with the overall composition despite the presence of NASICON (or other phases, until  $F = 0$ ). Many

examples of such behavior exist in multicomponent systems; for a simple illustration we point to a ternary phase diagram no.9775a in Phase Diagrams for Ceramists<sup>12</sup>, where a three-component system exhibits a wide two-phase coexistence field within which the compositions of the two phases (joined by tie-lines) vary continuously.

The results in Figure 6-5 show that Zr-doped compositions (Mechanism 1) exhibit such behavior. With increasing Zr doping level the relative amount of NASICON phase (open circles) increases almost linearly, reaching just under 20 wt% NASICON at the highest Zr content tested (0.10 mole fraction), while the weight percentage of olivine decreases linearly (open squares). However, the olivine unit cell volume (closed squares) increases linearly showing continued incorporation of Zr. The NASICON unit cell volume (closed circles) also varies continuously but not in a linear manner; it increases sharply from zero to about 0.02 mole fraction Zr and then increases with a shallower slope with Zr level. Clearly the Zr activity is not constant in either the olivine or NASICON phase across this composition range. In experiments on the same composition system, Ellis *et al.*<sup>6</sup> erroneously took the appearance of the Zr-rich NASICON phase to indicate that the solubility of Zr in the olivine has been exceeded, which would only be correct if the system had reached zero compositional degrees of freedom. Instead, with increasing Zr doping the amount of Zr in both the olivines and NASICON phases continues to increase. The same thermodynamic principles apply for any dopant. There is a common belief often expressed in literature that a single-phase doped sample is somehow a “good” sample and that one containing additional phases is inferior, which these considerations show to be fallacious. From the linear variation of unit cell volume with Zr doping (Vegard’s law) in Figure 2b, the variation in Zr level in the olivine phase can be obtained if the lattice concentration is known for any one doped sample. This information is obtained independently from structural refinement of neutron diffraction data in the later section.

### **Effect of Particle Size on Dopant Solubility**

Particle-size dependent solid solubility can occur for various reasons, but most frequently when there is a sufficiently large surface/volume ratio and the solute in question is

surface-active. Nanoscale  $\text{TiO}_2$  is one system in which size-dependent solid solubility due to interfacial segregation of dopants has been studied.<sup>13</sup> Since the powders prepared in this study generally had <100nm particle size, it was of concern to us to determine whether the observed high dopant solubility is due to, or at least influenced by, the small crystallite size. Although the interfacial segregation of solutes has not been studied (in part since, until now, solid solution behavior has not been accepted), some predictions are possible from basic theory. For aliovalent solutes in ionic compounds, there in general exists an electrostatic driving force for interfacial segregation, which has been studied for a number of oxide systems doped with supervalent and subvalent cations.<sup>14-17</sup> For doped olivines with extrinsic defect structures such as those in Table 6-I, it can be shown from basic theory<sup>14-18</sup> that the introduction of bulk cation vacancies will cause an initially neutral surface will develop a negative charge, adjacent to which forms a positive space-charge penetrating the crystal. If the supervalent cations are sufficiently mobile, they will accumulate in the space-charge in response to the negative surface charge. (Other charged defects will also redistribute.) The dopant may also have other driving forces for segregation, such as the elastic energy due to ion size misfit, which can cause segregation at surface sites (or other lattice discontinuities) resulting in further contributions to the total amount of interfacial segregation.

We tested the size-dependent solid solubility hypothesis by taking one highly doped sample, having 7.5% Zr (Mechanism 1), and heat treating it to coarsen the particle size from an initial average particle size of 45 nm. As shown in Figure 6-5, under firing conditions that result in coarsening of the powder particle size to size scales well beyond that at which significant size-dependent effects are expected (>1  $\mu\text{m}$ ), there is a slight decrease in the unit cell volume, which points to some role of size-dependent solubility. However, even at the highest firing temperature (coarsest particle size) the unit cell volume remains well above that of the undoped sample. This indicates that the high solid solubility of Zr (and by inference other dopants) is fundamentally a bulk phenomenon. Nonetheless, these size-dependent solubility effects are interesting and warrant further study.

## Site Occupancies in Doped Solid Solutions

Having indications from the change in unit cell parameters that bulk doped solid solutions do exist, we next used X-ray and neutron diffractions together to determine the atomic site occupancy and the detailed changes in structure upon doping. Simultaneous Rietveld refinements of multiple-data sets (three neutron diffraction profiles covering low, medium and high angle reflections, and X-ray diffraction from 15°-135° 2 $\theta$ ) were carried out using initial lattice parameters and atomic coordinates from Ref. 19 and isotropic thermal parameters from Ref. 20. Figure 6-7 shows the Rietveld refinement results when different M1/M2-site occupancy models are applied to the neutron diffraction profile for a single sample doped with 5% Zr according to Mechanism 1. It can be seen that the quality of the Rietveld refinement was least satisfactory when an ordered stoichiometric LiFePO<sub>4</sub> was assumed (Figure 6-7b,  $\chi^2 = 2.422$ ) or when M2-site substitution by the Zr with charge compensation by M2 vacancies was assumed (Figure 6-7c,  $\chi^2 = 3.432$ ). The quality of refinement improved significantly when the theoretical site occupancy of this sample, Li<sub>0.80</sub>Zr<sub>0.05</sub>Δ<sub>0.15</sub>FePO<sub>4</sub>, was assumed (Figure 6-7d,  $\chi^2 = 1.980$ ). When Li and Zr were confined to the M1 site and Fe to the M2, but the concentration of each was allowed to vary, the best fit was obtained for the site occupancy (Li<sub>0.845</sub>Zr<sub>0.043</sub>Δ<sub>0.112</sub>)(Fe<sub>0.979</sub>Δ<sub>0.021</sub>)PO<sub>4</sub> ( $\chi^2 = 1.885$ ), Figure 6-7a. The refinement thus provides an independent determination of the actual amount of Zr in solid solution: at 4.3 mole %, it is 86% of the overall doping level (5 %). It is reasonable that the amount in solution in the olivine is somewhat reduced from the overall level given that there is about 9% NASICON phase at this doping level (Figure 6-6). Extrapolating linearly the olivine unit cell volume with doping level (Vegard's law) in Figure 6-3b indicates that at the highest Zr doping level tested, the amount in solid solution is about 8.6 mole %. Even this level must be regarded as only a lower limit to the maximum Zr solubility since Figure 6-3b shows no deviation from linearity yet at this doping level. Overall, the refined site occupancies indicate that the defect compensation mechanism is very close to the theorized extrinsic mechanism:  $3[\text{Zr}_{\text{Li}}^{\bullet\bullet}] = [\text{V}_{\text{Li}}']$ . The site-occupancies, atomic coordinates, and thermal parameters of this sample are summarized in Table 6-II. For each of the other solutes (Mg<sup>2+</sup>, Al<sup>3+</sup>, Nb<sup>5+</sup>) doped according to Mechanism 1, the

refinements also indicated that the dopant predominantly occupies the M1 site, as will be discussed elsewhere.

Since the concentration of charge-compensating vacancies increases with the valence  $n$  of the dopant, the relationship being given specifically by  $[V_{Li}'] = (n-1)[M_{Li}^{(n-1)}]$  for Mechanism 1, we are able to conclude from the present results that all else being equal, lithium vacancies cause the olivine unit cell to expand. Figure 6-2 shows a monotonically increasing unit cell expansion with dopant valence  $n$  even though each of the dopants ( $Mg^{2+}$ ,  $Al^{3+}$ ,  $Zr^{4+}$ ,  $Nb^{5+}$ ) has smaller 6-fold ionic radii (0.072, 0.054, 0.072, and 0.064 nm respectively) than both  $Li^+$  (0.076 nm) and  $Fe^{2+}$  (0.078 nm). This conclusion is further supported by the linear expansion upon Zr doping shown in Figure 2. Thus the partial molar volume of lithium is shown to be *negative* in this compound. Note that this conclusion is not in conflict with the nearly linear decrease in unit cell volume observed in  $Li_{1-x}FePO_4$  solid solutions with increasing  $x$ , since in that case delithiation is accompanied by the replacement of  $Fe^{2+}$  (0.078 nm) with the smaller  $Fe^{3+}$  (0.065 nm) ion. Doping with aliovalent solutes that are charge-compensated by Li vacancies therefore produces an expansion of the olivine lattice relative to ideal stoichiometric  $LiFePO_4$ , whereas delithiation causes lattice contraction.

We were interested in whether the lattice expansion induced by doping could influence the kinetics of ion transport. Examination of bond lengths in the doped samples showed that the increased unit cell volume was associated with increased lithium-oxygen and oxygen-oxygen bond lengths. In the olivine structure ( $Pnma$ ), inspection suggests that  $Li^+$  will not migrate directly through the shared edge (O1-O2) between  $LiO_6$  octahedra, but instead should follow a curved migration path through the adjacent interstitial space, illustrated in Figure 6-8. The activation energy for this migration path, which traverses an opening defined by the oxygen bond lengths O1-O2-O3, has been modeled by Morgan *et al.*<sup>21</sup> and Islam *et al.*<sup>3</sup> with the values obtained differing by more than a factor of two (270 meV and 550 meV, respectively). Nonetheless, its plausibility is supported by recent experiments by Nishimura *et al.*<sup>22</sup> that provide an elegant and direct experimental visualization of the Li migration path. In Table 6-III, we show bond length data obtained

from the undoped control sample and four samples doped according to Mechanism 1 with 10% Mg, 5% Al, 5% Zr, and 5% Nb respectively. The O-O bond lengths are increased in all of the doped samples compared to the undoped control sample, with the largest expansions being as follows: O1-O2, +0.02 Å; O2-O3, +0.013 Å; O1-O3, +0.006 Å. The Li-O bond lengths are also all increased: Li-O1, +0.012 Å; Li-O2, +0.008 Å; and Li-O3, +0.010 Å, as are certain of the Fe-O bond lengths. Comparing the Al<sup>3+</sup>, Zr<sup>4+</sup> and Nb<sup>5+</sup> series at the same 5% doping level, each of the O-O bond lengths increases monotonically with the valence of the dopant (i.e., the number of charge-compensating vacancies introduced per dopant atom). Although we have not done so, this structural data could be used to compute changes in lithium migration activation energy. For example, a comparable expansion of 0.02 Å of the lithium slab spacing in Li(Mn,Ni)O<sub>2</sub> results in a 20-30 meV decrease in the calculated Li migration energy.<sup>23</sup> However, any consideration of Li migration in the olivine structure must also take into account the effects of less mobile cations occupying the [010] M1 channels, a point we return to later.

### **Potentiostatic Titration Measurements of Lithium Immiscibility and Phase Transformation Kinetics**

Although the main focus of this work was the elucidation of dopant solubility and defect mechanisms, we also obtained some results relating to the effect of doping on the lithium miscibility and phase transformation kinetics. These characteristics have been correlated with the ability of nanoscale olivines to deliver stored energy at high charge/discharge rates in previous work.<sup>24,25</sup> Potentiostatic intermittent titration tests (PITT) are particularly useful for characterizing such behavior, for the following reasons. Since true two-phase coexistence is characterized by a constant open circuit voltage (OCV), careful measurement of the charge capacity above, and discharge capacity below, the OCV can be used to measure directly the extent of solid solution (phase boundaries). Unlike galvanostatic tests, PITT allows the capacity at a given potential to be measured without the application of any overpotential. In the absence of an overpotential, there is no thermodynamic driving forces for phase transformation until the OCV is exceeded. In this methodology,<sup>24</sup> the room-temperature OCV of the cells is first measured with the samples at 50% SOC, well within the miscibility gap, to obtain the OCV for an

equilibrated two-phase state. Then, the cumulative charge capacity below the OCV is measured upon charging in small constant-voltage steps (5 mV), allowing the current to relax to  $<C/100$  at each voltage. The cumulative discharge capacity above the OCV is similarly measured upon discharge from the fully charged state. The accumulated charge capacity below the OCV is then a measure of the solid solution  $x$  in the Li-rich endmember, e.g.,  $\text{Li}_{1-x}\text{FePO}_4$ , and the accumulated discharge capacity above OCV is a measure of the solid solution  $y$  in the Li-poor phase, e.g.,  $\text{Li}_y\text{FePO}_4$ .

The most complete set of results compared a 5% Mg sample doped according to Mechanism 1 with an undoped control sample of identical particle size, and are discussed here. Figure 6-9 shows results from the PITT measurement, in which it can be seen that there are substantial capacities above and below the OCV both during charge and discharge of the cell. The Li-nonstoichiometry  $x$  was calculated to be  $\sim 10.6\%$  and the Li-nonstoichiometry  $y$  to be  $\sim 13.3\%$ . PITT responses of the undoped control sample, the conventional coarse-grained sample, and 1% Nb doped nanoscale sample are plotted to the same scale in Figure 6-9 for comparison.

Compared to undoped  $\text{Li}_{1-x}\text{FePO}_4$ , which already exhibits a strong size-dependent miscibility gap in this particle size range,<sup>20,25</sup> the doped samples exhibit even greater lithium miscibility. Figure 6-10 shows the equilibrium phase diagram for bulk  $\text{Li}_{1-x}\text{FePO}_4$  published by Dodd *et al.*<sup>26</sup> compared with the solid solution limits measured using PITT for several materials. Conventional  $\text{LiFePO}_4$  of 113nm mean particle size shows very limited solid solution, whereas the lithium miscibility gap contracts significantly for undoped powder at 42nm mean particle size.<sup>25</sup> At the same particle size (as determined from BET measurements of the specific surface area) the miscibility gap is compressed further still for the 5% Mg doped nanoscale sample. The lithium-poor phase,  $\text{Li}_y\text{Mg}_{0.05}\text{FePO}_4$ , has a Li excess,  $y$ , of  $\sim 13.3\%$ , more than twice that in the undoped nanomaterial at the same (room) temperature, while the lithium-rich endmember,  $\text{Li}_{0.90-x}\text{Mg}_{0.05}\text{FePO}_4$ , has a Li deficiency,  $x$ , of  $\sim 10.6\%$ , which is about the same as for the undoped nanoscale composition. The 1% Nb-doped sample shows still further contraction of the miscibility gap on both sides.<sup>24</sup>



Doping therefore appears to have the effect of reducing the miscibility gap beyond that which can be obtained by size reduction alone. We attribute this to atomic disorder in the olivine lattice produced by the aliovalent solute and its charge-compensating defects. The results in Figure 6-10 suggest that aliovalent solutes of higher valence (e.g., Nb<sup>5+</sup> or even dopants such as W<sup>6+</sup>) have greater impact on the phase diagram per unit concentration, which may be related to the higher lithium vacancy concentration that is introduced per dopant atom.

PITT measurements can also be used to directly measure the phase transformation rate in the two-phase field, since the current measured in PITT is proportional to the phase transformation rate when the co-existing phases have fixed composition. Meethong *et al.*<sup>24</sup> have shown that the cycling-induced phase transformation in olivines is made more facile by reducing the lithium immiscibility, and misfit strain, between the co-existing phases. Figure 6-11 shows similar measurements performed on the 5% Mg sample and the undoped control of nearly identical particle size. The voltage vs. time curves are the constant-voltage PITT steps separated by 5 mV. During each constant voltage hold, the time-dependence of current (data points in red) were recorded, and show the rate of lithium exchange out of (during charge) or into the sample (during discharge). For the doped sample, the current flow starts at a maximum value when the voltage is first stepped up during charging (Figure 6-11a) or stepped down (Figure 6-11b) during discharging, then decays monotonically from there). This behavior qualitatively differs from that of the undoped Li<sub>1-x</sub>FePO<sub>4</sub> in which (Figure 6-11c) there is a local maximum in the current suggesting that a barrier to transformation is being overcome. It is unlikely that these differences in PITT kinetics are due to extrinsic factors such as electrode polarization since all of the electrodes were formulated and processed identically, the absolute currents recorded during the constant voltage holds are all less than  $\sim C/15$ , and the voltage increments are only 5 mV in magnitude. We believe these characteristics represent true differences in lithium exchange behavior at the nanoparticle level. Note that the undoped sample of 42nm size already has considerable lithium nonstoichiometry, yet shows sluggish phase transformation kinetics compared to the doped sample. The undoped nanoscale sample has qualitatively similar behavior during charge to a 113 nm

undoped carbon-coated material reported in reference.<sup>24</sup> The detailed modeling of the current transients in terms of kinetic steps has proven to be complex, but may provide additional insight when complete.

At high doping levels, the improvement in kinetics does not come without penalty, however. The fast kinetics of the 5% Mg sample is mitigated by lower absolute values of charge and discharge capacities, 114 and 110 mAh/g respectively (compared to typical capacities >150 mAh/g in less highly doped samples). This reflects a compromise that must be struck in designing doped compositions between lithium channel blocking and the beneficial effects of phase diagram manipulation and, possibly, lithium diffusion channel expansion.

### **Summary and Conclusions**

The present results show that aliovalent solutes of 2+ through 5+ valence are readily accommodated in the olivine lattice, especially when the overall composition is formulated to allow the simultaneous introduction of cation vacancies for charge compensation. The approach of intentionally producing a nonstoichiometric cation ratio to accommodate the introduction of an aliovalent solute and its charge-compensating defect, demonstrated long ago in other ionic compounds,<sup>11</sup> appears to be effective in olivines as well. The total energies for such compensation processes were not considered in recent computational studies that concluded that aliovalent solutes are insoluble.<sup>3,4</sup> Chung *et al.*<sup>1</sup> had originally proposed that supervalent solutes smaller in size than the host  $\text{Li}^+$  and  $\text{Fe}^{2+}$  should preferentially occupy M1 sites, rather than exchanging sites with  $\text{Fe}^{2+}$  for example. This tendency is supported by the present results. The recent results of Wagemaker *et al.*<sup>[8]</sup> explore a single mechanism (our Mechanism 1) and are in general agreement with our results at low doping levels. However, whereas they conclude that only low levels up to about 3 mol% are soluble (see also Ref. 6), here we show that the olivine structure can accommodate much higher solubility, up to at least ~10 mole% in the case of Zr. As discussed in Section 3, neglecting the implications of the Gibbs phase rule for multicomponent systems leads to the mistaken interpretation that solid solution limits have been reached when a second phase appears. It should also be emphasized that

although Mechanism 1, having M1 site occupancy by the supervalent dopant and charge-compensation by lithium vacancies, results in the largest change in lattice constants, it does not necessarily provide the highest solubility; other defect mechanisms (Table 6-I and Figure 6-2) may have equivalent or higher absolute solubilities.

If it is then accepted that aliovalent solutes are in fact highly soluble in the olivines, the effects of doping on properties are of much interest. The present work provides additional support to previous results<sup>24,25</sup> that at nanoscale particle sizes (<100 nm), the size-dependent lithium miscibility gap in undoped  $\text{Li}_{1-x}\text{FePO}_4$  can be further manipulated by doping. The correlation between a reduced lithium miscibility gap, reduced elastic misfit between the phases participating in the first-order phase transition, and a faster rate of phase transformation during electrochemical cycling,<sup>24</sup> is upheld here. Gibot *et al.*<sup>27</sup> recently reported complete Li miscibility at room temperature in undoped but disordered nanoscale  $\text{Li}_x\text{FePO}_4$ . As they point out, Li-Fe disorder by itself is expected to be highly dependent on the synthesis method used. While the details of how the phase diagram is influenced by disorder and defect type remain to be understood, any such manipulation is more easily controlled by extrinsic doping.

Returning to the issue of [010] M1 channel blocking by less mobile ions, in addition to arguments against M1 site doping, Li-Fe disorder in  $\text{LiFePO}_4$  has been widely considered to be detrimental to electrochemical properties for the same reason.<sup>28</sup> This may well be true at large particle size or for single crystals, but at nanoscale particle sizes the actual number of blocking cations per Li channel should be considered. The [010] channels have 2 M1 sites per 0.6 nm, so a 30 nm particle having 1% of the M1 sites occupied would have on average one M1 dopant atom per channel. Since both ends of the [010] channel remain open for Li extraction and insertion, there should be almost no loss of accessible lithium. These considerations lead to the expectation of a tradeoff between [010] channel blocking and other effects of doping at particle sizes of a few nanometers, and doping levels of a few percent.

Another effect of inducing a greater lithium nonstoichiometry range  $x$  and  $y$  is that greater  $\text{Fe}^{2+}/\text{Fe}^{3+}$  multivalency will be incurred in the solid solutions produced during

electrochemical cycling, or even during the synthesis of materials. The effect of lithium nonstoichiometry on lattice electronic conductivity is another topic of much debate, and is not directly addressed by the results presented here. However, it is notable that Amin and Maier<sup>29</sup> have recently observed a  $10^3$  increase in the electronic conductivity of undoped and carbon-free  $\text{Li}_{1-x}\text{FePO}_4$  upon introducing lithium deficiency of  $x < 40$  ppm through heat treatment in “inert atmosphere,” presumably a much less reducing environment than the forming gas atmosphere used by Herle *et al.*<sup>30</sup> to produce phosphide-laden samples of high conductivity. While full discussion is beyond the scope of this paper, we wish to correct an assertion by Wagemaker *et al.*<sup>8</sup> that some among the present authors have suggested the existence of  $\text{Fe}^+$  in aliovalent doped olivines as a cause of increased conductivity, citing a patent document.<sup>31</sup> Wagemaker *et al.* misrepresent what is a simple typographical error. The only instance where  $\text{Fe}^+$  appears in the entire cited reference is a mistyped formula (column 34, line 16 of Ref. 31):  $\text{Li}^{1+}_{1-a-x}\text{M}^{3+}_x(\text{Fe}^{2+}_{1-a+2x}\text{Fe}^+_{a-2x})(\text{PO}_4)^{3-}$  where  $\text{M}^{3+}$  represents a trivalent dopant on the M1 site. There are in fact two typographical errors in the formula, which is not electrically neutral as written. From the context of the cited reference the formula is clearly intended to read:  $\text{Li}^{1+}_{1-a-x}\text{M}^{3+}_x(\text{Fe}^{2+}_{1-a+2x}\text{Fe}^{3+}_{a-2x})(\text{PO}_4)^{3-}$ . This formula in fact represents an M1-site doped composition with an extended lithium solid solution range, a composition supported by the present work.

Thus we show that aliovalent solute doping of  $\text{LiFePO}_4$  is not only possible, but has several distinct consequences which may be manipulated to improve battery electrode properties. We find that the olivine lattice can accept aliovalent cations of 2+ through 5+ at concentrations of at least several percent, with charge-compensation by M1 vacancies being at least one available defect mechanism. The disorder produced by these substitutions cause the lithium miscibility gap to be contracted, and by modifying the crystal structure so as to expand the lithium migration channels, may have the effect of increasing lithium mobility. Along with nanoscaling and other compositional modifications of the olivines, controlled aliovalent doping is a methodology that may be used to advantage in the ongoing worldwide effort to develop improved battery technologies for energy applications.

## References

1. S. Y. Chung, J. T. Bloking, Y.-M. Chiang, Electronically conductive phospho-olivines as lithium storage electrodes. *Nat. Mater.*, **1**, 123 (2002).
2. N. Ravet, A. Abouimrane, M. Armand, From our readers. *Nat. Mater.*, **2**, 702 (2003).
3. M. S. Islam, D. J. Driscoll, C. A. J. Fisher, P.R. Slater, Atomic scale investigation of defects, dopants and lithium transport in the LiFePO<sub>4</sub> olivine type battery material. *Chem. Mater.*, **17**, 5085 (2005).
4. C. A. J. Fisher, V. M. Hart Prieto, M. S. Islam, Lithium Battery Materials LiMPO<sub>4</sub> (M) Mn, Fe, Co, and Ni): Insights into Defect Association, Transport Mechanisms, and Doping Behavior, *Chem. Mater.*, **20**, 5907 (2008).
5. C. Delacourt, C. Wurm, L. Laffont, J.-B. Leriche, C. Masquelier, Electrochemical and electrical properties of Nb- and/or C-containing LiFePO<sub>4</sub> composites. *Solid State Ionics*, **177**, 333 (2006).
6. B. Ellis, P. S. Herle, Y. -H. Rho, L. F. Nazar, R. Dunlap, L. K. Perry, D. H. Ryan, Nanostructured materials for lithium-ion batteries: Surface conductivity vs. bulk ion/electron transport. *Faraday Discuss.*, **134**, 119 (2007).
7. Y.-H. Kao, N. Meethong, Y.-M. Chiang, Aliovalent Solute Solubility and Defect Compensation Mechanisms in Olivine Cathodes for Li-ion Batteries, MRS Spring 2008 Abstract # JJ3.7, March 25 - 27, 2008, San Francisco, CA., Y.H. Kao, N. Meethong, M. Tang, H.-Y. Huang, W. C. Carter, Y.-M. Chiang, Aliovalent Solute Solubility and Defect Compensation Mechanisms in Olivine Cathodes, IMLB 2008, Abstract # 47, June 22-28, 2008, Tianjin, China.
8. Wagemaker M., B. L. Ellis, D. Lutzenkirchen-Hecht, F. M. Mulder, L.F. Nazar, Proof of Supervalent Doping in LiFePO<sub>4</sub>, *Chem. Mater.*, **10**, 423 (2008).
9. R. Amin, C. Lin, J. Maier, Aluminum-doped LiFePO<sub>4</sub> single crystals, *Phys. Chem. Chem. Phys.*, **10**, 3519 (2008).
10. K. Zaghib, A. Mauger, J. B. Goodenough, F. Gendron, C. M. Julien, Electronic, Optical and Magnetic Properties of LiFePO<sub>4</sub>: Small Magnetic Polaron Effects. *Chem. Mater.*, **19**, 3740 (2007).

11. H. M. Chan, M. P. Harmer, and D. M. Smyth, "Compensating Defects in Highly Donor-Doped BaTiO<sub>3</sub>," *J. Am. Ceram. Soc.*, **69**, 507 (1986).
12. Figure 9775a, Phase Diagram for Ceramists, Volume XI, The American Ceramic Society, Westerville, Ohio, 1995.
13. C.D. Terwilliger, Y.-M. Chiang, "Size Dependent Segregation and Solid Solubility in Ultrafine Polycrystals: Ca in TiO<sub>2</sub>," *Acta Metall. Mater.*, **43**, 319 (1995).
14. Y.-M. Chiang, A.F. Henriksen, W.D. Kingery, D. Finello, "Characterization of Grain Boundary Segregation in MgO," *J. Am. Ceram. Soc.*, **64**, 383 (1981).
15. Y.-M. Chiang, T. Takagi, "Grain Boundary Chemistry of Barium Titanate and Strontium Titanate: I, High Temperature Equilibrium Space Charge," *J. Am. Ceram. Soc.*, **73**, 3278 (1990).
16. J.A.S. Ikeda, Y.-M. Chiang, "Space Charge Segregation at Grain Boundaries in Titanium Dioxide: Part I, Relationship Between Lattice Defect Chemistry and Space Charge Potential," *J. Am. Ceram. Soc.*, **76**, 2437 (1993).
17. J.A.S. Ikeda, Y.-M. Chiang, A.J. Garratt-Reed, J.B. Vander Sande, "Space Charge Segregation at Grain Boundaries in Titanium Dioxide: Part II, Model Experiments," *J. Am. Ceram. Soc.*, **76**, 2447 (1993).
18. Y.-M. Chiang, D.P. Birnie, III, and W.D. Kingery, *Physical Ceramics: Principles for Ceramic Science and Engineering*, John Wiley and Sons, New York, 1997.
19. S. Andersson, B. Kalska, L. Haggstrom, J.O. Thomas, Lithium extraction/insertion in LiFePO<sub>4</sub>: an X-ray diffraction and Mossbauer spectroscopy study. *Solid State Ionics*, **130**, 41 (2000).
20. Yamada, H. Koizumi, S.-I. Nishimura, N. Sonoyama, R. Kanno, M. Yonemura, T. Nakamura, Y. Kobayashi, Room-temperature miscibility gap in Li<sub>x</sub>FePO<sub>4</sub>. *Nat. Mater.*, **5**, 357 (2006).
21. D. Morgan, A. Van der Van, G. Ceder, Li conductivity in Li<sub>x</sub>MPO<sub>4</sub>(M=Mn, Fe, Co, Ni) Olivine Materials. *Electrochem. Solid-State Lett.*, **7**, A30 (2004).
22. S.-I. Nishimura, Y. Kobayashi, K. Ohoyama, R. Kanno, M. Yashima, A. Yamada, Experimental visualization of lithium diffusion in Li<sub>x</sub>FePO<sub>4</sub>. *Nat. Mater.*, **7**, 707 (2008).

23. K. S. Kang, , Y. S. Meng, J. Breger, C.P. Grey, G. Ceder, Electrodes with high power and high capacity for rechargeable lithium batteries. *Science*, **311**, 977 (2006).
24. N. Meethong, H.-S. Huang, S.A. Speakman, W.C. Carter, Y.-M. Chiang, Strain accommodation during Phase Transformations in Olivine-based cathodes as a materials selection criterion for high-power rechargeable batteries. *Adv. Funct. Mater.*, **17**, 1115 (2007).
25. N. Meethong, H.S. Huang, W.C. Carter, Y.-M. Chiang, Size-dependent lithium miscibility gap in nanoscale  $\text{Li}_{1-x}\text{FePO}_4$ . *Electrochem. Solid-State Lett.*, **10**, A134 (2007).
26. J. L. Dodd, R. Yazami, B. Fultz, Phase diagram of  $\text{Li}_x\text{FePO}_4$ . *Electrochem. Solid-State Lett.*, **9**, A151 (2006).
27. P. Gibot, M. Casas-cabanas, L. Laffont, S. Levasseur, P. Carlach, S. Hamelet, J.-M. Tarascon, C. Masquelier, Room-temperature single-phase Li insertion/extraction in nanoscale  $\text{Li}_x\text{FePO}_4$ . *Nat. Mater.*, **7**, 741 (2008).
28. S. Yang, Y. Song, P.Y. Zavalij, M. S. Whittingham, Reactivity, stability and electrochemical behavior of lithium iron phosphates. *Electrochem. Commun.*, **4**, 239 (2006).
29. R. Amin, J. Maier, Effect of annealing on transport properties of  $\text{LiFePO}_4$ : Toward a defect chemical model. *Solid State Ionics*, **178**, 1831 (2008).
30. P. S. Herle, B. Ellis, N. Coombs, L. F. Nazar, Nano-network electronic conduction in iron and nickel olivine phosphates, *Nat. Mater.*, **3**, 147 (2004).
31. Y.-M. Chiang, S.-Y. Chung, J.T. Bloking, A.A. Andersson, U.S. Patent 7338734, March 4, 2008.
32. H. Toby, *EXPGUI*, a graphical user interface for *GSAS*, *J. Appl. Cryst.*, **34**, 210 (2001).
33. A.C. Larson, R.B. Von Dreele, "General Structure Analysis System (GSAS)", Los Alamos National Laboratory Report LAUR 86-748, 2000.

## Chapter 6 Figures and Tables

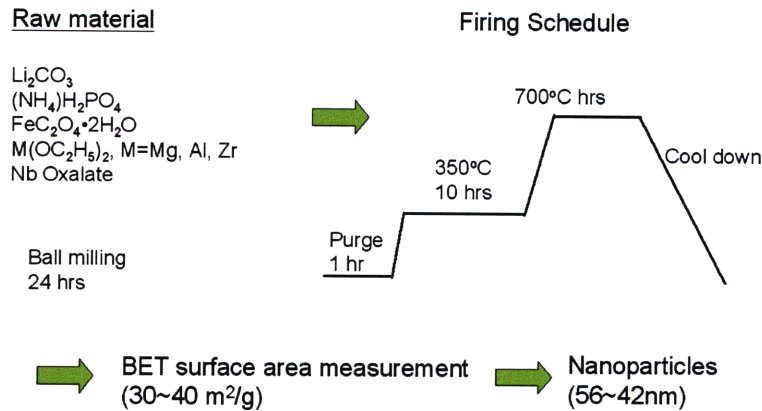


Figure 6-1: Sample preparation and firing schedule of the studied materials.

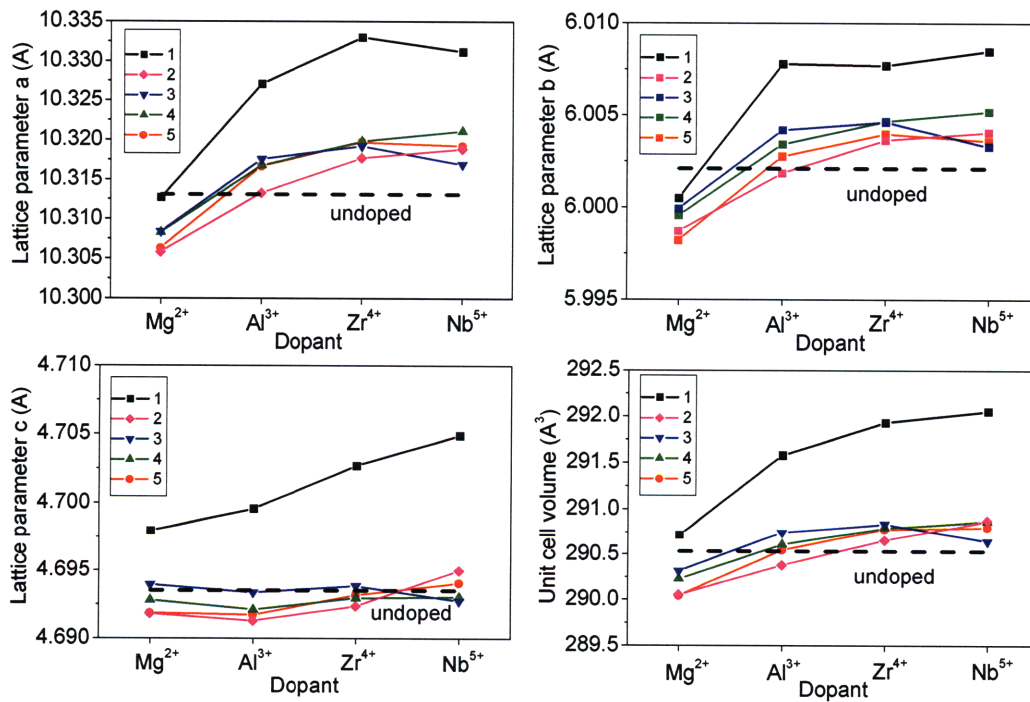


Figure 6-2: Lattice parameters and unit cell volumes for four dopants each at 5 at% overall doping level, formulated according to Mechanisms 1-5, compared to the undoped control sample (dashed horizontal line). Values are from Rietveld refinements of X-ray diffraction spectra. The unit cell parameters increase as the valence of the dopant increases; Mechanism 1 in which the solute substitutes onto the M1 site with charge compensation by Li vacancies gives the largest unit cell expansion



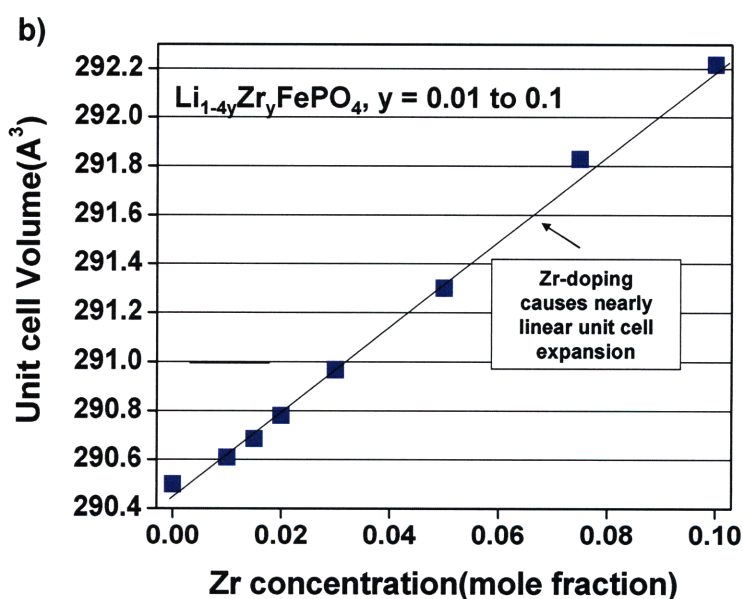
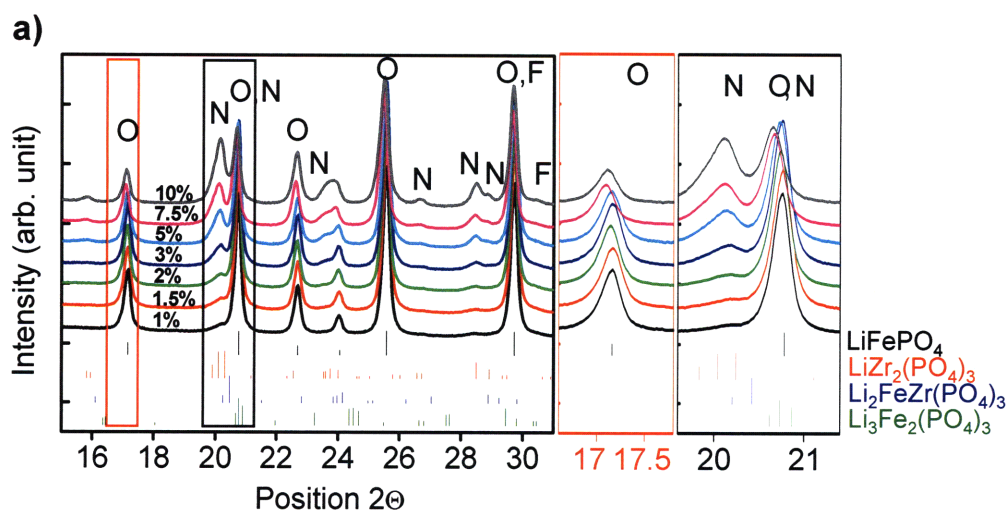
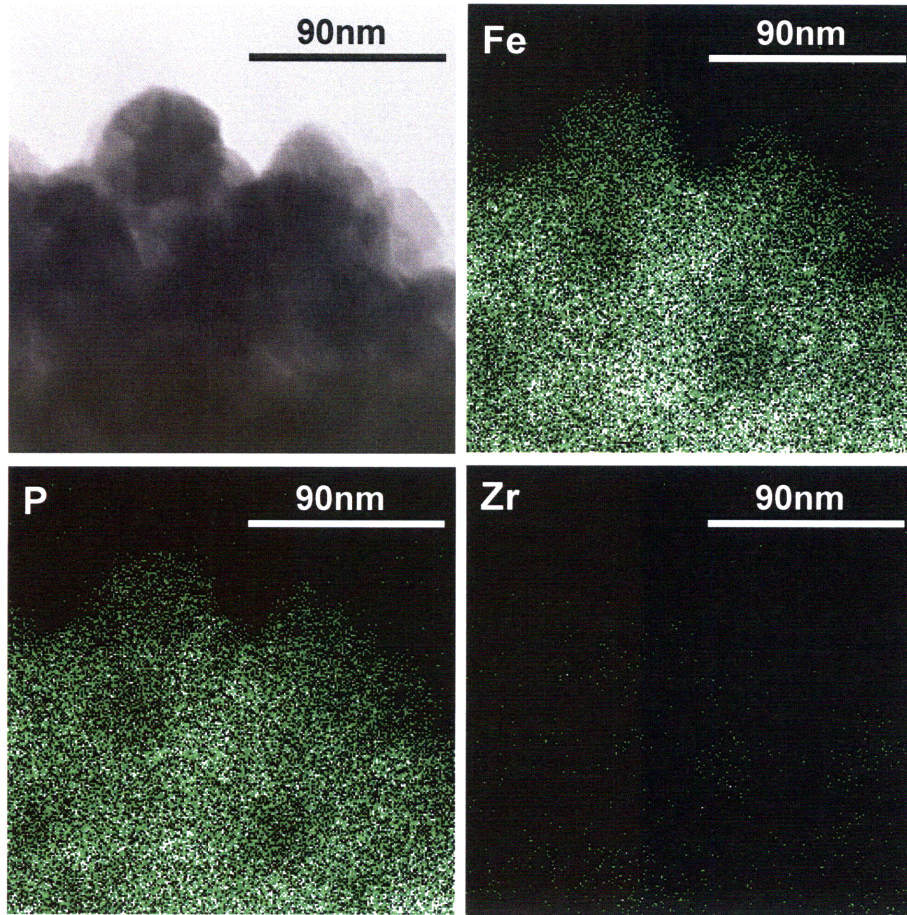


Figure 6-3: a) X-ray diffraction spectra for samples with varying Zr doping level showing olivine (O), NASICON (N), and trace  $\text{Fe}_2\text{P}_2\text{O}_7$  (F). High-quality spectra ( $R_{\text{exp}} \sim 1.5\%$ ) were collected using a Rigaku RTP500RC instrument at scan rates of  $0.18^\circ \text{ min}^{-1}$  over the  $2\theta$  range from  $15^\circ$  to  $135^\circ$ . Limited  $2\theta$  ranges are shown on an expanded scale for clarity. Lines for NASICON phases of several compositions are shown for comparison. With increasing Zr content, the single NASICON phase in the sample increases in amount and exhibits a peak shift to lower angles indicating increasing Zr content in this phase. b) Unit cell volume expansion for Zr-doped samples shows nearly linear increase with increasing Zr doping level up to 10% without saturation.



**Figure 6-4:** STEM composition maps of the 5 mol % Zr sample, doping according to mechanism 1, showing that Zr is uniformly detected in the crystallites.

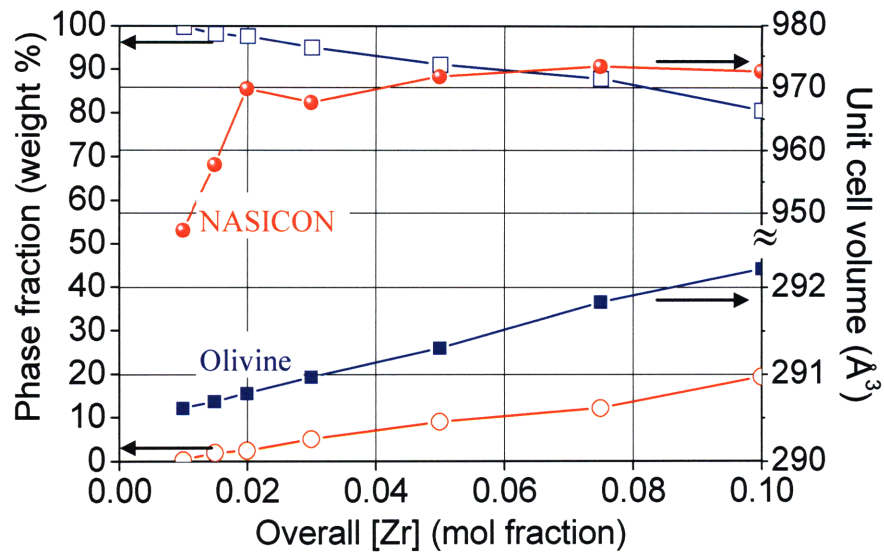


Figure 6-5: Rietveld-refined phase fractions (□: Olivine, ○: NASICON) and unit cell volumes (■: Olivine, ●: NASICON) for olivine and NASICON in Zr-doped compositions prepared according to defect mechanism 1. As is permitted by the Gibbs phase rule, the relative amounts and unit cell volumes (reflecting Zr concentration) vary continuously as the overall Zr doping level is increased. Thus the solubility of Zr in both phases increases with Zr content.

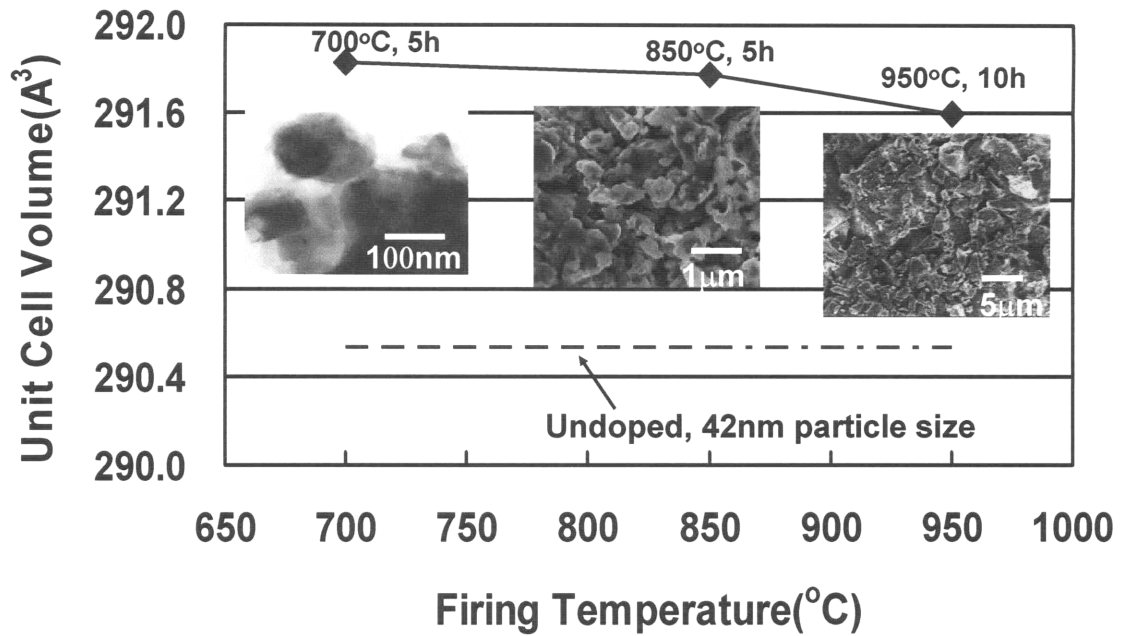


Figure 6-6: Olivine unit cell volume vs. firing temperature for a 7.5% Zr-doped composition, compared to results for undoped  $\text{LiFePO}_4$ . The unit cell volume decreases slightly upon coarsening of the particle size to  $>1 \mu\text{m}$  from an initial average particle size of 45 nm (determined from BET measurement), but remains significantly greater than that for the undoped sample, showing that the solid solubility of Zr is slightly size-dependent.

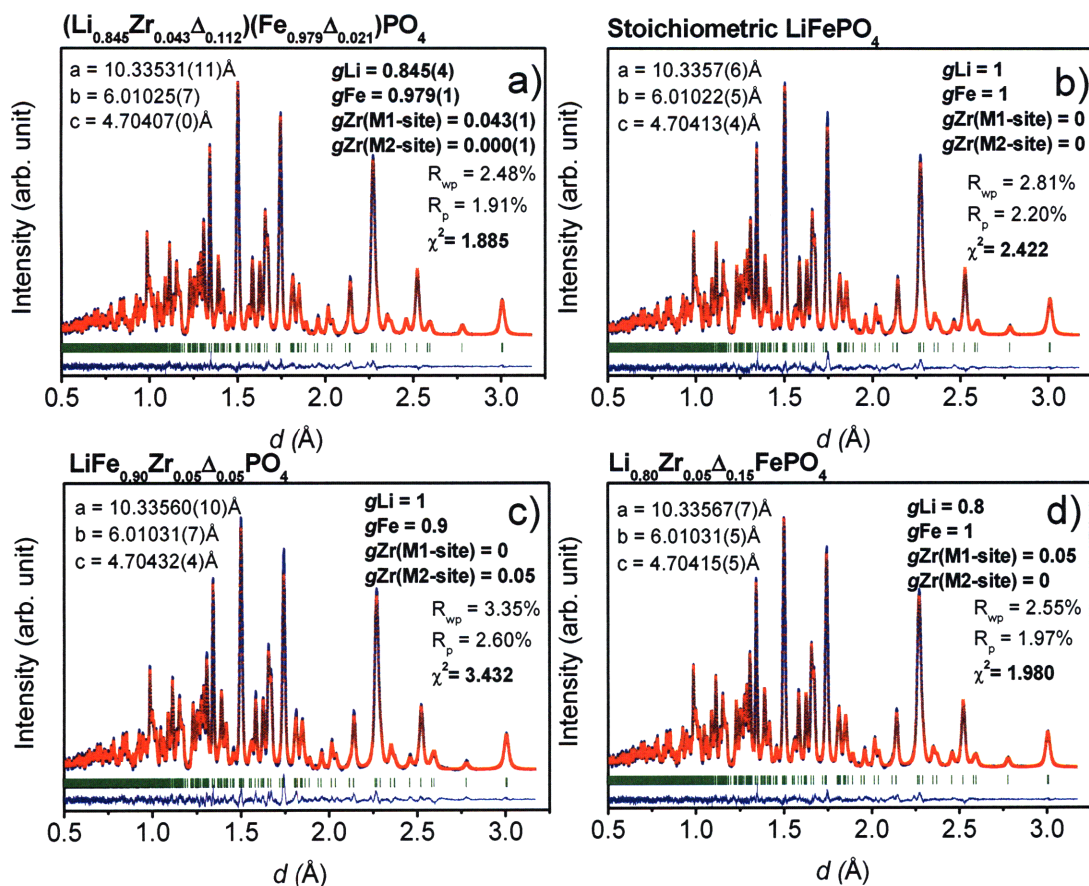


Figure 6-7: An example of neutron diffraction spectrum from a 5 mol% Zr sample doped according to Mechanism 1. Two additional neutron and one XRD spectra were simultaneously refined according to the following models: a)  $(\text{Li}_{0.845}\text{Zr}_{0.043}\Delta_{0.112})(\text{Fe}_{0.979}\Delta_{0.021})\text{PO}_4$ ; b) stoichiometric  $\text{LiFePO}_4$ ; c)  $\text{Li}(\text{Fe}_{0.90}\text{Zr}_{0.05}\Delta_{0.05})\text{PO}_4$ ; and d)  $(\text{Li}_{0.8}\text{Zr}_{0.05}\Delta_{0.15})\text{FePO}_4$ .  $\Delta$  represents vacant lattice sites. The observed intensity data are shown by the solid line, and the overlying dotted line is the calculated intensity. Vertical markers below the diffraction patterns indicate positions of possible Bragg reflections. Differences between the observed and calculated intensities are plotted in the same scale. The best goodness-of-fit (smallest  $R_{\text{wp}}$ ,  $R_{\text{p}}$ , and  $\chi^2$  parameters) is obtained for models a) and d) in which the Zr is assumed to occupy the M1 sites, and especially for model a) in which the Zr site concentration is allowed to vary.

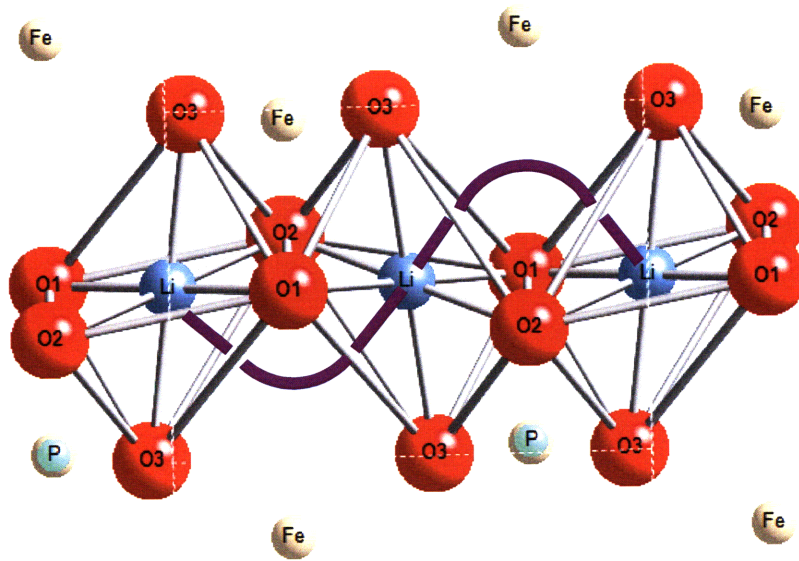


Figure 6-8: Curved Li migration path in the olivine [010] direction <sup>3, 21, 22</sup>, for comparison with the Li-O and O-O bond length changes in Table 6-II. Note that the diffusion path lies out of the x-y plane and passes through O1-O2-O3 triangle.

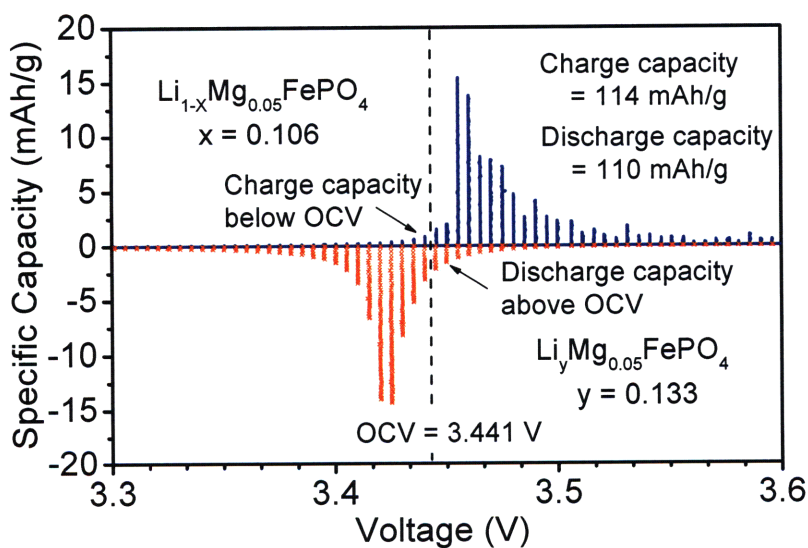
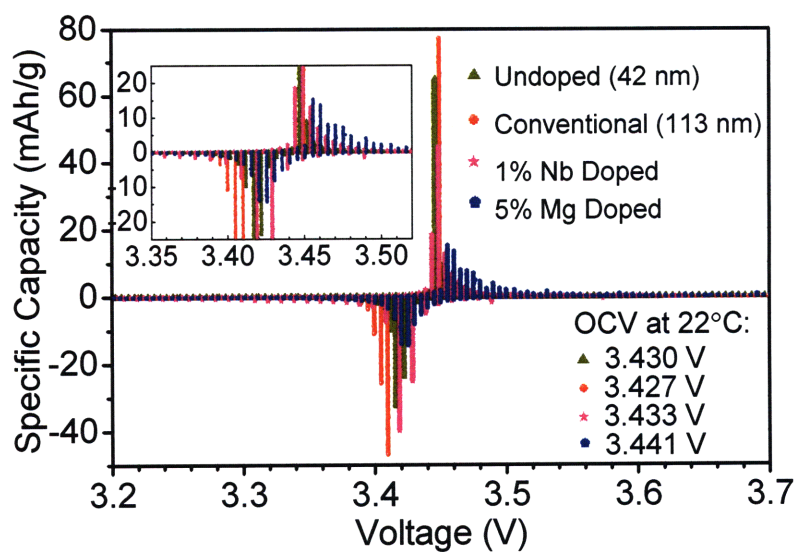


Figure 6-9: Capacity versus voltage measured potentiostatically upon charge and discharge in 5 mV steps for the 5 mol% Mg doped nanoscale sample (bottom). Solid solubility regions  $x, y$  can be measured and calculated from the accumulated capacities below and above the OCV for  $x$  in the Li-rich  $\text{Li}_{1-x}\text{FePO}_4$  phase and  $y$  in the Li-poor  $\text{Li}_y\text{FePO}_4$  phase, respectively. The solid solubility  $x$  and  $y$  are calculated to be 10.6% and 13.3%, respectively. PITT responses of the undoped control sample, the conventional coarse-grained sample, and 1% Nb doped nanoscale sample were plotted for comparison (top).

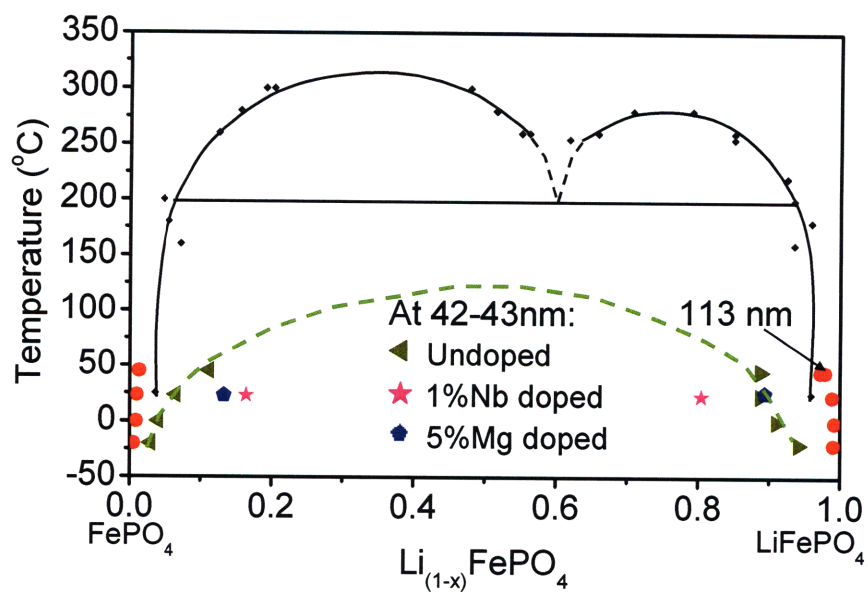
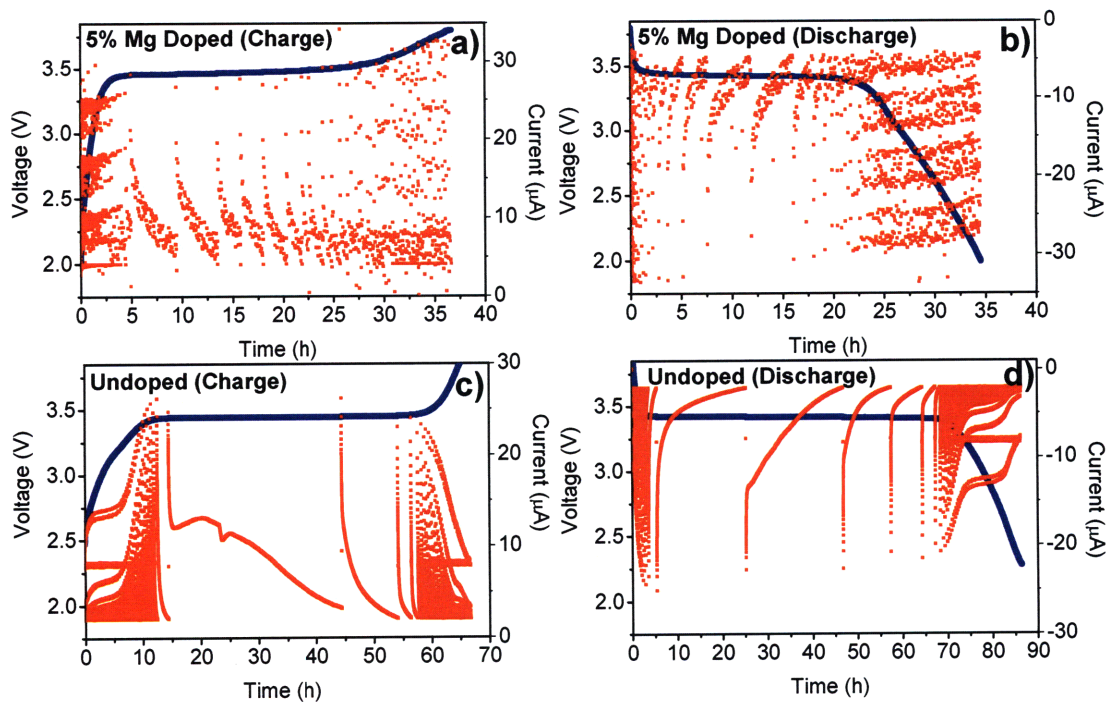


Figure 6-10: Comparative phase diagram shows the miscibility gap contraction of nanoscale Mg and Nb doped samples as compared to the undoped control of similar particle size (42 nm) and a coarser conventional powder (113nm), each measured using the same PITT protocol. The equilibrium phase diagram for bulk  $\text{Li}_{1-x}\text{FePO}_4$  (micron size) published by Dodd et al. <sup>16</sup> is also shown for comparison.





**Figure 6-11: Potentiostatic intermittent titration tests (PITT), showing 5 mV voltage steps (blue) and corresponding current relaxation (red). a) 5% Mg doped sample during charge; b) 5% Mg doped sample during discharge; c) Undoped sample during charge; d) Undoped sample during discharge. The 5% Mg-doped nanoscale sample exhibits a characteristic of fast phase transformation with a peak current at the start of each voltage step followed by monotonically decay, at all overpotentials. The undoped sample exhibits slower rate of current decay and, at some potentials, rise in current as a phase transformation barrier is overcome. The cut-off currents were  $C/100$  for the 5% Mg doped sample and  $C/200$  for the undoped sample, respectively.**

**Table 6-I. Ideal crystal compositions and defect compensations mechanisms tested, with  $M^{n+}$  substituting on M1 and/or M2 sites.  $M^{n+}$  represents  $Mg^{2+}$ ,  $Al^{3+}$ ,  $Zr^{4+}$  or  $Nb^{5+}$  ions.**

#	Ideal crystal composition	Defect compensation mechanism	Defect Compensation (Kroger-Vink notation)
1	$Li_{1-ny}M^{n+}_yFePO_4$	Li-substitution & Li-vacancy compensation	$[V_{Li}'] = (n-1)[M_{Li}^{(n-1)*}]$ $[V_{Li}'] = 3[Zr_{Li}''']$
2	$Li_{1-(n-2)y}M^{n+}_yFe_{1-y}PO_4$	Fe-substitution & Li-vacancy compensation	$[V_{Li}'] = (n-2)[M_{Fe}^{(n-2)*}]$ $[V_{Li}'] = 2[Zr_{Fe}''']$
3	$Li_{1-y}M^{n+}_yFe_{1-(n-1)y/2}PO_4$	Li-substitution & Fe-vacancy compensation	$2[V_{Fe}'] = (n-1)[M_{Li}^{(n-1)*}]$ $2[V_{Fe}'] = 3[Zr_{Li}''']$
4	$LiM^{n+}_yFe_{1-ny/2}PO_4$	Fe-substitution & Fe-vacancy compensation	$2[V_{Fe}'] = (n-2)[M_{Fe}^{(n-2)*}]$ $[V_{Fe}'] = [Zr_{Fe}''']$
5	$LiFePO_4 + M_xO_y$	Stoichiometric & impurity	Defect compensation undetermined

**Table 6-II: Rietveld refined site occupancies (g), atomic coordinates (x, y, z) and thermal parameters for a 5% Zr doped sample doped according to defect mechanism 1. The site occupancies correspond to an approximately charge-neutral composition of  $(\text{Li}_{0.845}\text{Zr}_{0.043}\text{Al}_{0.112})(\text{Fe}_{0.979}\text{Al}_{0.021})\text{PO}_4$ . Lattice parameters also shown.**

	g	x	y	z	100*Uiso
Li	0.845(4)	0	0	0	1.61(5)
Fe	0.979(1)	0.2822(4)	0.25	0.9750(10)	0.69(1)
P	1	0.0957(7)	0.25	0.4198(1)	0.78(2)
O1	1	0.0982(7)	0.25	0.7425(2)	1.06(2)
O2	1	0.4577(7)	0.25	0.2045(2)	0.81(2)
O3	1	0.1659(6)	0.0478(1)	0.2851(1)	1.01(1)
ZrLi	0.043(1)	0	0	0	0.69(1)
ZrFe	0.000(1)	0.2822(4)	0.25	0.9750(10)	0.69(1)
$R_{\text{wp}} = 2.48\%$		$R_p = 1.91\%$		$\chi^2 = 1.885$	

$$a = 10.33531(11) \text{ \AA} \quad b = 6.01025(7) \text{ \AA} \quad c = 4.704072(0) \text{ \AA}$$

$$\alpha = 90^\circ \quad \beta = 90^\circ \quad \gamma = 90^\circ$$

**Table 6-III: Goodness-of-fit parameters and bond lengths of doped compositions based on defect Mechanism 1, M1 site doping with M1-site vacancy compensation mechanism, compared to undoped control sample. The Mg<sup>2+</sup> results are for a 10% doping level while the Al<sup>3+</sup>, Zr<sup>4+</sup> and Nb<sup>5+</sup> results are for 5% doping level. Systematic expansion of the oxygen-oxygen and lithium-oxygen bond lengths is observed upon doping at these levels.**

Ion-pair	Bond Lengths				
	Undoped	Mg <sup>2+</sup>	Al <sup>3+</sup>	Zr <sup>4+</sup>	Nb <sup>5+</sup>
$\chi^2$	1.504	1.178	1.493	1.885	1.846
R <sub>wp</sub> (powder total)	0.024	0.033	0.022	0.025	0.021
R <sub>p</sub> (powder total)	0.018	0.025	0.017	0.019	0.016
Fe-O(1)	2.193	2.183	2.196	2.194	2.199
Fe-O(2)	2.106	2.099	2.106	2.110	2.105
Fe-O(3) (x 2)	2.067	2.064	2.067	2.071	2.070
Fe-O(3) (x 2)	2.237	2.235	2.242	2.245	2.245
Li-O(1) (x 2)	2.171	2.179	2.176	2.182	2.179
Li-O(2) (x 2)	2.088	2.096	2.091	2.093	2.097
Li-O(3) (x 2)	2.190	2.200	2.193	2.197	2.197
P-O(1)	1.525	1.521	1.520	1.518	1.522
P-O(2)	1.539	1.539	1.541	1.543	1.544
P-O(3) (x 2)	1.553	1.555	1.549	1.551	1.548
O(1)-O(2)	2.965	2.988	2.975	2.981	2.985
O(1)-O(3)	2.903	2.913	2.911	2.914	2.916
O(2)-O(3)	2.476	2.482	2.474	2.475	2.479

# Chapter 7

## Conclusions

### Summary

Olivine compounds  $\text{LiMPO}_4$  have the advantages of low cost, reasonable high energy density, high thermal stability, and non-toxicity. However, its practical utility as a cathode material for lithium ion batteries was initially limited. It was believed to only be capable of cycling at low rates due to its sluggish mass and charge transport.<sup>1</sup> In the past few years the electrochemical performance of these phospho-olivine cathodes has been substantially improved via surface coating with an electron-conducting phase (mostly carbon),<sup>2-3</sup> particle size minimization,<sup>4-6</sup> and/or doping.<sup>6</sup> Nanoscale olivines have already been commercialized as a cathode material in batteries for power tools and other high power applications, and are a serious candidate for future batteries in hybrid, plug-in hybrid electric or all-electric vehicles. It can also be commercialized for other applications requiring a low-cost and safe battery. Nevertheless, there is more room for improvement and still a great deal to be learned about  $\text{LiMPO}_4$ .

The use of nanoscale samples has proven to be an effective way to improve the electrochemical properties of these battery materials due partially to the reduction of solid state transport length and increase in surface reactivity. However, unexpected behavior arising at nanoscale dimensions is an interesting topic which was not yet explored. At the beginning of this study, the impact of phase behavior and phase transformation kinetics on electrochemical properties was not well understood and literature results were limited to primarily coarse grained samples ( $> 100$  nm). For example, the phase composition of nanoscale samples during electrochemical cycling was not well characterized. The mechanism of the transformation between the two phases (triphylite and heterosite), which becomes more complicated as particle sizes approach nanometer dimensions, was

not known. Understanding such correlations was the primary goal of this thesis. Even though only the olivine compounds were studied in this thesis, the understanding achieved here can be applicable to other lithium intercalation compounds.

The major results of this thesis and the application of these results are as follows:

We found that the phase stability of this system could be easily manipulated by changing particle size and by doping (Chapter 3 and Chapter 4). We found dramatic changes in the miscibility gap compared to the previous published phase diagrams. The miscibility gap in undoped nanoscale  $\text{Li}_{1-x}\text{FePO}_4$  powders contracts with decreasing particle size and increasing temperature. In aliovalent substituted olivine the miscibility gap is reduced further, exhibiting about 2 times larger lithium nonstoichiometry at room temperature than the undoped powder of equivalent size (Chapter 4). These changes in phase stability of the materials have been shown to have significant effects on structure and properties of this system.

The greater extent of solid solution in both the Li-poor and Li-rich coexisting phases is also correlated with a reduced lattice mismatch between the two co-existing phases during electrochemical cycling (Chapter 4). We showed that the olivine cathodes with reduced lattice mismatch during electrochemical cycling have substantially better rate capability than the materials with larger misfit (Chapter 4). The correlation between elastic misfit and rate capability can explain the rate capability behavior in several other lithium intercalation oxides exhibiting first-order phase transitions as well. For example,  $\text{LiMnPO}_4$  has a much larger misfit between the co-existing phases than  $\text{LiFePO}_4$ , and exhibits a very poor rate capability even in its nanoscale forms.  $\text{Li}_4\text{Ti}_5\text{O}_{12}$ , on the other hand, is a cubic spinel known for having nearly zero dimensional change between its lithiated and delithiated phases, and is also known for having exceptional rate capability when produced in nanoscale form. A third example is the spinel  $\text{LiMn}_2\text{O}_4$ . Between the composition limits  $\text{MnO}_2$  and  $\text{Li}_{0.5}\text{MnO}_2$ , there exists a continuous solid-solution cubic spinel that is known for its high rate capability. However, upon further lithiation, a first-order phase transition from  $\text{Li}_{0.5}\text{MnO}_2$  to tetragonal “ $\text{Li}_2\text{Mn}_2\text{O}_4$ ” occurs with a 5.6%

volume misfit and 16% change in the  $c/a$  ratio. The rate capability in this regime is found to be markedly inferior to that of the cubic spinel. We know of no counterexamples in which high rate capability is obtained for a phase transformation of large misfit. Thus, a strain-based predictive criterion for the design and selection of high power battery electrode compounds is suggested.

In addition to the changes in phase stability arising from particle size reduction or doping, we found that the phase transformation kinetics as determined from time resolved electrochemical and structural measurements were qualitatively different among nanoscale, conventional, and doped nanoscale samples as well (Chapter 4, Chapter 5, and Chapter 6). Detailed analysis of the differences is ongoing and will be published elsewhere.

Moreover, we show that the product of the transformation becomes more complicated as particle size approaches nanometer dimensions (Chapter 5). We conducted a comparative study of the structural and phase changes taking place during electrochemical cycling of nanoscale ( $< 100$  nm) and conventional  $\text{Li}_{1-x}\text{MPO}_4$  and found that phase transformation path differs significantly between the two types of materials. Whereas coarse-grained  $\text{LiFePO}_4$  undergoes a conventional two-phase reaction in which crystalline  $\text{LiFePO}_4$  and  $\text{FePO}_4$  co-exist, in nanoscale sample there is a reduced miscibility gap between co-existing crystalline phases; and upon charge, a fraction (increasing with increasing size) of the crystalline delithiated  $\text{Li}_y\text{FePO}_4$  that is formed is partially amorphous and metastable.

Questions regarding whether  $\text{LiMPO}_4$  olivines can be doped with aliovalent ions have stimulated considerable interest and controversy in the Li-ion battery field. For the purpose of understanding plausible defect compensation mechanisms and determining the aliovalent ion solubility in the olivine compounds, we conducted a systematic study using model compositions designed to accommodate  $\text{Mg}^{2+}$ ,  $\text{Al}^{3+}$ ,  $\text{Zr}^{4+}$ ,  $\text{Nb}^{5+}$  ions in solution on the M1 and/or M2 sites of  $\text{LiFePO}_4$  with appropriate charge-compensating defects (Chapter 6). We showed that aliovalent solute doping of  $\text{LiFePO}_4$  was not only possible,

but had several distinct consequences which could be manipulated to improve battery electrode properties. We find that the olivine lattice can accept aliovalent cations of 2+ through 5+ at concentrations of at least several percent, with charge-compensation by M1 vacancies being at least one available defect mechanism. The disorder produced by these substitutions cause the lithium miscibility gap to be contracted, and by modifying the crystal structure so as to expand the lithium migration channels, may have the effect of increasing lithium mobility. Along with nanoscaling and other compositional modifications of the olivines, controlled aliovalent doping is a methodology that may be used to advantage in the ongoing worldwide effort to develop improved battery technologies for energy applications.

## **Future Work**

### **Lithium Transport Kinetics in Olivine Cathodes**

A future study of potential importance is to determine the lithium transport mechanism limiting electrochemical cycling of these materials. Electrochemical transport in all Li insertion electrodes can be complicated because, in many cases, they involve interfacial transfer, solid-state diffusion, and phase transitions. Olivine  $\text{LiFePO}_4$  electrodes are a classic example of battery materials in which any one of the three processes can be rate-limiting. The kinetic characteristics, however, can be analyzed and distinguished by electrochemical methods such as potentiostatic intermittent titration tests (PITT) and impedance spectroscopy (IS). It is believed also that the exact lithium intercalation/deintercalation mechanism in different samples depends on the size, morphology and surface chemistry of the samples. Fundamental understanding of the various contributions to the kinetics of olivine electrodes is important to the future development of phosphate battery technology.



## **Electrochemically Driven Phase Transformations Studies using In-situ X-ray Diffraction**

Our findings (Chapter 5) that the phase transformations during electrochemical cycling of nanoscale olivine cathodes involved transitions to amorphous or metastable phase(s) has led Ming et al.<sup>7</sup> to develop a model to assess the conditions under which non-equilibrium phase transitions may occur in  $\text{LiMPO}_4$  particles. Their model is based on the diffuse-interface model and developed for the effects of overpotential, size, and misfit strain. The overpotential is defined as the difference between the electrical potential imposed on a particle and the equilibrium potential corresponding to the composition and phase state of the particle. There were three major predictions resulting from this model. First, it was predicted that, due to the lower surface energy of the amorphous phase, an initially crystalline phase may undergo amorphization during cycling when the particle size is below a critical value. Second, the effect of applied electrical overpotentials on the phase stability was predicted to strongly influence the phase transition pathways of small particles. Third, the tendency to amorphize was predicted to be significantly affected by the magnitude of the misfit strain between the lithiated and delithiated crystalline phases. It was shown that there should be a critical misfit strain above which the preferred transformation pathway is amorphization, regardless of the particle size. This model provides a useful road map to future experiments.

We are currently conducting critical experiments using in-situ synchrotron X-ray diffraction at Brookhaven National Laboratory beamline X14A of the National Synchrotron Light Source to track the overpotential and time dependence of phase evolution in samples of various compositions and crystallite size scales. Ex-situ XRD (as shown in Chapter 5) can provide information on the equilibrium or near equilibrium states of the material. However the phase transformation and the misfit strain relaxation may occur too fast to be observed by ex-situ XRD. We have therefore used in-situ synchrotron XRD for a more thorough understanding of the phase behavior of  $\text{LiFePO}_4$  during charge and discharge in actual electrochemical cells. Since in-situ XRD can simultaneously monitor the structural changes during electrochemically cycling, it can

give us information related to the effects of overpotential, size, misfit strain, and even crystalline anisotropy, given the right kind of sample.

### **Mixed Transition Metal Olivines Cathodes for Li-ion Batteries**

A cathode material with high theoretical voltage is usually desirable in high energy density rechargeable batteries, because the energy output is mainly determined by the product of the voltage and the specific capacity of the cell. In the olivine-type  $\text{LiMPO}_4$  family, the  $\text{P}_{\text{tet}}\text{-O-M}_{\text{oct}}$  linkage in the structure induces the superexchange interaction that tunes the  $\text{M}^{3+}/\text{M}^{2+}$  redox energy to useful levels  $\sim 3.4$ ,  $4.1$ , and  $4.8$  V for  $\text{Fe}^{3+}/\text{Fe}^{2+}$ ,  $\text{Mn}^{3+}/\text{Mn}^{2+}$ , and  $\text{Co}^{3+}/\text{Co}^{2+}$ , respectively.<sup>1,8</sup> Olivine-type solid solutions such as  $\text{Li}(\text{Mn}_y\text{Fe}_{1-y})\text{PO}_4$  or  $\text{Li}(\text{Co}_z\text{Fe}_{1-z})\text{PO}_4$  can be promising alternatives and should be investigated further, since they have the potential to generate higher energy density than pure  $\text{LiFePO}_4$  electrodes.  $\text{Li}(\text{Mn}_y\text{Fe}_{1-y})\text{PO}_4$  looks especially promising because it operate at  $3.4\text{-}4.1$  V vs.  $\text{Li}/\text{Li}^+$ . This is providential, because it is not so high as to decompose the organic electrolyte but is not so low as to sacrifice energy density. In addition it would be interesting to see the particle size dependence effect on phase stability in these olivine-type solid solution compounds as well.

### **References**

1. A. K. Padhi, K. S. Nanjundaswamy, and J. B. Goodenough, *J. Electrochem. Soc.*, **144**, 1188 (1997).
2. N. Ravet, J. B. Goodenough, S. Besner, M. Simoneau, P. Hovington, and M. Armanin The Electrochemical Society and the Electrochemical Society of Japan Meeting Abstracts, vol. 99-2, (Abstract no 127). Honolulu, HI, 1999.
3. I. Belharouak, C. Johnson, and K. Amine, *Electrochem. Comm.*, **7**, 983 (2005).
4. D. H. Kim and J. Kim, *Electrochem. Solid-State Lett.*, **9** A439 (2006).
5. A. Yamada, S. C. Chung, and K. Hinokuma, *J. Electrochem. Soc.*, **148**, A224 (2001).
6. S. Y. Chung, J. T. Bloking, and Y. M. Chiang, *Nat. Mater.*, **2**, 702 (2003).

7. M. Tang, H. -Y. Huang, N. Meethong, Y. -H. Kao, W. C. Carter, Y. -M. Chiang, *Chem. Mater.*, in press.
8. K. Amine, H. Yasuda, and M. Yamachi, *Electrochem. Solid-State Lett.*, **3**, 178 (2000).